Synthesis and Functionalization of Zinc Oxide Nanowires

by

Jia Xu

A Dissertation Presented in Partial Fulfillment
of the Requirements for the Degree
Doctor of Philosophy

Approved April 2017 by the
Graduate Supervisory Committee:

Jingyue Liu, Chair
David Smith
Candace Chan
Bin Mu

ARIZONA STATE UNIVERSITY

May 2017

ABSTRACT

Zinc oxide nanowires (NWs) have broad applications in various fields such as nanoelectronics, optoelectronics, piezoelectric nanogenerators, chemical/biological sensors, and heterogeneous catalysis. To meet the requirements for broader applications, growth of high-quality ZnO NWs and functionalization of ZnO NWs are critical. In this work, specific types of functionalized ZnO NWs have been synthesized and correlations between specific structures and properties have been investigated.

Deposition of δ-Bi_2O_3 (narrow band gap) epilayers onto ZnO (wide band gap) NWs improves the absorption efficiency of the visible light spectrum by 70%. Furthermore, the deposited δ-Bi_2O_3 grows selectively and epitaxially on the {11-20} but not on the {10-10} facets of the ZnO NWs. The selective epitaxial deposition and the interfacial structure were thoroughly investigated. The morphology and structure of the Bi_2O_3/ZnO nanocomposites can be tuned by controlling the deposition conditions.

Various deposition methods, both physical and chemical, were used to functionalize the ZnO NWs with metal or alloy nanoparticles (NPs) for catalytic transformations of important molecules which are relevant to energy and environment. Cu and PdZn NPs were epitaxially grown on ZnO NWs to make them resistant to sintering at elevated temperatures and thus improved the stability of such catalytic systems for methanol steam reforming (MSR) to produce hydrogen. A series of Pd/ZnO catalysts with different Pd loadings were synthesized and tested for MSR reaction. The CO selectivity was found to be strongly dependent on the size of the Pd: Both PdZn alloy and single Pd atoms yield low CO selectivity while Pd clusters give the highest CO selectivity.

By dispersing single Pd atoms onto ZnO NWs, Pd_1/ZnO single-atom catalysts (SACs) was synthesized and their catalytic performance was evaluated for selected

catalytic reactions. The experimental results show that the Pd_1/ZnO SAC is active for CO oxidation and MSR but is not desirable other reactions. We further synthesized ZnO NWs supported noble metal (M_1/ZnO; M=Rh, Pd, Pt, Ir) SACs and studied their catalytic performances for CO oxidation. The catalytic test data shows that all the fabricated noble metal SACs are active for CO oxidation but their activity are significantly different. Structure-performance relationships were investigated.

To my family for their unconditional support.

ACKNOWLEDGMENTS

I would like to thank my advisor, Professor Jingyue Liu, for offering me the opportunity to work in his group and providing his instruction and support. This work was done under his kind mentoring and concentrated guidance. I would also like to thank my committee members, Professor David Smith, Professor Candace Chan and Professor Bin Mu for their time and helpful advice.

We gratefully acknowledge the use of the John M. Cowley Center for High Resolution Electron Microscopy, the facilities within the LeRoy Eyring Center for Solid State Science and the Goldwater Environmental Laboratory at Arizona State University.

I also want to thank all the members in our group for their friendship and the moments we spent together, especially Botao Qiao, Jiaxin Liu, Yian Song, Yang Lou, Yiwei Yu, Wen Zhang, Honglu Wu and Yafeng Cai who gave me a hand with my research. I would like to thank Mr. David Wright and Mr. David Lowry for their supports in sample preparation.

I sincerely thank my parents for their eternally immutable love and support.

TABLE OF CONTENTS

Page

CHAPTER Page

CHAPTER Page

CHAPTER Page

LIST OF TABLES

Table Page

LIST OF FIGURES

Figure Page

Figure Page

Figure Page

Figure Page

Figure Page

Figure Page

Figure Page

LIST OF ACRONYMS

ACRONYM	DEFINITION
NW	Nanowire
NP	Nanoparticle
VLS	Vapor liquid solid
VS	Vapor solid
VPT	Vapor phase transport
MSI	Metal-support interaction
PEMFCs	Polymer electrolyte membrane fuel cells
PVD	Physical vapor deposition
MOCVD	Metal-organic chemical vapor deposition
MBE	Molecular beam epitaxy
PLD	Pulsed laser deposition
DSC	Dye sensitized solar cell
SERS	Surface Enhanced Raman Scattering
STEM	Scanning transmission electron microscopy
EELS	Electron energy loss specroscopy
MSR	Methanol steam reforming
WGS	Water gas shift
PROX	Preferential oxidation of CO

Chapter 1 Introduction

1.1 One-dimensional (1D) nanostructures

Novel nanostructured materials have attracted tremendous interest due to their remarkable performance in broad applications. The nature of a number of physicochemical effects changes drastically as the size of the system decreases down to the nanometer scale. Nanomaterials or nanostructured materials are generally classified into four categories depending on their shape: 1) zero-dimension (0D), 2) one-dimension (1D), 3) two-dimension (2D) and 4) three-dimension (3D)[2]. Typically 1D structures have cross-sections in the range of 1-100 nm and lengths of many micrometers or longer with the high aspect ratio and large specific area. They are of interest both for fundamental research and practical applications because of their unique properties and as building blocks for other more complex architectures [3]. The major advantages with the 1D nanostructures are their important role in fabricating electronic, optoelectronic, electrochemical, and electromechanical devices with nanoscale dimensions[4]. Their unique structure makes them flexible and can allow them to be physically manipulated into various shapes according to design requirements. Their single-crystalline nature ensures extremely low defect density and the absence of other structural irregularities, attributing to their superiority in mechanical strength. As 1D nanostructures combine spatial confinement effect in two dimensions and has the ability of feasible manipulation in one dimension, they provide a good model system to investigate the dependence of electrical and thermal transport or mechanical properties on dimensionality and size reduction.

A wide class of nanomaterials, including metal oxides, elemental metals, insulators, semiconductors and carbon-based materials can be produced as 1D nanostructures [5]. In addition, these 1D nanostructures are in different configurations including wires, rods, fibers, tubes and belts. All of these 1D nanostructures have their own nature in structure and properties for different applications.

Among 1D nanostructures, metal oxide nanowires (NWs) have gained significant attention from scientific researchers owing to their ability to function as excellent catalysts and/or sensors. Because of large surface to volume ratio, the use of NWs rendering the ability for more surface atoms to participate in surface reactions and the increased electron and hole diffusion rate to the surface could facilitate quick desorption of molecules. Another current research activities for applications of NWs, due to their small length scale in 2D, excellent flexibility, enhanced light absorption and higher thermoelectric coefficient, pertain to the energy harvesting devices to convert mechanical, thermal and especially solar energy into electricity. The major advantages of NWs in such applications are the qualities of their single-crystalline structure and operability for fabricating into various orientations (perpendicularly oriented NWs, parallel or in-plane NWs and meshed NWs) and complex geometries such as hierarchical structures. Such complex system increases the surface area and also reduces the charge recombination, attributed to higher efficiency in energy conversion.

Although 1D NWs are promising in many applications, as single component materials, it also has limitations. For multifunctional nanosystems, it is of vital importance to functionalize NWs and integrate it with different materials.

1.2 Heterostructured semiconductor NWs

"Hetero-structure" means combination of different structures as one entity. One of the important families of heterostructure (HS) is based on heterostructuring of 1D NWs. This could include several different situations depending on how the different components are combined.

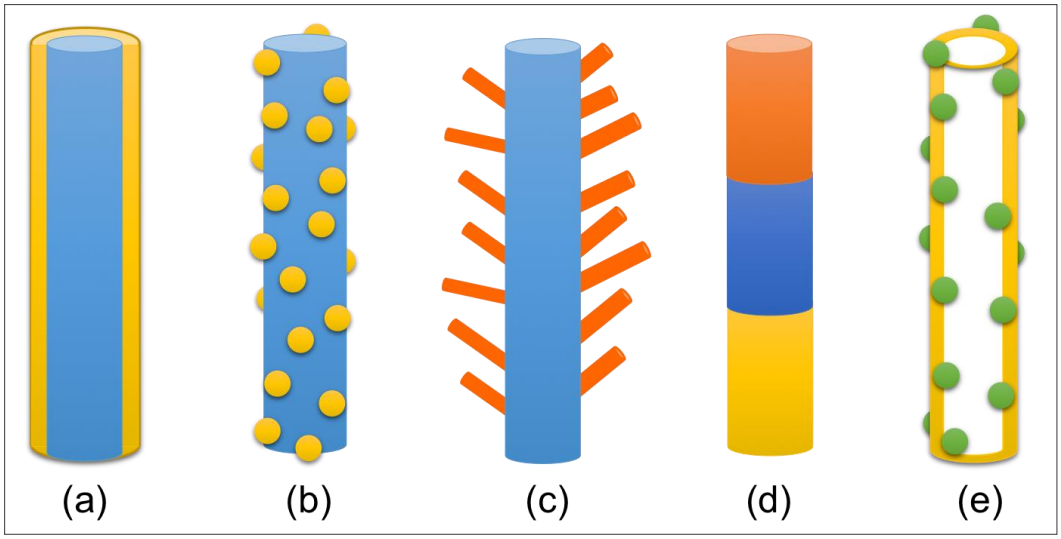

Figure 1.1 Schematic illustrations of different types of heterostructured NWs.

For example, core-shell NWs (Figure 1.1a) could adopt all possible advantages of core-shell nanoparticles and at the same time maintain the original properties of NWs, such as electron transport along the nanowire and confinement across the NWs[6]. Metal particle decorated semiconductor NWs (Figure 1.1b) could effectively enhance photocatalytic and photoelectrochemical cell performance[7]. Multi-segment heterostructured nanowires (Figure 1.1c), made by heterostructuring along nanowire axis, can be an efficient method for high-speed devices[8]. The addition of catalyst nanoparticles onto NWs can work as seed, leading to the growth of branches on nanowire trunks and form 3D hieratical nanostructures (Figure 1.1d) by using vapor-liquid-solid (VLS) mechanism or heterogeneous nucleation[9]. Another important type

of hetero-hollow-nanotube (Figure 1.1e) structures can be fabricated by sacrificing the cores[10]. Beside the decoration of nanoparticles on the outside of the NWs, decoration of nanoparticles on the inside walls of hollow tubes is also possible.

1.2.1 Effective charge separation

HSs could effectively assist the charge transfer and extend lifetime of carriers during photocatalytic reactions, which suffer from the rapid recombination of active charge carriers within crystals when electrons and holes migrate toward the surface. In order to decrease the recombination rate at the surface, electrons or holes traveling towards heterojunctions need to be quickly separated, reducing the probability of electron/hole annihilation[11].

Heterostructured NWs, composed of semiconductor with both narrow band gap and wide band gap components, can improve the efficiency of solar cells [12, 13].Under certain wavelength illumination, such as visible light, pairs of carriers are only formed inside the semiconductor with narrow band gap. On the other hand, different band gaps can make photogenerated carriers flow from one semiconductor to another, resulting in long time and effective separation[14]. It was previously reported that better charge separation and electron accumulation in the metal-semiconductor and semiconductor-semiconductor junctions shift the Fermi level to a more negative potential[15, 16]. For example, in the ZnO-CdS system, conduction band edge of ZnO is located between the conduction band and the valence band of CdS. In this band-gap configuration, when electron-hole pairs are generated by visible-light excitation in CdS shell, the photoelectrons can be transferred to the conduction band of the ZnO NWs, and holes could flow into the higher valance band of CdS, which facilitates the charge separation process of electron-hole pairs before they recombine (the scheme is shown in Figure

1.2a). This band-alignment is an important factor in the enhancement of the photoelectrochemical performances of the semiconductor-sensitized photoelectrodes. The improved separation efficiency of electron-hole pairs can be achieved by the established internal electric field at the interface between two semiconductors when they acquire an equalized Fermi level. In addition, the built-in electric field can further promote the separation of electron-hole pairs, thus leading to an enhanced activity.

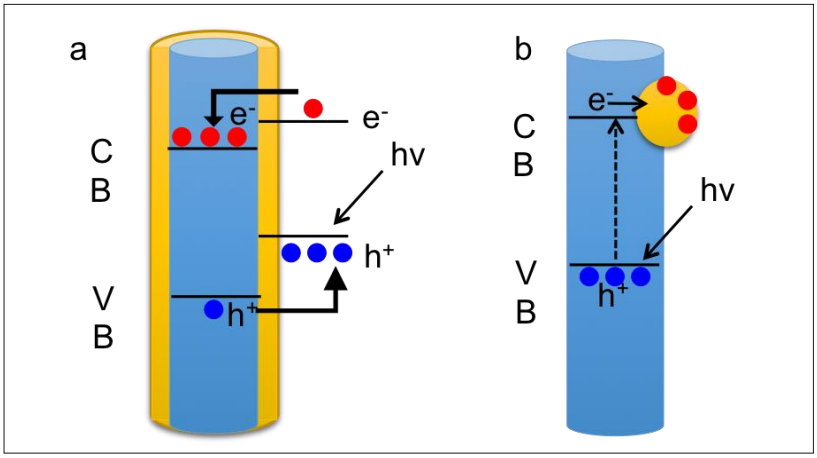

Figure 1.2. Schematic illustrations of charge separation of core-shell nanowire and metal decorated nanowire.

When semiconductor nanomaterials are heterostructured with metals, pairs of electrons and holes are generated and electron could quickly dissipate along the conductive path due to lower Fermi level of metals compared with the conduction band of a semiconductor, resulting in the efficient separation of charge carriers[17]. Metal nanoparticles also work as electron sink[18] (when the Fermi level of nanoparticles is lower than the conduction band of the semiconductor) and active sites for chemical reactions[19] (scheme shown in Figure 1.2b).

1.2.2 Improved surface stability

Due to the presence of surface trapping states, many semiconductors with lower optical band gaps may suffer from undesirable surface recombination losses and

photocorrosion, resulting in low efficiency and stability[20]. Heterostructuring of materials with a layer of stable material could effectively solve this issue without compromising their original properties. For example, it has been reported that the surface recombination sites of a-Fe_2O_3 can be efficiently passivated by coated surface CoO_x overlayers[21], thereby partially suppressing surface recombination. In addition, a thin layer of inert material could protect core from corrosion, high temperature oxidation and unwanted chemical reaction while maintain the original magnetic, catalytic, plasmonic and conductive properties.

Metal supported catalysts have demonstrated high catalytic performances in many important chemical reactions[22-29]. However, a major issue is that the precious NPs tend to agglomerate when being treated or used at elevated temperature[30]. For a supported catalyst, the metal-support interaction (MSI) strongly affects, not only the activity performance but also the NP's stability as a durable catalyst[31]. Heteroepitaxy, where coherent or semi-coherent interfaces form, has relatively low energy than other configurations[32] and can stabilize the metal NPs on support materials. Since most of the exposed surfaces of crystalline NWs support possess the same surface structure and are clean, then it is plausible to grow epitaxial NPs onto the surfaces of the support if certain conditions are met[33]. By anchoring metal NPs onto faceted NWs, both supported Au NPs[34] and Pd NPs[35] are resistant to sintering and show better stability compared with those are supported on commercially available powders.

1.3 Zinc Oxide (ZnO) and ZnO nanostructures

ZnO nanostructures have received broad attention due to their applications in electronics, optics and photonics. Dating back to the 1960's, ZnO thin films has been

synthesized for applications of sensors, transducers and catalysts. Nanostructured ZnO is a versatile functional material that has a diverse group of growth morphologies[36].

1.3.1 ZnO: Material properties and applications

ZnO is a II-VI semiconductor material with a direct and wide band gap in the near-UV spectral region[37] making it suitable for short wavelength optoelectronic applications. A material with a direct band gap is technologically beneficial, as radiative recombination in an indirect band gap material cannot occur without a change in momentum, which normally requires phonon absorption/emission, making it a much lower probability process. ZnO has an large exciton binding energy of 60meV is a desirable property because it favors the radiative recombination of excitons, which are not thermally dissociated at room temperature[38, 39], thus allowing for a more efficient light emission at room temperature. In piezoelectric materials, an applied voltage generates a deformation in the crystal and vice versa. These materials are generally used as sensors, transducers and actuators. The low symmetry of the wurtzite crystal structure combined with a large electromechanical coupling in ZnO gives rise to strong piezoelectric and pyroelectric properties[37].ZnO possesses high chemical and thermal resistance, which is widely used in the creation of instruments, such as the formation of transparent contact of solar cells. ZnO also has a strong luminescence in the green-white region of the spectrum, known as an efficient phosphor[40]. The n-type conductivity of ZnO makes it appropriate for the applications in vacuum fluorescent displays and field emission displays.

ZnO has also extensively studied in catalysis application. For example, it has been utilized for methanol steam reforming process as a catalyst and catalyst support, leading to high selectivity to hydrogen. Hydrogen is a renewable and clean energy that

considered to be one of the promising energy source for the replacement of fossil fuels. Polymer electrolyte membrane fuel cells (PEMFCs), which run on hydrogen, are zero-pollutants emission systems because they transform the chemical energy of the electrochemical reaction within hydrogen and oxygen into clean electrical power [41]. Reforming of hydrocarbons, from which hydrogen can be extracted, allows a hydrogen production in situ and solve the transportation problem [42-44]. Among the fuel sources, methanol has advantages such as high hydrogen to carbon ratio and low activation temperature (200-300°C [45]) because of the absence of a strong C-C bond. However, the main drawback is the formation of carbon monoxide (as the equations below), which will poison the anodic catalyst of PEMFCs[46].

$$\boldsymbol{CH_3OH + H_2O \rightarrow CO_2 + 3H_2}$$

$$\boldsymbol{CH_3OH \rightarrow CO + 2H_2}$$

ZnO supported Cu catalyst is known to be selective to CO_2 and actively lower the reaction temperature[47]. It has been reported that it is the combination of Cu and ZnO but not pure metallic Cu that lead to the catalytic reactions. Another system, Pd/ZnO, is reported to exhibit comparable methanol steam reforming activity and have high CO_2 selectivity upon proper pretreatment [48], which is attributed from the formation of PdZn alloy on ZnO support. In addition, ZnO support was also found to affect catalytic activity and CO selectivity [49].

1.3.2 Crystal structure and chemical bonding of zinc oxide

ZnO is a key technological material. The lack of a center of symmetry and combined with large electromechanical coupling, resulting in its strong piezoelectric and pyroelectric properties. Such properties make the consequent use of ZnO in mechanical

actuators and piezoelectric sensors[36]. ZnO binding in crystal lattice involves an sp^3 hybridization of the electron state, which leads to four equivalent orbitals in a tetrahedral geometry. Molecules with tetrahedral geometry generally form either a zinc-blende crystal structure or a hexagonal wurtzite structure depending on the close-packed layer stacking sequences. The zinc oxide preferentially forms a hexagonal wurtzite crystalline structure with lattice parameters a=b=0.325nm, c=0.5204nm as shown in Figure 1.3a. The structure of ZnO can be simply described as a number of alternating planes composed of tetrahedrally coordinated O^{2-} and Zn^{2+} ions[36], stacked alternately along the c-axis, which is along the [0001] direction. There is a very small deviation in the axis ratio (c/a=1.602) from the ideal close-packed wurtzite axis ratio (c/a=1.633) because of the high polarity of the ZnO bond.

ZnO is an anisotropic material and thus has different values of surface energy for different faces. Spontaneous polarization along the c-axis and a normal dipole moment is produced by positively charged Zn (0001) and negatively charged O (000-1) c-planes. The polar surfaces also result in divergence in surface energy. the m-plane (10-10) surfaces and the a-plane (11-20) are non-polar faces with lower surface energy. This anisotropy leads to the preferential growth of ZnO along c-axis, as there will be higher degree of preferential atom/molecule incorporation on the polar faces rather than on the side non-polar faces.

1.3.3 Nanostructured zinc oxide

In the last few decades, study of nanostructured materials has provided many new insights into the fundamental understanding of nanoscale systems. With reduction in size, novel electrical, mechanical, chemical and optical properties have been discovered [36]. Surface and quantum confinement effects are of importance. The different surface

structures of ZnO could induce anisotropic growth, generating a variety of ZnO nanostructures. By controlling the growth kinetics, local growth temperature, and the chemical composition of the source materials, it is possible to tune the growth rate along different directions and a wide range of nanostructured ZnO can be grown, including nanobelts, nanoflowers, nanocages,nanorings, etc.[50-53].

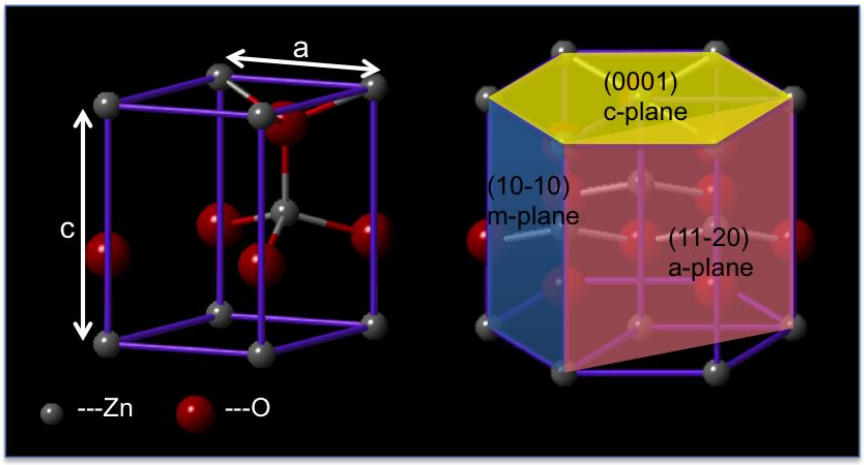

Figure 1.3 Schematic illustration of the crystal structure of ZnO.

The most common crystal faces on the 1D ZnO nanostructures are the (10-10), (11-20) and (0001) facets[36]. The highest growth rate in ZnO is along the c-axis and the large facets are usually {10-10} and {11-20}, which make the preferential growth of ZnO NWs along the [0001] direction. The single-crystalline zinc oxide NWs exhibit unique properties compared with bulk ZnO: (i) It is significantly stronger due to a reduction in the number of defects per unit length; (ii) it has superior electrical properties with electron field mobility, almost ten times than that of ZnO thin film transistors [54]; (iii) it has higher aspect ratio and large surface area, rendering ZnO NWs gas sensor sensitive and selective[55].

1.4 Growth of ZnO NWs

Wide ranges of techniques, both chemical and physical, have been used for growth of ZnO NWs. For example, physical vapor deposition (PVD)[56, 57], metal-organic chemical vapor deposition (MOCVD), molecular beam epitaxy (MBE) and pulsed laser deposition (PLD), have been used to produce ZnO NWs[58, 59]. Each method has pros and cons: Impurities introduced into ZnO NWs during the PVD process, poor deposition uniformity and low product yield by MOCVD and MBE, and the less controllability and reproducibility by the PLD method. Most importantly, for large scale production and usage costly synthesis methods cannot be practical. Although wet chemistry methods[60]are attractive it suffers from the poor dispersion of the produced ZnO NWs, which can influence the broad applications of the functionalized ZnO NWs.

1.4.1 Chemical Vapor Deposition (CVD)

Chemical vapor deposition (CVD) is a chemical process used to produce high quality, high-performance solid materials, which is broadly used to produce thin films. Nowadays, it is also adopted as a simple cost-effective means of preparing semiconductor NWs. Typically, precursors are transported to heated substrates, where they react and condense to make desired products. The by-products produced in this process are pumped out of the chamber. Several reaction parameters including temperature, gas flow rate, pressure and reaction time can be tuned to get the different products.

In a typical CVD process for the growth of ZnO NWs, either pure Zn powder or a mixture of ZnO and graphite powders are used as the Zn source to prepare ZnO NWs[61-63]. There are mainly two mechanisms, vapor-liquid-solid (VLS) and vapor-solid (VS) growth, reported for the CVD growth of ZnO NWs [61, 64]. In VLS mechanism, normally

transition metal or noble metal particles with controlled size and dispersion are used as catalysts to control the diameter of as-grown ZnO NWs. The metal nanoparticle forms a liquid eutectic and gaseous reactants dissolve progressively into the liquid droplet, leading to a supersaturated solution facilitating nucleation and growth. In VS mechanism, the Zn vapor condenses and oxidizes directly, working as a self- catalyzed growth of ZnO NWs. The Zn vapor was produced by the reduction of ZnO by graphite powder and then the zinc can be fully or partially oxidized by oxygen in the carrier gas and form ZnO or ZnOx onto the substrate. Although such methods are considered as simple for the growth of NWs, the NW yield is limited by the size and type of the substrates. In addition, the catalyst parameters need to be optimized for a controlled growth of ZnO NWs.

1.4.2 Aqueous chemical growth of ZnO NWs

Aqueous chemical, the term hydrothermal is also often used, growth method has also attracted a lot attention in the growth of ZnO NWs [60]. The main advantages for this method are low cost and easy scaling up; no need of metal catalysts; and low operation temperature. During the growth process, ZnO can be crystallized by the hydrolysis of Zn salts in a basic solution. Solution temperature and pH determine the number of Zn^{2+} intermediates, which has remarkable effects on the morphology of ZnO NWs. The length and density of NWs increase with increasing Zn^{2+} concentration. The minimization of energy in the reaction system is generally considered as the driving force for the NWs growth. Polar surfaces (0001), which have higher energies, have higher tendency to attract and adsorb the incoming ions and thus form ZnO NWs along the [0001] direction.

1.4.3 Modified vapor phase transport growth of ZnO NWs

In our work, we developed a catalyst-free and substrate-free modified vapor phase transport (VPT) method to grow ZnO NWs in large quantities. The final products are freestanding NWs in a shape of white cotton like flexible films. Since we do not utilize any catalysts and substrates we can grow ultrapure, clean and individually separable ZnO NWs. The functionalization of the synthesized ZnO NWs largely depends on these unique ZnO NWs growth processes, which will be discussed in detail in chapter 3.

1.5 Functionalization of ZnO NWs

Although each single component has its own functions, there are also limitations. It is considered that functionalized structures are a preliminary step for creating multifunctional nanosystems. The functionalization of ZnO NWs has been intensely investigated to exploit the functional properties arising from the interfaces.

1.5.1 Core-shell heterostructured ZnO NWs

One of the most common heterostructures is basically core-shell type NWs. A lot of metal oxide semiconductors shells, such as Al_2O_3, TiO_2, Bi_2O_3, Co_3O_4, SnO_2, ZrO_2 and other compound like ZnS, CdSe, CdTe, CdS have been explored to be grown on ZnO NWs core by different methods, including electrodeposition, hydrothermal reaction, photochemical reaction and ALD [16, 65-70]. In most cases, the shell layer, either polycrystalline or amorphous, has a strong influence on the properties of the core NWs. These HSs show significantly modified properties. For example, thin shells of amorphous Al_2O_3 /anatase TiO_2 coated ZnO NW arrays were reported to have improved performance for dye sensitized solar cell (DSC)[10]. The amorphous Al_2O_3 shells act as tunnel barriers that reduce recombination when it is very thin, but blocks electron

injection as it becomes thicker. Highly crystalline (thick) TiO_2 shells not only build a radical energy barrier that repels electrons from the surface of NWs but also enable more efficient electron injection and transport. Incorporation of ZnO/MgO core shell NWs in the solar cell resulted in substantive efficiency improvements of over 400% in comparison to the prinstine ZnO nanowire based photovoltaics[71]. The improvement of core-shell devices could be due to altering the bandgap, allowing for the interstitial states to create injection paths as an intermediate band solar cell. CdTe shell onto ZnO NWs core shows enhanced substantive efficiency in hybrid photovoltaic devices by enhancing the photoinduced charge generation and the photocurrent [70]. The adsorption of CdTe shell above its narrow bandgap and band alignment between the CdTe shell and ZnO core make it a promising photoelectrode. Improved photocatalytic activity is achieved by modifying ZnO NWs (a wide bandgap (3.37eV) and only absorb UV lights) with Bi_2O_3 coatings, enlarging the solar light absorption and reducing the recombination of photoinduced carriers [72]. Although the core-shell HSs are superior for modulation of certain properties, control on the thickness of the outside layers and formation of high quality interfaces between the shell material and the core NW are, however, challenging.

In our work, we uniformly coat the ZnO NWs with δ-Bi_2O_3 epi-layers via a simple one-step deposition process to improve the absorption efficiency of the visible light spectrum. The thickness of the δ-Bi_2O_3 layers can be well controlled below 2nm. The experimental data demonstrated that the deposited δ-Bi_2O_3 grows selectively and epitaxially on the {11-20} but not on the {10-10} facets of ZnO NWs. . The selective epitaxial deposition and the interfacial structure were thoroughly investigated. Based on the experimental data, we found that the growth of the δ-Bi_2O_3 on the ZnO {11-20} surfaces follows the

Stranski-Krastanov (SK) mechanism: an initial layer-by-layer growth followed by the formation of islands. The schematics of the selective and epitaxy growth of Bi_2O_3 is shown in Figure 1.4. In addition, we can also tune the morphologies of Bi_2O_3/ZnO nanostructures by modifying the deposition conditions. More details will be discussed in Chapter 4.

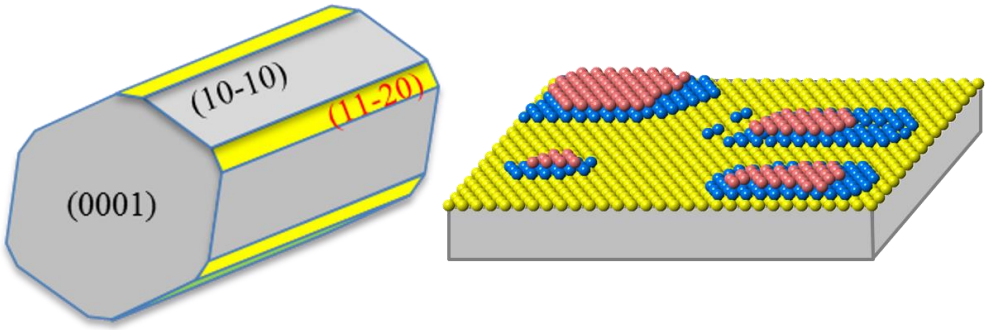

Figure 1.4 Schematics of selective and epitaxy growth of Bi_2O_3 layers onto ZnO NWs

1.5.2 Metal nanoparticles decorated ZnO NWs

Metal nanoparticle-decorated semiconductor NWs exhibit superior chemical, optical and electronic properties, which make them competitive in various applications, including catalysis, photonics and optoelectronics[73]. Different metals, e.g., Au[74-76], Ag[77, 78], Pt[79, 80], Zn[81], Pd[82-84], Ni[85] etc. have been used to decorate ZnO NWs by sputtering, wet-chemistry, electrodeposition and electron beam evaporation processes.

the decoration of Au and Ag particles on ZnO NWs has been carried out for the improvement of the UV emission and suppression of green emission in ZnO NWs. The enhancement is mainly due to the localized Surface Enhanced Raman Scattering (SERS) effect, which caused by a high density of hot spots on the surface of the ZnO NWs. The long-lived excitons in ZnO NWs and the localized electromagnetic modes in metal NPs make it possible to design specific optical responses and to explore new

phenomena as consequence of exciton-plasmon coupling, probably leads to breakthroughs in sensing devices[78, 86]. The exciton-plasmon coupling between Ag NPs and ZnO has been intensively studied by optical measurements [87]; it is also investigated by monochromated Scanning transmission electron microscopy-electron energy loss spectroscopy (STEM-EELS) in our previous report [88].

the use of bare ZnO NWs as a photocatalyst is limited by the photocorrosion phenomenon, which is caused by the UV radiation. As a result, the ZnO NWs catalyst has very poor stability and gives a dramatic decrease in catalytic activity [89]. The decoration of noble metals onto the ZnO nanowire surfaces changes the band structure of the ZnO through storing and shuttling photogenerated electrons from the ZnO to acceptors in photocatalytic processes [90, 91].

the electronic charge transfer and metal-support interaction also make metal NPs supported ZnO good catalysts for a variety of catalytic reactions. For example, Au NPs decorated ZnO NWs has been proved to have good catalytic performance in CO oxidation reactions [27, 34].Because of the strong interaction between Au NPs and the {10-10} surface of ZnO NW, Au NPs epitaxially grow into ZnO NWs and significantly improve the sintering resistance of the Au NPs. Such Au/ZnO NW catalyst is highly active for CO oxidation and has good stability at high temperature [34]. We have also reported that the Ag NPs decorated ZnO NWs has a much higher activity and better selectivity than pure ZnO NWs in Methanol Steam Reforming (MSR) reactions [92]. ZnO NWs supported Pt and Pd NPs catalysts are also extensively studied for methanol stream reforming reactions [22, 93]. Ni/ZnO NWs, reported as an adsorptive hydro-desulfurization catalyst toward kerosene-fed fuel cell applications [94], have also been developed[95].

In this work, Cu and Pd NPs were epitaxially grown on ZnO NWs to make them resistant to sintering at elevated temperatures and thus improved the stability of such catalytic systems for methanol steam reforming to produce hydrogen (Chapter 5). We also investigated the influence of particle size on catalytic performances.

1.5.3 Alloy decorated ZnO NWs: improved catalytic properties

Pd metals were reported to have good catalytic property over methanol decomposition to CO and hydrogen[96]. When supported on ZnO and reduced at temperatures higher than 300 °C, the formation of PdZn will occur and greatly increase the selectivity to CO_2[97]. However, higher loading or higher reduction temperature results in the aggregation of PdZn particles, which will influence the catalytic performance. Anchoring PdZn particles on the surface of ZnO provide a way to help stabilize the PdZn particles. A combined PVP assisted alcohol thermal procedure and impregnate method was used to prepare ZnO NWs and the deposition of Pd metals, respectively[35]. Depending on the Pd loading, Pd_xZn_y phases of various compositions are formed and stay stable on the nonopoar (10-10) facets of ZnO NWs. PtZn bimetallic/ZnO NWs catalyst was synthesized by heating the prepared ZnO NWs supported Pt catalysts under a reducing atmosphere when the temperature above 300°C [98]. Only when the molecular precursor species were uniformly coated onto the ZnO nanowires, which primarily consists of the low-energy and stable {10−10} nanoscale facets, the nucleation and growth of epitaxial PtZn nanoalloys will occur. These PtZn alloy nanoparticles decorated ZnO NWs exhibited very good durability under high-temperature water gas shift (WGS) and methanol steam reforming (MRS) reactions. In this work, we prepare PdZn epitaxially grow into ZnO NWs (as shown in Figure 1.5), showing with very high CO_2 selectivity and stabilized at elevated reaction temperature.

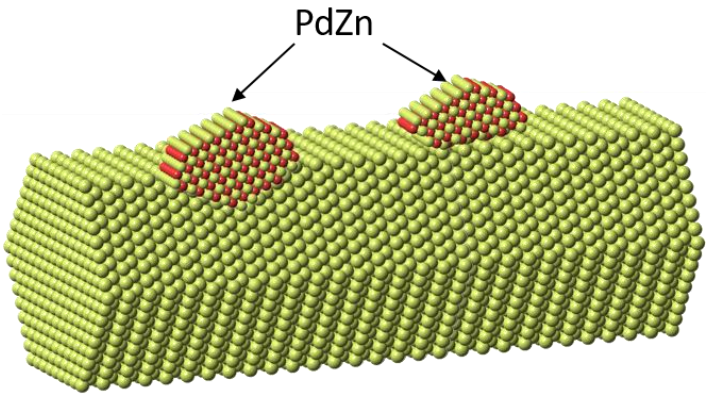

Figure 1.5 Schematic of PdZn NPs decorated ZnO NWs

1.5.4 Surface doped ZnO NWs for sensor and ZnO NWs supported Single Atom Catalyst (SACs)

Many experimental studies have examined ZnO NWs for gas sensing. They have been used successfully for the detection of a wide range of gases such as NO_2, H_2, C_2H_5OH, O_2, NH_3, CO, HCHO, acetone and CH_4 [99]. Functionalization of surfaces will further enhance the selectivity and sensitivity of ZnO NWs based sensor. For example, the concentration of OH groups can be tuned by treating ZnO NWs with hydrogen peroxide, resulting in variable electrical transport characteristics [100, 101].

Enhancement of sensitivity for hydrogen detection was demonstrated by depositing Pd clusters on ZnO nanorods [102]. In addition, by controlling the doping of ZnO NWs with Ga, the sensitivity of CO has been successfully customized[100]. A model study has been conducted on the doping of ZnO (10-10) surface with a wide range of dopants (such as Na, K, Au, Cu, Ti, Al, and Mg) and reveals that the dopant significantly altered the chemistry of the surface and its interaction with methanol[103]. All these studies suggest that modifying the surface properties of the ZnO NWs makes it possible to tune their sensing properties. The enhanced gas sensing performances are generally explained in terms of electronic and chemical modifications. In certain situations, the metal is

expected to act as an electron acceptor on support surfaces, which contributes to the increase of the depletion layer [104]. Therefore, the change in resistance is larger and the response is increased.

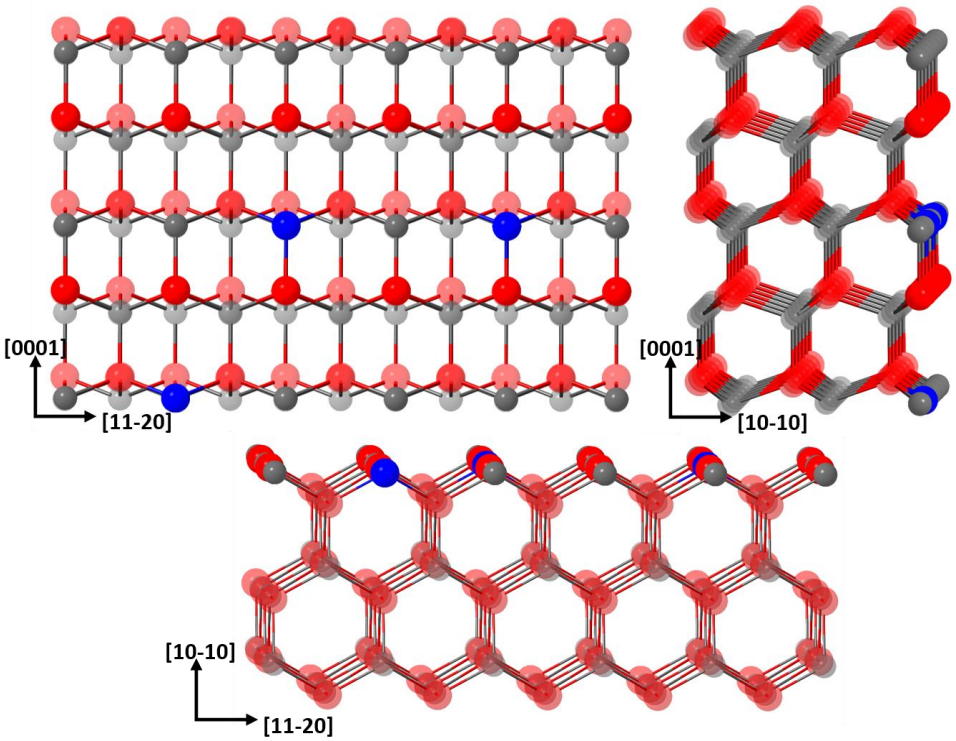

Figure 1.6 Schematic of ZnO supported single atom catalyst. The blue, grey and red balls indicate deposited single metal atoms, Zn atoms and O atoms, respectively.

Although supported noble metal NPs are among the most important catalysts that enable many critical technologies, they are expensive and of limited supply. Size reduction of NPs and even small clusters and single atoms catalysts will dramatically reduce the consumption of precious metals. Recent reports show that SACs are highly desirable not only for the cost reduction but also excellent catalytic performances [105]. The active centers in single atom catalysts (SACs) consist of isolated individual metal atoms and their immediate neighbor atoms of the support (see Figure 1.6). the strong metal-support interaction results in charge transfer and thus generate new ensembles,

which may possess unique catalytic properties different from those of the corresponding supported metal NPs. The interaction between these single atoms and support surfaces is determined by the geometric location of the metal atoms. With low levels of metal loading, the isolated metal atoms usually occupy the cation positions of the corresponding metal oxides. Figure 1.6 show the schematics of typical ZnO NWs supported single metal atoms catalysts, oriented form different directions. The single metal atoms occupy Zn positions on {10-10} surfaces of ZnO NWs. More experimental data and discussion will be in Chapter 6. As we mentioned above, semiconductor industry has been using doping a pure semiconductor to modify its electronic band structure and conductivity, such principle also works for catalysis applications. The change of local electronic structure can be used to tune the binding energy for reactant and/or product molecules[105]. Single Pt_1 and Au_1 atoms stabilized by lattice oxygen on the {10-10} surfaces of ZnO nanowires were used for methanol steam reforming (MSR) reaction[106]. The single Pt_1 sites is measured to be about three orders of magnitude higher than pure ZnO which is active for MSR as well.

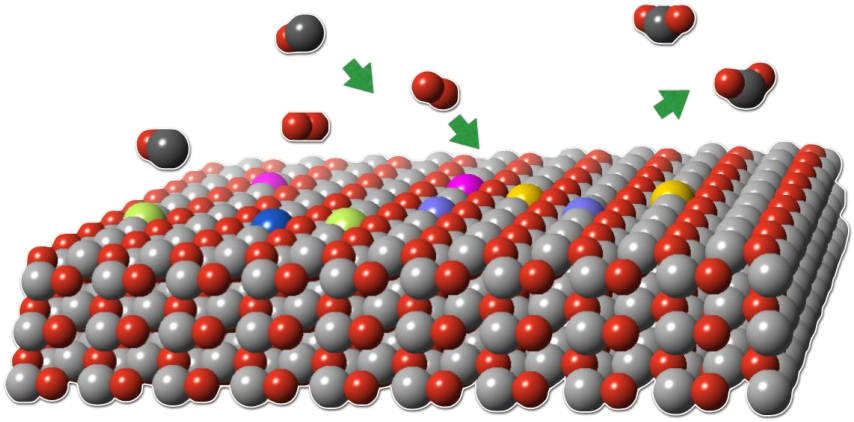

Figure 1.7 Schematic of M_1ZnO for CO oxidation

In this work, , We synthesized Pd_1/ZnO single-atom catalysts (SACs) by dispersing single Pd atoms onto ZnO NWs and evaluated their catalytic performance for selected

catalytic reactions. The experimental results show that the Pd_1/ZnO SAC is active for CO oxidation and MSR but is not desirable other reactions. We further synthesized ZnO NWs supported noble metal (M_1/ZnO; M=Rh, Pd, Pt, Ir) SACs and studied their catalytic performances for CO oxidation (Figure 1.7). The catalytic test data shows that all the fabricated noble metal SACs are active for CO oxidation but their activity are significantly different. Structure-performance relationships were also investigated.

Chapter 2 Methods

2.1 Growth of ZnO NWs

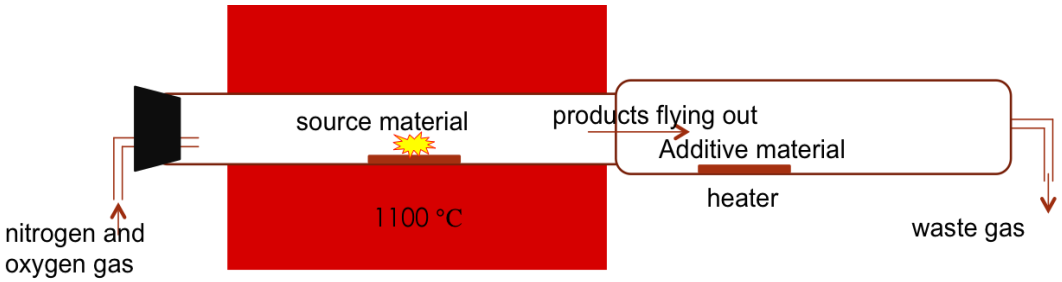

Figure 2.1 Schematic of experimental set up for the growth of ZnO NWs

the experimental set up for VPT growth is depicted in Figure 2.1a. Equal amounts (usually 1.5 g) of ZnO powder (99%, Sigma-Aldrich) and carbon black (Carbot Corp) are mixed together in a mortar. The resulting mixture is placed in a quartz boat and spread evenly over a boat with width of 2-inches and length of 8-inches. This boat is then placed in the center of a quartz tube with an inner diameter of 4 inches. A large clean quartz tube with inner diameter of 5 inches, nominated as collection tube, is placed outside the furnace and connected with the reaction tube. Another end of the furnace is attached to gas lines for oxygen and nitrogen. When grow pure ZnO NWs, the collection tube is blank and clean, without an extra heater and additive materials (Figure 2.1). The extra heater is designed and used for the functionalization of ZnO NWs, see section 2.2. The collection tube is open to external atmosphere via the exhaust and the pressure in the furnace is 1 atm. N_2 with a flow rate of 1L/min is used to purge the furnace for 15min before use. The furnace is then heated to 1100°C at a rate of 10°C/min and reacted for 30min with O_2/N_2 flow rate of 10/500sccm. More details will be shown in Chapter 3.

2.2 Methods for functionalization of ZnO NWs

2.2.1 Evaporation and deposition via VPT growth

the additive species were evaporated either in another zone of three-zone tube furnace or in a newly designed extra heater (Figure 2.1) among the process when ZnO NWs flying out along the reaction tube carried by the mixed gases. For the growth of overlayers that complete wet the surface of ZnO and to get designed specific high temperature phase, for example δ-Bi_2O_3, the species could be located on another high temperature zone, evaporated and deposited. For NPs do not wet the surface of ZnO and suffers from rapid sintering when the substrate temperature (ZnO) is too high, a designed extra heater were used, which is composed of boat-shape heating element and temperature control system can be placed outside the high temperature tube furnace. The species, for example silver, can be evaporated by the heater and deposited on ZnO NWs when the temperature of ZnO NWs is relatively low. Ag NPs, Ag clusters and Ag single atoms supported ZnO NWs can be synthesized benefits from this method.

2.2.2 Absorption and deposition via chemical synthesis

NPs were deposited onto the synthesized ZnO NWs via a modified deposition–precipitation method. Typically, ZnO NWs were dispersed into deionized water under stirring. Percursors awueous solution, such as $HAuCl_4$, $Pd(NO_3)_2$ et al., was added dropwise to the suspension, during which the pH value of the mixture can be tuned at a fixed value by simultaneously adding appropriate amounts of Na_2CO_3 solution. The suspension was then heated to 60 °C, stirred and aged for 2 h, respectively. Then the suspension was filtered and washed with deionized hot water for several times to remove the residual waste. The resultant solid was dried at 60 °C overnight. If needed,

they will continue be calcined in a muffle furnace and reduced in tube furnace in 5%H_2/He at various temperatures.

2.3 Methods for structural characterization and analysis

2.3.1 SEM Characterization

the morphologies of the prepared functionalized ZnO NWs were observed with scanning electron microscopy (SEM) using a JEOL JXA-8530F operated at 10~20kV.the electron beam interacts with the sample atoms in various ways, such as elastic or inelastic scattering, resulting in the production of different signals. Secondary electrons are ejected from the surface atoms by inelastic scattering with the beam electrons and it is the main emission type by which morphological and topological information is obtained from a SEM.

2.3.2 XRD characterization

the powder X-ray diffraction (XRD) measurements for the structure determination were carried on a PANalytical X'pert PRO X-ray diffractometer. The XRD patterns were collected using Cu Kα radiation (1.54 Å) at a voltage and current of 40 kV and 40 mA, respectively. The catalyst powder samples were scanned over the specific range according to different samples with a step size of 0.01-0.02° (specific with different sample) under continuous scan mode.

2.3.3 STEM characterization

High-angle annular dark-field (HAADF) electron microscopy images were obtained on a JEOL ARM-200F aberration-corrected scanning transmission electron microscope (AC-STEM) operated at 200 kV with a nominal spatial resolution of 0.08 nm in the STEM mode. Before the STEM experiments, the samples were ultrasonically dispersed

in 95% ethanol and then a drop of the solution was put onto lacy carbon supported copper grid. Since the intensity of HAADF images is directly related to atomic number, it is a strong technique to differentiate supported noble metals on ZnO substrates.

2.3.4 Cross-sectional specimen preparation from ultramicrotome

Although the synthesized thin ZnO NWs are ideal for electron microscopy observations, it is extremely difficult to examine the cross-sectional view of long NWs. The ultramicrotome is used in this work to prepare cross-sectional samples for STEM characterization. The ultramicrotomed thin sections (30-50nm by my operations) have a uniform thickness and retain the original elemental distribution in phases of the sample. This is used to examine the interfacial atomic structures of core-shell NWs in Chapter 4.

Typically, the composite NWs were embedded into resin capsules (Epon-812) and polymerized for 24h at 70°C. Then the cured block will be trimmed to small size under optical microscope. A diamond knife with a wedge angle of 45° will be used to section the sample and the sectioned slices will float on the surface of water. Collect the ultrathin sections carefully on a lacy-carbon film coated copper grids and coat the thin sections with a thin layer of carbon before STEM observation.

2.4 Performance characterization

2.4.1 Absorption performance

the ultraviolet-visible spectrophotometer is used to measure the intensity of light passing through a sample and compares it to the intensity of light before it passes through, the obtained ratio is transmittance and expressed as a percentage of T%. Also, the reflectance (R%) is also measured from the ratio of intensity of light reflected from

the sample and the light reflected from a reference material. The absorbance therefore is the complementary to the sum of transmission and reflection (A%=1-T%-R%).

2.4.2 Catalytic performance

2.4.2.1 Methanol Steam Reforming (MSR)

the methanol steam reforming (MSR) reaction test was carried out in a fixed-bed reactor with 50 mg of catalyst. The CH_3OH and deionized water were premixed and pumped to a helium (He) carrier gas and vaporized at 180°C. The final feed gas composition was 8 vol% CH_3OH + 12vol% H_2O and He balance. The total gas flow rate was 37 ml/min., providing a space velocity of 44,420ml·h-1g-1-cat. The reaction products were on-line analyzed by a gas chromatograph (Agilent 7890A, and thermal conductivity detector). The products detected are H_2, CO and CO_2 without any other products. The conversion rate of the MSR reaction was calculated based on the carbon balance.

2.4.2.2 CO oxidation

the catalytic performances of the prepared samples for CO oxidation were evaluated in a fixed-bed reactor. Typically, 0.05 g of the catalyst was loaded in a quartz reactor and fixed with quartz wool. Then, the feed gas, consisting of 1 vol% CO, 1 vol% O_2 and balance He, was allowed to pass through the reactor at a flow rate of 33.6 ml/min (corresponding to a space velocity of 40,400 ml/(h·gcat)). The effluent gas composition was on-line analyzed by a gas chromatograph (HP 7890) and a thermal conductivity detector. The CO conversion was calculated based on the difference between inlet and outlet CO concentrations.

For measuring the specific reaction rate, the CO reaction was conducted differently, where the CO conversion was controlled below 20 %. To achieve this purpose, specific

amount of the sample was diluted with Al_2O_3 and a much higher space velocity was used. The effect of external diffusion was excluded by proportionally varying the gas flowrate and catalyst amount. For each run at a specified reaction temperature, the CO conversions at 20, 40, and 60 min were averaged and used for calculating the specific rate.

Chapter 3 Growth of ZnO NWs

3.1 Vapor Phase Transport (VPT) growth of ZnO NWs

Among all kinds of methods available for ZnO NWs growth, VPT is one of the most straightforward and low cost methods. Generally, the growth happens in high temperature tube furnace at or close to atmospheric temperature. The zinc vapors were generated at high temperature and were carried by N_2/O_2 to the place where it is deposited. Substrate was placed in low temperature zone and collects the produced ZnO NWs in most of the VPT growth. In our work, by modify the growth method, another clean container (either quartz tube or big bucket), which is placed outside of the reaction tube, is used to collect the produced ZnO NWs (Figure 2.1a). This kind of growth eliminates the limitation of the substrate and can be scaled up the large amount.

Zinc vapor can be produced at relative low temperature (700-800K) by direct evaporation of Zn metal powders. But, based on our previous work, this will produce ZnO nanostructures with uncontrollable morphologies. For pure ZnO sources, significant sublimation takes place at temperatures>2250K. However, Zn vapor can be much easier to be produced at ~1200K by carbothermal reduction (CTR) as described by the following equations:

$$ZnO\ (s) + \frac{1}{2}C(s) \rightarrow Zn(g) + \frac{1}{2}CO_2(g)$$

$$ZnO(s) + C(s) \rightarrow Zn(g) + CO(g)$$

the experimental set up for the growth of ZnO NWs has already been described in Chapter 2. The temperature of the furnace is increased at a rate of 10°C/min to 1100°C,

which is the growth temperature and remain constant for 30min and then cooled to room temperature.

Table 3-1 Influence of temperature, mass of ZnO/C source and flow rate on the growth of ZnO NWs.

Condition / Influence	Temp. ↑	Temp. ↓	Mass(source) ↑	Mass(source) ↓	Flow rate ↑	Flow rate ↓
ZnO vapor	↓	↓	↑	↓	----	----
O_2 consumption	↓	↑	↓	↑	----	----
Continue growth	N	N	N	N	Y	N
Remaining species in boat	Grown ZnO(I)	ZnO Source(II)	Grown ZnO(I)	ZnO Source (II)	Carbon (III)	Grown ZnO(I)

3.2 Parameters that influence the growth of ZnO NWs

the quality and yield of the grown ZnO NWs are dependent on several parameters, including reaction temperature, mass of source, flow rate and carrier gas ratio, as shown in Table 3-1.

3.2.1 Furnace temp, mass of source and flow rate

Typically, the extent of growth can be categorized into three groups by the results of remaining species on the reaction boat: (I) White cotton like ZnO grown on top of the boat; (II) White powder like ZnO sources; (III) black carbon. Both type I and type II represent the non-complete growth.

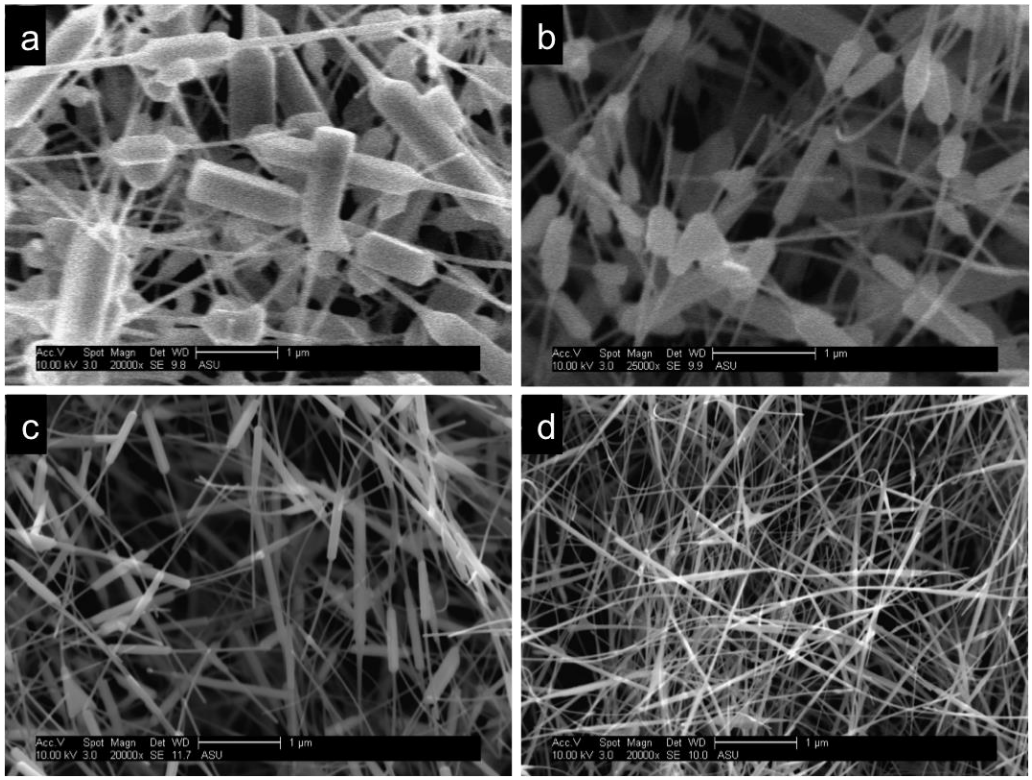

Figure 3.1 SEM images of ZnO NWs grown in the O_2/N_2 ratio of 0.21, 0.15, 0.1, 0.05. the aspect ratio of ZnO nanowire increases with the decrease of O_2 ratio. The scale bar is 1um.

When the temperature is too high (>1100°C), the source material (mixed ZnO and C) is massive, or the flow rate is too low, the resulted Zn vapor produced is very high and quickly react with oxygen to form ZnO. The rapid growth of ZnO will make them tangled together and blocked in the reaction tube. In this way, the reaction is quenched before the entire available powder mix is reacted due to re-deposition of ZnO on the powder surface with no carbon in the vicinity and hence the formation of an impermeable skin for longer growth period. On the contrary, low reaction temperature (<1000°C) and very less mixed source cause relatively low Zinc vapor. In this way, carbon in the mix will be consumed very quickly by oxygen and the remaining ZnO cannot produce Zn vapor at such temperature anymore. The remaining in the boat after reaction will be white ZnO powders haven't reacted yet. Only if have proper

temperature and amount of source material, and high enough flow rate to continuously transport produced Zn vapor and ZnO to the collection tube can all the reaction completed. There will be either nothing all small amount of carbon residue after reaction.

3.2.2 O_2/N_2 ratio in the carrier gas

As we concluded from last section, we need the overall flow rate large enough to get contiguous growth of ZnO NWs. Other than that, the partial pressure or the ratio of O_2/N_2 needs to be well controlled for the growth of ZnO NWs. The amount of O_2 must be small as the reaction between graphite and O_2 is energetically favorable. Otherwise, the graphite will be used up in the oxidation of Carbon instead of CTR of ZnO, like type (II) described in section 3.2.1. Performing growths at varying O_2 amounts and observing the resulted products allow us to determine the optimal ratio of the O_2/N_2.

As the main carrier gas is N_2 and there is also a need O_2 to grow ZnO NWs, we firstly use air as carrier gas to grow ZnO NWs and the results were shown in Figure 3.1a. It shows that a single nanowire is composed of two parts with diameters in large differences: a thick part in the middle or at one end of a nanowire with a diameter of about 500nm and a thin part in one or both ends with a diameter of about 50-80nm. By mix air with either oxygen or nitrogen to work as input gas, we can tune the oxygen ratio from 0.05 to 0.3. There is barely any growth of ZnO NWs when the oxygen ratio over 0.3 but quite thinner NWs growing with decreased oxygen ratio. The averaged aspect ratio of the NWs increases from 6 to 10, 50 and over 200 with O_2/N_2 ratio of 0.2, 0.15, 0.1 and 0.05, respectively (shown in Figure 3.1a-d).

3.3 Scale up: Large scale growth of ZnO NWs

the scale up the growth of ZnO NWs, we used a big three-zone tube furnace with a inner diameter of 4'' and collection tube with a inner diameter of 5''. By tuning the parameters we got a final optimized condition as: 3g mixed ZnO and carbon with a mass ratio 1:1 put in the right zone of the furnace with a constant temperature at 1100°C.

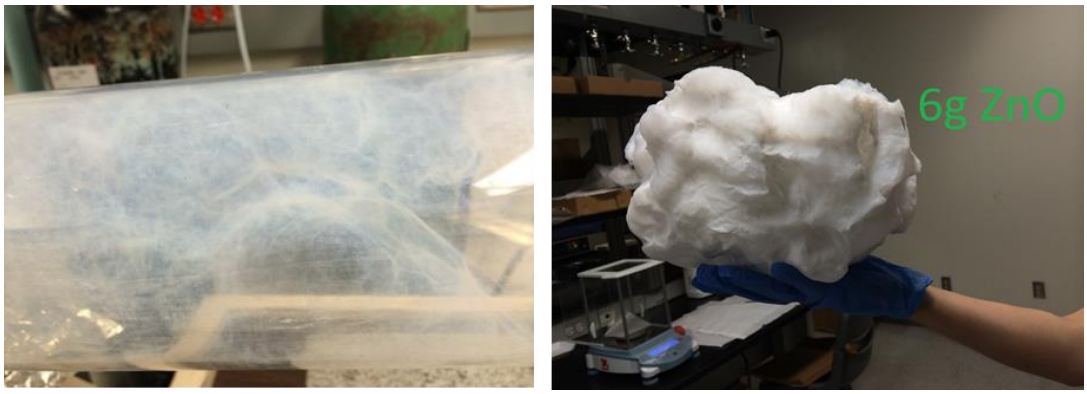

Figure 3.2 Large amount of synthesized ZnO NWs

the produced Zn vapor will be transported to collection tubes, which is room temperature by a high flow rate of 510sccm with O_2/N_2 ratio of 10:500. The reaction will be lasted for 30min each batch and the products will be collected for further application. The yield of ZnO NWs is about 500mg per batch and 2g per day, final product is shown in Figure 3.2.

the structure of synthesized ZnO NWs was shown in Figure 3.3. The diameter of the single nanowire is about 30nm with clean and flat {10-10} facets exposed. The preferential growth direction is identified as [0001].

3.4 Growth mechanism

As our method to grow ZnO NWs is catalyst and substrate free, in which the vapor-solid (VS) mechanism is generally considered to be responsible for the growth. It is

also proposed that the catalyst-free growth of ZnO NWs might include a self-catalyzed vapor-liquid-solid (VLS) process with Zn or ZnOx liquid droplets as catalysts[107].

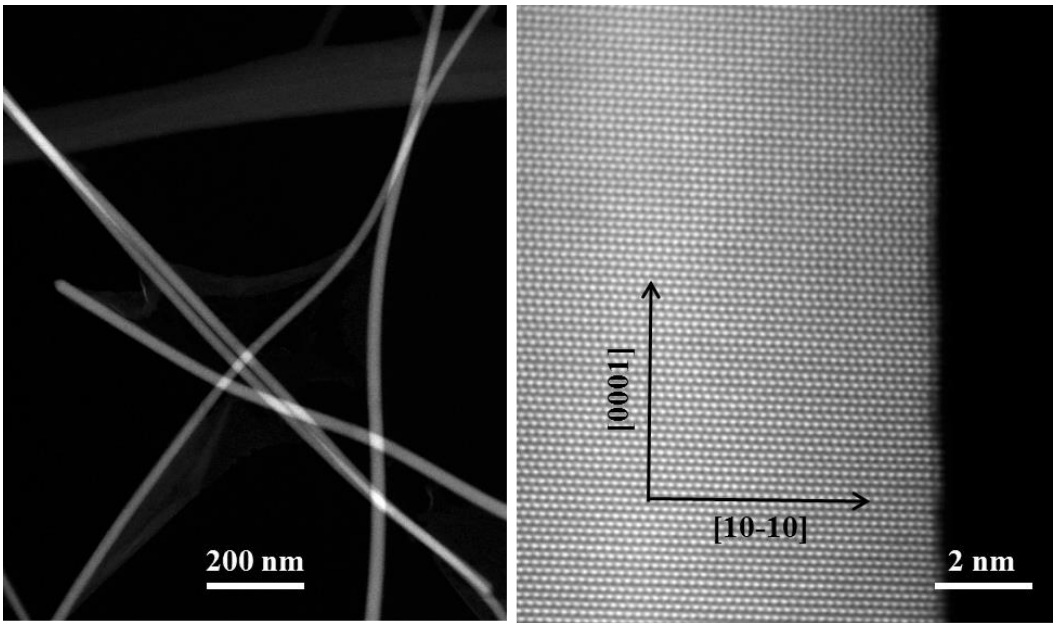

Figure 3.3 Low and high magnification HAADF images of ZnO NWs with a clean and flat ZnO {10-10} surfaces.

Various authors have suggested that ZnO growth proceeds via different paths. Kubo et al. Assume that ZnO molecular vapor condenses to form solid ZnO in their molecular dynamics simulation of ZnO homoepitaxial growth [108]. However, there is also other groups propose that Zn vapor is the condensing species and subsequently oxidized to form solid ZnO[109, 110]. In addition, Im et al. suggests a combination of both Zn vapor and ZnO condensation and the dominant process will be dependent on experimental conditions [111]. In our work, Zn vapor over condensed Zn is undersaturated at all temperatures, indicates that there are more molecules leaving the surface than arriving. However, the Zn vapor over solid ZnO is supersaturated at all temperatures, indicating that once a ZnO nanowire has started to grow, Zn vapor will be readily condensed and remain on the nanowire and oxidized to form ZnO NWs.

3.5 Interfacial atomic structures formed among ZnO nanowires

the interfacial structures of ZnO nanowires were also examined by STEM. Figure 3.4a shows low magnification HAADF image of two ZnO NWs attached to each other.

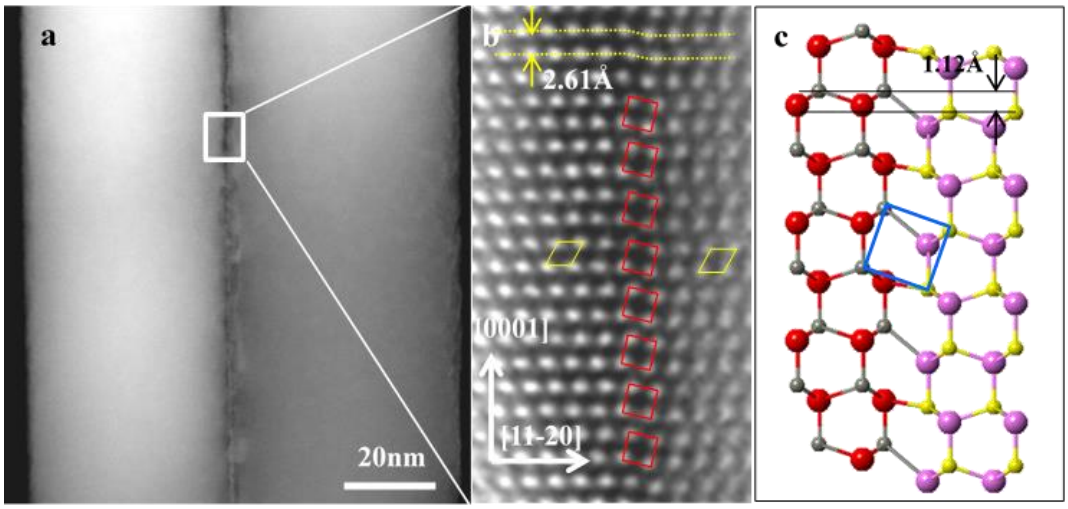

Figure 3.4 Low (a) and high (b) magnification HAADF images of a typical bonded ZnO NWs, revealing the atomic arrangement of the Zn columns at the interface region. The interface is marked by the red squares. The unit cell of the ZnO wurzite structure is indicated by the yellow paralleograms. (c) is the schematic illustrating the interfacial atomic arrangement viewed along the ZnO [11-20] zone axis.

Detailed examination of the contact regions revealed that atomic diffusion had occurred so that the two NWs bonded strongly to each other. The atomic resolution HAADF image (Figure 3.4b) clearly shows the positions of the Zn columns of both the ZnO NWs and the interfacial region. Both NWs possess the ZnO wurtzite structure. The theoretical unit cell of ZnO wurtzite structure is identified in Figure 3.4b (indicated by the yellow parallelogram) for both ZnO NWs. It appears that the two NWs shifted by about 0.11 nm along the [0001] direction. The interface structure is identified by the red squares in Figure 3.4b. The interfacial Zn-Zn bonding was measured to be 0.31nm, 7% longer than the Zn-Zn bonding in the NWs. Figure 3.4c shows a schematic diagram illustrating the interfacial atomic arrangement viewed along the [11-20] zone axis.

Chapter 4 Bi/BiO_x functionalized ZnO NWs

4.1 Selectively growth of δ-Bi_2O_3 epilayers onto ZnO NWs

4.1.1 Introduction

One-dimensional nanostructures have attracted broad interest because of their unique properties and potential applications. ZnO nanowires (NWs) have been extensively studied due to their applications in nanoelectronics[112], catalysis[20, 113], chemical sensing and energy storage[114, 115]. Functionalization of ZnO NWs can modify their physicochemical properties and make them suitable for desired applications. For example, ZnO-based hetero-nanowires have been investigated for applications in dye-sensitized solar cells[116-119] and photodetectors[120, 121]. Surface modifications of ZnO NWs have been reported to improve their emission properties in the UV region[77, 122] or to enhance their sensing properties for detection of CO molecules[123].

the different crystal facets of a single crystal NW usually exhibit different physical and chemical properties due to their differences in surface energies. Therefore, one can utilize this unique property to selectively functionalize the targeted surfaces for improved properties. For example, facet-selective growth of metals on Cu_2O has been reported to enhance photocatalytic[124] and electrocatalytic properties[125] because the {111} facets of octahedral Cu_2O have proven to yield much higher catalytic activity than the cubic Cu_2O enclosed by the {100} facets. Facet selective deposition of Au and Ag nanoparticles on $BiVO_4$ crystals achieved efficient charge separation on different crystal facets and resulted in much higher activity in photocatalytic water oxidation reactions[126]. Facet-selective growth of semiconductor compounds on Si NWs enabled the epitaxial growth of hetero-structures with large mismatches in lattice spacings[127].

In facet-selective epitaxial growth, the strained epilayer is limited to only the width of the facet, which can effectively alleviate the strain energy between the epilayer and the crystal substrate even if the lattice spacing mismatch is relatively large[127].

the photocatalytic activity of ZnO has been widely explored and reported[128]. Because of its wide band gap (3.37 eV) ZnO, however, only absorbs UV light, which accounts for only 5% of the solar energy. To significantly improve the photocatalytic activity of ZnO NWs, it is critical to increase the light absorption properties ZnO NWs without increasing the recombination rate of photoinduced carriers. We expect that selective epitaxial growth of thin layers of materials onto ZnO NWs with efficient absorption of visible light provide a versatile platform for broad applications in photocatalysis, photoelectrochemical conversions, etc.

Bismuth oxides are regarded as promising materials for applications in photocatalysis and optical coatings[113]. ZnO nanoparticles coated with different phases of Bi_2O_3 (α-, β-$Bi_2O_{3)}$ have shown increased light absorption and thus resulted in enhanced photocatalytic activity[129-131]. The coating of Bi_2O_3 onto ZnO can efficiently reduce the recombination rate of photon-induced electron−hole pairs[130]. For such hetero-systems, the interfacial structures become critical to the overall properties of the nanocomposite systems. For example, it is expected that epitaxial growth of Bi_2O_3 phases onto the surfaces of the ZnO NWs may further improve the photocatalytic performance of the Bi_2O_3/ZnO nanostructured systems. In this particular nano-structuring scheme, the ZnO core efficiently conducts electrons and provides mechanical strength while the combination with Bi_2O_3 shell enhances the electron transfer from ZnO to Bi_2O_3 and inhibits the recombination of photoexcited carriers[72].

In addition to the α- and β-phases of Bi_2O_3 discussed above, the fluorite-structured δ phase of Bi_2O_3 (δ-Bi_2O_3) is of interest because it exhibits much higher ionic conductivity, presumably due to the presence of higher concentrations of oxygen vacancies, than all other oxides. Such unique properties enable lower operation temperatures of the solid oxide fuel cells (SOFCs) and improve its efficiency and reliability[132]. The presence of higher concentrations of oxygen vacancies is expected to further enhance the absorption of visible light[133], which may provide improved properties than the other Bi_2O_3 phases for photocatalytic applications. For bulk materials, however, this high temperature phase is stable only within a narrow temperature window (729-825°C) and can easily transform to the other Bi_2O_3 polymorphs (α-, β-Bi_2O_3) at ambient temperatures[134]. Epitaxial growth of thin films of δ-Bi_2O_3 provide a route to effectively stabilize the δ-Bi_2O_3 phase even at ambient temperatures[132].

Luo et al. reported that in polycrystalline ceramic materials nanometer-thick disordered Bi_2O_3 films preferentially segregate and grow onto ZnO {11-20} facets while there were no such films detected on the {10-10} facets[18]. Crystallites of δ-Bi_2O_3 were occasionally observed to nucleate and grow the {11-20} surfaces of ZnO[135]. We expect that thin films of δ-Bi_2O_3 may be stabilized on the {11-20} nanoscale facets of the ZnO NWs. We report here, for the first time, the unique growth processes of thin layers of Bi_2O_3 onto ZnO NWs: Stable δ-Bi_2O_3 layers selectively and epitaxially grow onto the {11-20} nanofacets of ZnO NWs which are enclosed by {11-20} and {10-10} surfaces.

4.1.2 Synthesis

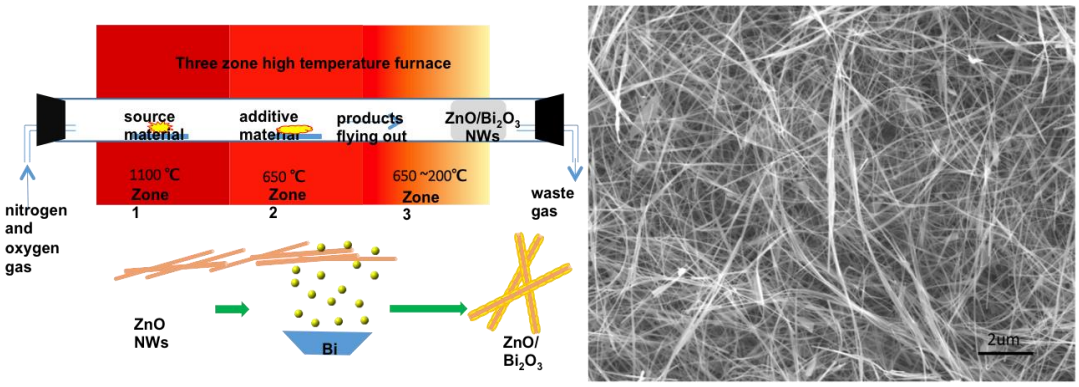

Figure 4.1 Illustrations of the growth of ZnO/Bi_2O_3 core shell NWs in three-zone tube furnace. SEM image shows high aspect ratio and uniformity of the product.

the Bi_2O_3/ZnO NWs were synthesized by a one-step, non-catalytic, and template-free physical vapor deposition process. Briefly, mixed ZnO and carbon powders, in a 1:1 ZnO/C weight ratio, were heated to about 1100°C and Bi powders were placed downstream of a high temperature tube furnace and were heated to a temperature that evaporates Bi atoms (Figure 4.1). ZnO NWs, formed in the high temperature zone, were carried, by the carrier gas such as Ar or N_2, to the low temperature zone where Bi atoms were deposited onto the surfaces of the pre-formed ZnO NWs. The thickness, structure and morphology of the deposited Bi/Bi_2O_3 species depend on the Bi partial vapor pressure, the deposition temperature, and the flow rate of the carrier gas. The morphology and size distribution of the synthesized Bi_2O_3/ZnO NWs were examined by high resolution scanning electron microscopy (SEM). Aberration-corrected scanning transmission electron microscopy (AC-STEM), with a nominal image resolution of 0.08 nm in the high-angle annular dark-field (HAADF-STEM) imaging mode, was used to characterize the atomic structure of the interfacial regions of the

Bi_2O_3/ZnO NWs. Cross-sectional TEM/STEM samples were prepared by the ultramicrotome technique.

4.1.3 Results and discussion

Compared to the chemical doping[136] and catalyzed vapor-liquid-solid (VLS) growth methods[137], our synthesis process produces large amount ultra-pure Bi_2O_3/ZnO NWs. XRD pattern (Figure 4.2) obtained from the synthesized Bi_2O_3/ZnO NWs clearly demonstrating that the produced material consisted of only wurtzite ZnO. The XRD pattern did not show any Bi_2O_3 or tertiary $Bi_xZn_yO_z$ phases[138]. As we will discuss later, only small patches of thin layers of Bi_2O_3, which would not be detected by the XRD technique, were present in the synthesized Bi_2O_3/ZnO NWs. The SEM image of the synthesized Bi_2O_3/ZnO NWs (Figure 4.1) shows the general morphology of the NWs with an average diameter of ~ 100 nm and length of ~10 micrometers, resulting in a high aspect ratio of about 100.

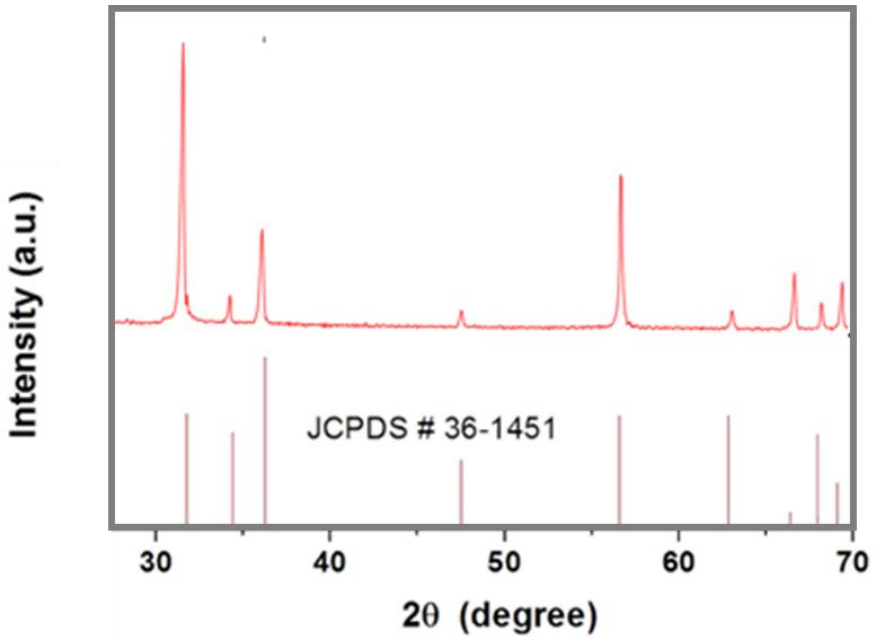

Figure 4.2 XRD pattern of the synthesized Bi_2O_3/ZnO NWs. All diffraction peaks can be indexed to the wurtzite structure of the ZnO (space group P63mc).

the XPS experiments were carried out to investigate the chemical nature of the deposited Bi-containing species on the ZnO NWs. Figure 4.3a shows survey spectra obtained from the pure ZnO NWs and the Bi_2O_3/ZnO nanocomposites, respectively. In addition to the presence of Zn and O a small amount of C was also detected from the pure ZnO NWs. The small amount of C may have originated from the exposure of the samples to air. For the Bi_2O_3/ZnO nanocomposite sample, the XPS spectrum clearly showed the presence of the Bi peaks as well as those of Zn, O and C. The 1s peak of graphitic carbon (BE=284.6 eV) was used as a reference to calibrate all the XPS spectra[139]. The O 1s spectrum of the ZnO NWs was de-convoluted into 2 separate peaks centered at 530.2eV and 531.6 eV. These two peaks correspond to oxygen ions in the wurtzite ZnO structure and the chemisorbed oxygen on the ZnO surfaces, respectively [140]. The Zn 2p core-level of ZnO NWs consists of two peaks located at 1044.5 and 1021.3 eV, representing Zn $2p_{1/2}$ and Zn $2p_{3/2}$, respectively [140].

the main peaks in the Bi 4f spectrum of Bi_2O_3/ZnO NWs correspond to Bi $4f_{7/2}$ (159.1 eV) and Bi $4f_{5/2}$ (164.5 eV), manifesting a typical Bi 4f spin–orbit doublet splitting of 5.4 eV. Compared with the Bi 4f peak positions of pure Bi_2O_3, a 0.6 eV positive shift of the Bi 4f peaks of the Bi_2O_3/ZnO NWs was detected. Such shift of the onset energy suggests a strong interaction between the Bi_2O_3 and ZnO phases. It has been reported that with intimate contact electron transfer from Bi atoms to ZnO can occur[141]. The pair of weak peaks located at an energy about 2.0 eV below the Bi 4f core lines is probably associated with the presence of oxygen vacancies[142], consistent with the reported high concentrations of oxygen vacancies in the δ-Bi_2O_3 [134].

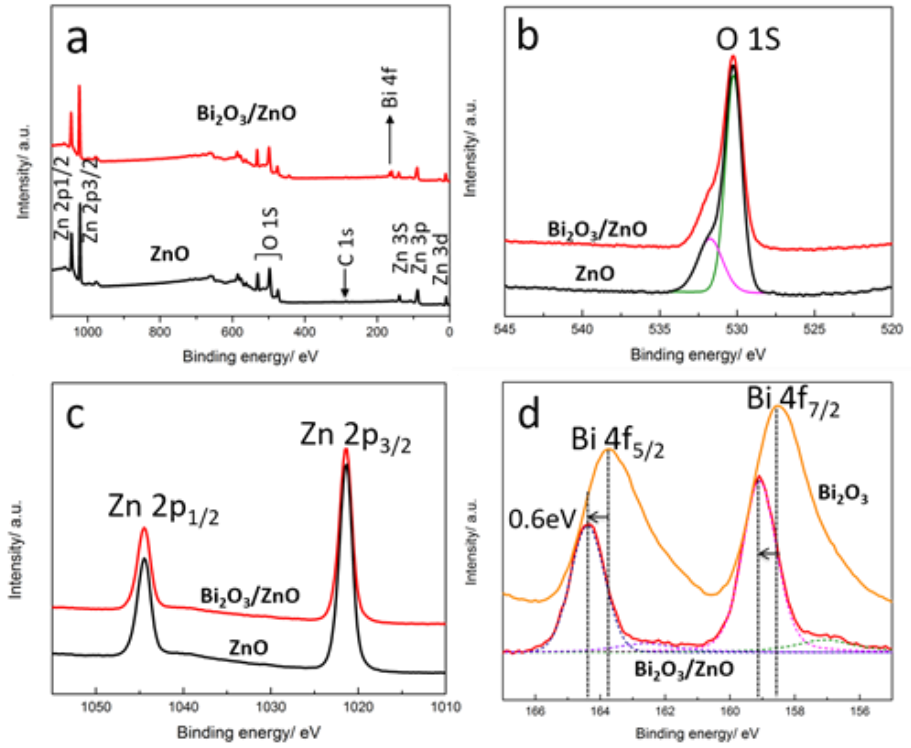

Figure 4.3 XPS spectra: (a) survey scan, (b) O 1s, (c) Zn 2p, and (d) Bi 4f of the δ-Bi_2O_3/ZnO NWs. The XPS spectra of the pristine ZnO NWs were also shown as reference.

HAADF-STEM imaging is capable of differentiating light elements from heavy elements [143, 144] because its image intensity is directly related to the atomic number of the probed species. Figure 4.4a, c shows low magnification HAADF-STEM images of typical Bi_2O_3/ZnO NWs with the electron beam oriented close to the ZnO [10-10] zone axis. In this orientation, the {11-20} and {10-10} facets that enclose the ZnO NW can be clearly revealed and indexed. The bright patches (indicated by the black arrows), which predominantly appear on the ZnO {11-20} facets, represent Bi-containing phases. Although some individual single Bi atoms were detected on the {10-10} facets one can conclude from Figure 4.4c that the Bi-containing phases selectively deposited onto the {11-20} facets of the ZnO NWs. HAADF-STEM images acquired with the electron beam along the ZnO [11-20] zone axis also clearly demonstrated the

preferential growth of Bi phases onto the ZnO {11-20} facets (Figure 4.4b). Similar bright patches can be observed on all the equivalent {11-20} facets (indicated by the white arrows in Figure 4.4c). In this viewing direction, the continuous layers and small islands of the Bi-containing species can be clearly discerned.

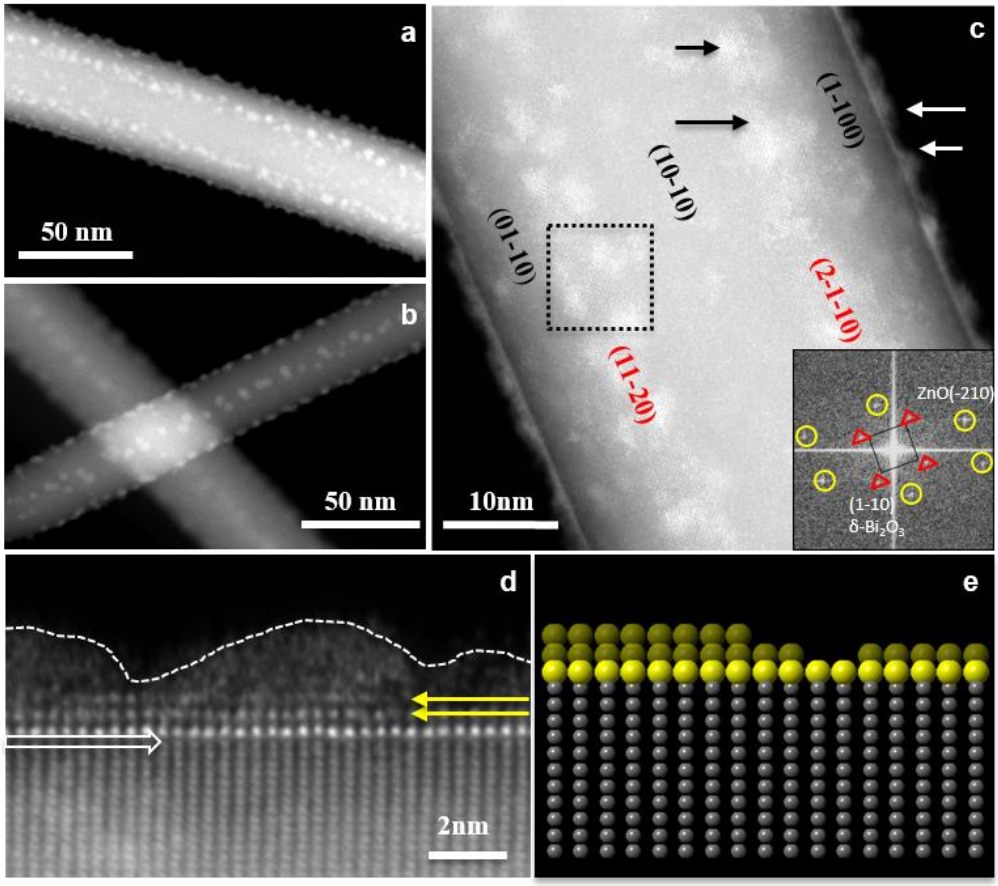

Figure 4.4 Low and high magnification HAADF-STEM images of typical δ-Bi_2O_3/ZnO NWs with the electron beam oriented close to the ZnO [10-10] (a, c, and d) and [11-20] (b) zone axis. The δ-Bi_2O_3 selectively grew onto the {11-20} facets of the ZnO NWs with an epitaxial relationship of ZnO [10-10] (11-20)||δ-Bi_2O_3[001](100) and a scheme of such epitaxy relationship is shown (e).

to identify the nature of the deposited phases, digital diffractograms were obtained from the high-resolution HAADF-STEM images. A representative diffractogram, which was obtained from the region encircled by the black square in Figure 4.4c, is displayed in the inset. The digital diffractogram contains two separate sets of diffraction spots: One

set of diffraction spots originated from the ZnO NW projected along the [10-10] zone axis and the other set was identified as from δ-Bi_2O_3 projected along its [001] zone axis.

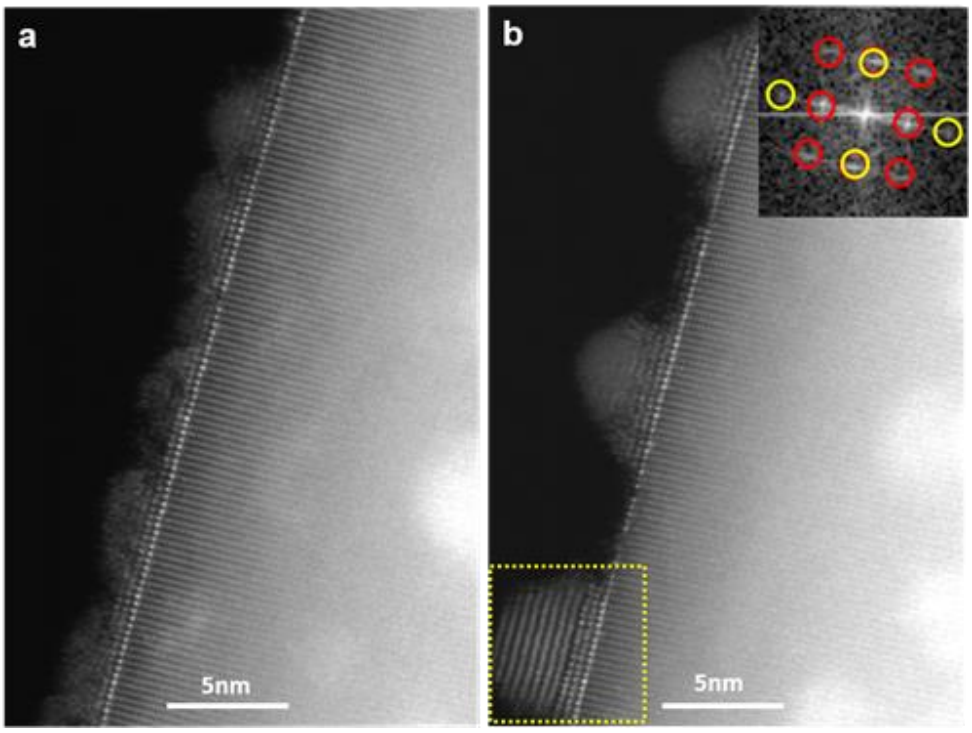

Figure 4.5 HAADF-STEM images of Bi_2O_3/ZnO nanowires show a) small amorphous-like islands on the almost continuous layer of bright dots which represent the Bi-containing phases and b) the formation of a few large Bi_2O_3 islands on thin layers of Bi_2O_3. The inset in (b) is the digital diffractogram of the region marked within the dotted yellow box. Two sets of diffraction patterns can be identified: One set represents ZnO[10-10] zone axis (yellow circles) and another set represents δ-Bi_2O_3 [001] zone axis (red circles).

Figure 4.5 shows another example of the growth of amorphous-like Bi-containing particles on thin layers of δ-Bi_2O_3. Occasionally, in addition to the thin layers some larger particles of δ-Bi_2O_3 were also detected (Figure 4.5b). It is clear that thin layers of δ-Bi_2O_3 phase can be stabilized by epitaxy. The epitaxy-stabilized δ-Bi_2O_3 phase in general only grow for 2-3 layers. Beyond this thin layer growth the Bi-containing species existed as highly disordered or amorphous-like particles.

the Bi_2O_3/ZnO interfacial structures are shown in the atomic profile imaging of Figure 4.4d. The brightest line (indicated by the white block arrow) represents the layer of Bi atoms projected along the [001] zone axis of δ-Bi_2O_3. The 2nd and 3rd layers of the δ-Bi_2O_3 (indicated by the yellow arrows) are less bright and seem to be discontinuous. Together with the intensity analysis of the δ-Bi_2O_3 patches in Fig. 1c we concluded that the 1st layer of the δ-Bi_2O_3 might cover large areas of the ZnO {11-20) facets while the 2nd and 3rd layers might form small patches. Beyond the 2nd or 3rd layers of δ-Bi_2O_3 small islands were formed as clearly shown in Figure 4.4c (encircled by the dotted yellow line). These small islands were not stable under electron beam irradiation and they did not show readily identifiable lattice fringes. Figure 1c and 1d clearly demonstrate that the δ-Bi_2O_3 layers grew epitaxially onto the {11-20} nanofacets of the ZnO NWs with an epitaxial relationship of ZnO [10-10] (11-20)||δ-Bi_2O_3 [001] (100), in agreement with the published results[145]. A schematic illustration of the growth the thin layers of δ-Bi_2O_3 is on the ZnO {11-20} facets is shown in Figure 4.4e.

to examine the interfacial structures between the ZnO nanoscale facets and the Bi_2O_3 phase, the ultramicrotome technique is used to prepare cross-section samples of the Bi_2O_3/ZnO NWs. A representative HAADF-STEM image of a typical cross-section sample (Figure 4.6a) clearly shows the 12 {11-20} and {10-10} nanoscale facets. The width of the {10-10} facets to that of the {11-20} facets is approximately 2:1, suggesting that the {10-10} are the dominant side surfaces of the 12-faceted ZnO NWs.

the deposited δ-Bi_2O_3 grew preferentially on the {11-20} rather than the {10-10} facets (indicated by black arrows). To our knowledge, the majority of the reported ZnO NWs either have six {10-10} or six {11-20} side surfaces and that these non-polar surfaces

consist of almost 80% of the total surface area[146, 147]. It is not clear if the presence of the Bi-containing phases modifies the growth morphology of the ZnO NWs.

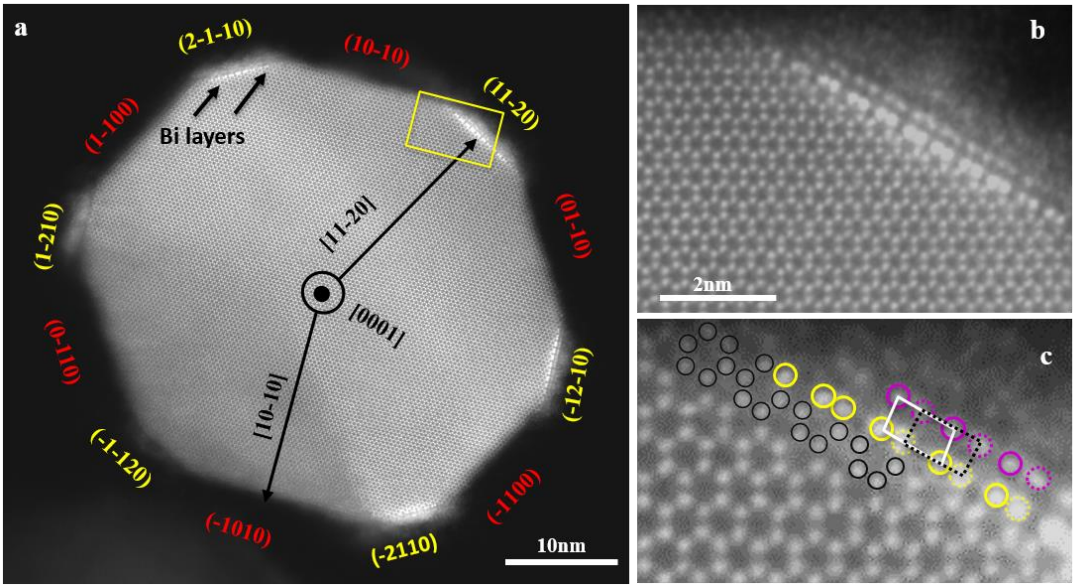

Figure 4.6 HAADF-STEM image of the cross-sectional view of a typical δ-Bi_2O_3/ZnO NW enclosed by the six {10-10} and six {11-20} side facets (a). Higher magnification image of the ZnO(11-20)/ δ-Bi_2O_3 (100) interface (b) and the atomic arrngement of the Bi and Zn atoms near the interfacial region (c). Black circles: Zn; yellow circles: 1st layer Bi; purple circles: 2nd layer Bi.

the magnified HAADF-STEM images (Figure 4.6b-c) unambiguously show the reconstruction of the Bi atoms at the interface. The first layer of the Bi atoms (marked by the yellow circles in Figure 4.6c) rearranges themselves to minimize the interfacial energy and allow epitaxial growth. The Bi atoms in the second layer (marked by the purple circles in Figure 4.6c) rearrange as well to accommodate the elastic strain. The original rectangle Bi unit (dotted black line in Figure 4.6c) is stretched to form a rhomboid (0.9 Å displacement along the ZnO [11-20] direction). Such a deformation becomes much smaller near the transitional region between the ZnO {11-20} and {10-10} facets.

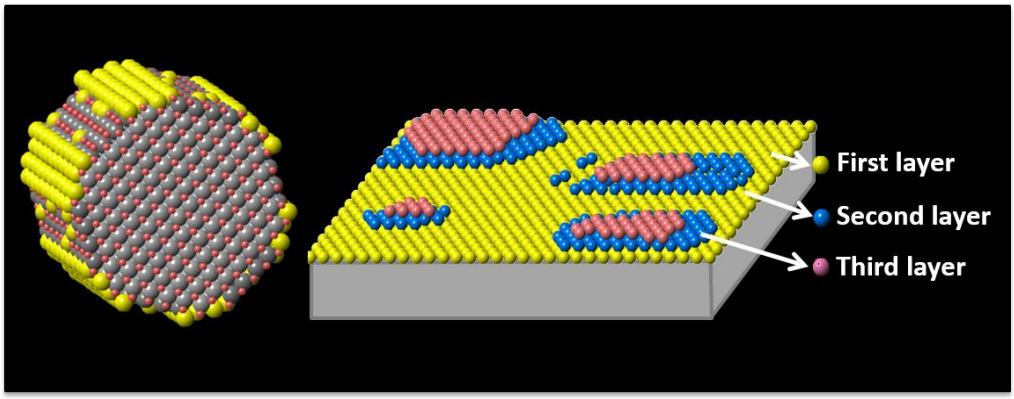

Figure 4.7 Schematic diagrams illustrate the proposed facet-selective growth of Bi_2O_3 on the {11-20} surfaces of the ZnO NWs (left panel) and the epitaxial layer growth of Bi_2O_3 on the ZnO {11-20} nanofacets.

Based on the analyses of the experimental data, a schematic model of the δ-Bi_2O_3 growth processes is proposed (Figure 4.7). The (100) facets of δ-Bi_2O_3 grow preferentially and epitaxially on the {11-20} facets of ZnO NWs. The fact that only a few isolated Bi single atoms were observed on the {10-10} facets of the ZnO NWs suggests that the sticking coefficient of the Bi species is extremely small on the ZnO {10-10} surfaces. On the other hand, the sticking coefficient of the Bi species and their binding energy on the ZnO {11-20} surfaces should be substantial to establish the epitaxy relationship. The growth of the δ-Bi_2O_3 on the ZnO {11-20} surfaces seems to follow the Stranski-Krastanov (SK) mechanism: an initial layer-by-layer growth followed by the formation of islands.

to fully understand the growth mechanisms of the epitaxial δ-Bi_2O_3 layers and the specific atomic arrangements of the different growth layers, plan view of the δ-Bi_2O_3/ZnO NWs were also examined. Figure 4.8a is an atomic resolution HAADF-STEM image of a δ-Bi_2O_3/ZnO NW projected along the ZnO [10-10] zone axis. In this orientation, the normal of the ZnO (10-10) nanofacet is parallel to the electron beam

while the normal of the ZnO (11-20) nanofacet is inclined 30° away from the electron beam.

4.1.4 Discussion on growth mechanism

the driving force for the preferential Bi deposition on the ZnO {11-20} rather than the ZnO {10-10} surface is most likely related to their surface crystal structures and the corresponding interfacial adhesion energies. The surface energy of ZnO {10-10} is smaller than that of {11-20}[148-150], which suggests that the {11-20} surfaces could be more active. According to Bravais' law, crystal planes with high atomic densities are more stable[151]. It is known that the density of atoms on the ZnO {10-10} is higher than that on the {11-20} surfaces. Therefore, the ZnO {11-20} surfaces may readily possess a high sticking coefficient for the Bi/BiO_x molecular species during the high temperature synthesis process. Epitaxy occurs in such a way that the total energy of the system, including the film-substrate, film-environment, and substrate-environment interfaces, is minimal. The interfacial energy of hetero-epitaxial growth, however, strongly depends on the nature of the hetero phases and the lattice mismatches[152, 153]. We analyzed the lattice mismatch between the ZnO and the δ-Bi_2O_3 epilayer. The mismatch between the ZnO(10-10) and the (100) of δ-Bi_2O_3 is approximately 2.6% while the mismatch between the ZnO(0001) and the (010) of δ-Bi_2O_3 is 8.2%. Although a mismatch of 8.2% along the ZnO[0001] direction is larger, the relaxation of the ZnO (11-20) surface along the [0001] direction[33] and the reconstruction of the first layer of the δ-Bi_2O_3 facilitates to accommodate the large mismatch. In addition, since the δ-Bi_2O_3 possesses eightfold-coordination polyhedral oxygen around the Bi atoms and 1/4th of the coordination oxygen sites are usually vacancies it is expected that the presence of oxygen vacancies may facilitate the formation of the epitaxial growth[36].

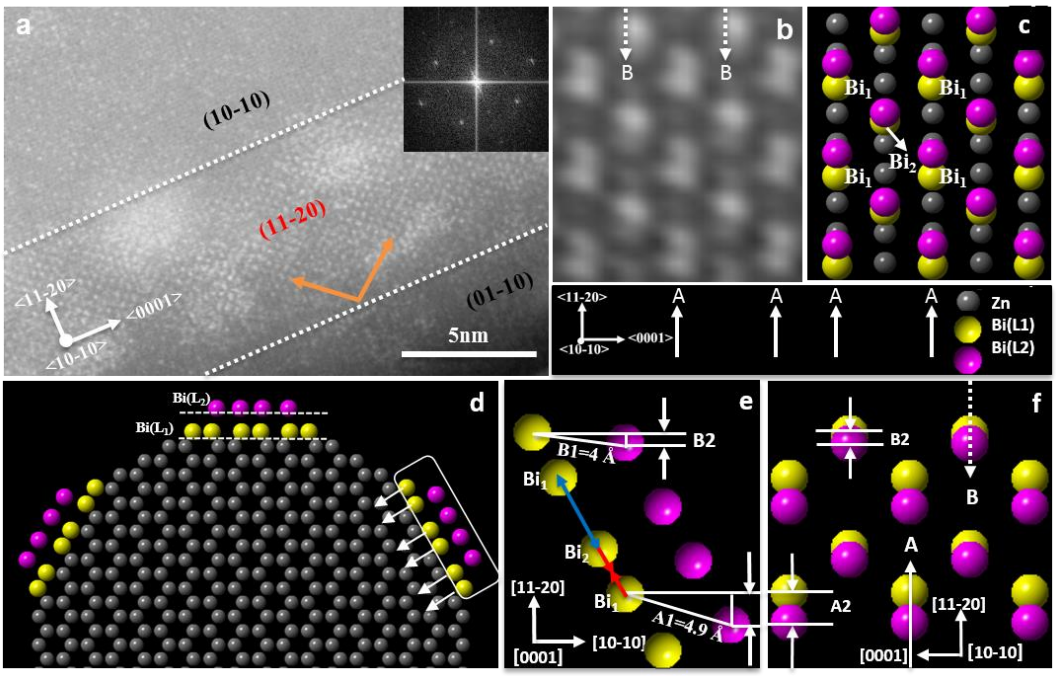

Figure 4.8 HAADF-STEM image of the δ-Bi_2O_3 layers epitaxially grown onto the ZnO {11-20} nanofacets with the incident electron beam along the ZnO [10-10] zone axis (a). Fourier filtered image (b) obtained from (a) to highlight the lattice fringes of the δ-Bi_2O_3 layers. Two columns of atoms were identified: the equal intensity dimers of column A (indicated by the solid white arrows) and the brighter atoms of column B (indicated by the dotted white arrows). The schematic (c) demonstrates the atomic configuration of the two layers of the Bi atoms with respect to the Zn atoms of the ZnO {11-20} surfaces. Grey balls: Zn; yellow balls: 1st layer of Bi; and purple balls: 2nd layer of Bi. The schematics (d-f) show the projection of the 2 layers of Bi atoms along the different viewing directions. The projection of 2 layers of the δ-Bi_2O_3 (100) along the ZnO [10-10] direction results in two closely spaced Bi atoms (B2=0.7 Å) for the B columns while for the A columns the distance is much larger (A2=1.4 Å). Due to the strong interaction between the Bi and Zn atoms, the reconstruction of the Bi layers resulted in the formation of different columns of Bi atoms with different lattice spacings (A1=4.9 Å and B1=4 Å). The projection of these reconstructed Bi atoms onto the ZnO {11-20} surfaces gives the observed image in b.

Because of the strong interaction between Zn and Bi atoms the locations of the interfacial Bi atoms must be adjusted to lower the interfacial energy between the ZnO (11-20) and the δ-Bi_2O_3 (100) interface (Figure 4.9).

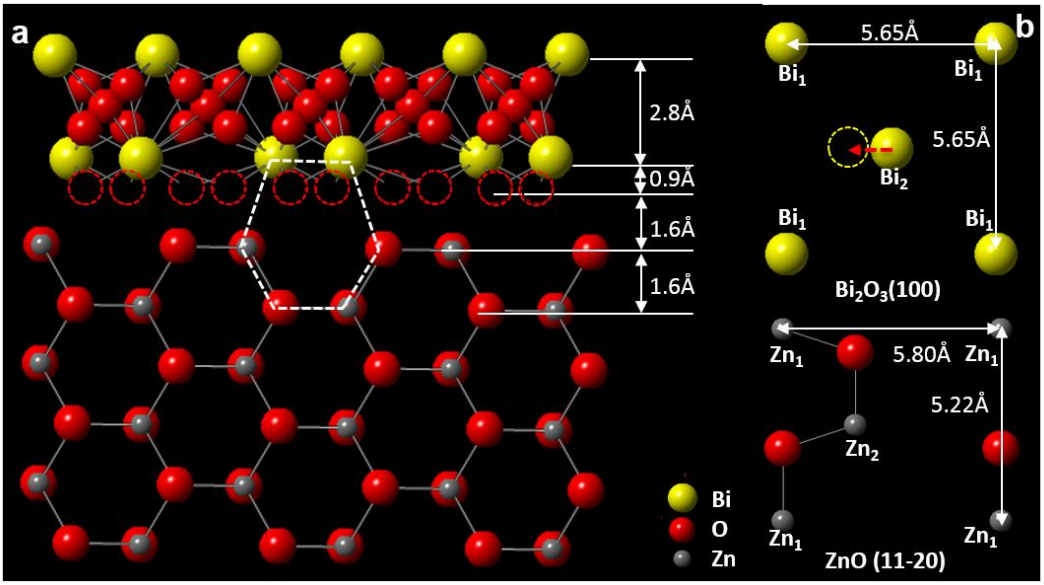

Figure 4.9 Preferential film formation at the {11-20} facets of ZnO can be understood as the existence of a low interfacial energy, due to epitaxy or ordering of the bismuth enriched film at this surface. The absence of film formation at the {10-10} surface can be attributed to either a low value of crystalline surface energy or poor epitaxy such that interface energy is not sufficiently low[36]. A high degree of lattice mismatch prevents the nucleation and growth of an over layer because of the large structural strain.

to accommodate the epitaxy relationship, the Bi atoms at the Bi_2 sites, in the first layer of the δ-Bi_2O_3 (100), should be strained by about 0.9Å towards the corresponding Zn sites, where the surface units of the ZnO (11-20) meet the surface units of the δ-Bi_2O_3 (100). When the second Bi layer grows the effect of the substrate is significantly reduced and the Bi atoms can grow at the regular sites of the FCC δ-Bi_2O_3. By measuring the distance between the Bi and Zn layers from the experimental images, which is 0.9 Å smaller than the adjacent Bi layers, we can propose models that explain the experimentally observed interfacial structure. It is possible that the Bi atoms substitute for the Zn sites of the ZnO and form bonds with the O atoms of the ZnO. Since the ionic radius of Bi^{3+} (1.20 Å) is larger than that of the Zn^{2+} (0.74 Å) [154]the

distance between the first layer of Bi and the first layer of Zn should be larger than the distance between the adjacent Zn layers. It is also possible that the Bi directly bonds with Zn (Zn-Bi bonding distances 2.5-2.9 Å have been reported) [155] .

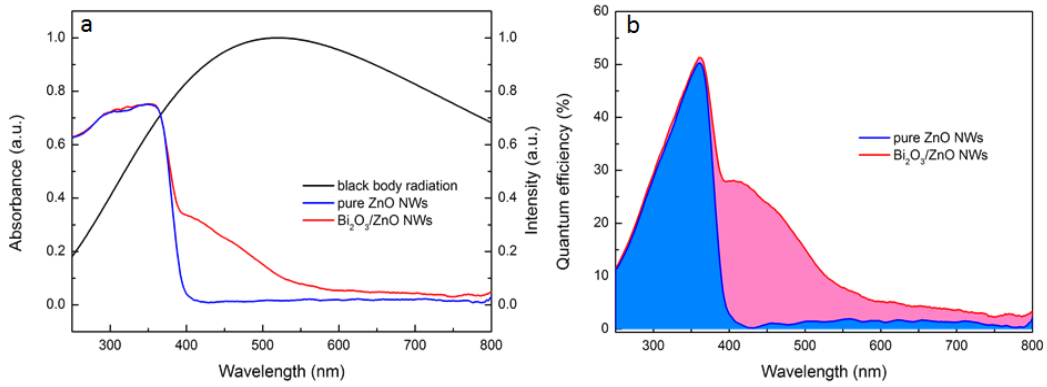

Figure 4.10 DRS spectra of the ZnO/Bi_2O_3 NWs and the calculated quantum efficiency. Compared with the efficiency of pure ZnO NWs (represented by the blue area). Bi_2O_3 functionalized ZnO improve the efficiency by 70%(red area)

Because of ZnO has wide bandgap, it only utilizes ultra-violet irradiation of the solar radiation. However, ultra-violet light accounts for only 5% energy of the sunlight. Surface modification of ZnO with Bi_2O_3 could efficiently enhance the absorbing ability over the visible spectrum. The DRS spectra of the Bi_2O_3/ZnO NWs were shown in Figure 4.7. The composite exhibited the similar absorption edge below 400nm, while an obvious visible light absorption band around 400-550nm was observed due to the narrow band gap of deposited Bi_2O_3 layers compared with ZnO. The black line in the Figure 4.10a indicates the black body radiation at 6000K, referring to the sunlight spectrum. Area in Figure 4.10b represents the quantum efficiency of photons radiated, which increased 70% by depositing Bi layers on ZnO NWs. The ability of light absorption in the visible range for the Bi_2O_3/ZnO composites makes it a good photo catalyst[72].

4.2 Influence of Bi_2O_3 on the growth of ZnO nanostructures

4.2.1 Introduction

In the past few years, much attention has been given to the possibility of controlling the size and shape of nanomaterials using growth-directed processes[156]. The composition and morphologies of HS play a key role in functionality. The synthesis conditions, as well as the dopants and additives to the substrate have remarkable effects on the morphology and size. A clear understanding of the underlying growth mechanism is important for tuning the morphology and to meet the demands of future applications.

Bi_2O_3/ZnO nanocomposite has been studied for its applications in photocatalyst[72, 157, 158]and nanovaristor[159, 160]. There is also reports on Bi-Au co-catalyze the growth of ZnO NWs[161]. Bismuth oxide is a kind of semiconductor with a narrow band gap, which is active under visible light irradiation[162] .By modify ZnO with Bi_2O_3, the light absorption is greatly enlarged and the recombination of photoincued carriers is reduced, which improve the photocatalytic activities of ZnO nanostructures. As sintering of ZnO with a small amount of Bi_2O_3 lead to the formation of a double Schottky barrier, nonlinear I-V characteristics for nanovaristors can be expected for Bi_2O_3 nanoparticles embedded ZnO nanostructures.

Although a lot of work has been done on the control of ZnO morphologies, best to our knowledge, there is no report on the morphology tuning by functionalize ZnO with Bi_2O_3 species. In this work, we present the growth of Bi_2O_3/ZnO nanostructures with different morphologies via a VS growth mechanism using a modified VPT growth method. By control the partial vapor pressure of Bi additives, we successfully tune the morphology of BiOx/ZnO nanomaterials from NWs to nanorods, and NPs.

4.2.2 Synthesis

the Bi_2O_3/ZnO nanostructures were synthesized in a high temperature tube furnace by a standard vapor phase transport process. The products were characterized by a FEI XL-30 scanning electron microscope (SEM) for observation of the general morphology of the different Bi_2O_3/ZnO structures. The JEOL JEM-ARM200F aberration-corrected scanning transmission electron microscope (STEM), with a nominal image resolution of 0.08 nm in the high-angle annular dark-field (HAADF) imaging mode, was used to investigate the atomic structure of the Bi_2O_3/ZnO structures.

to produce ZnO NWs, mixtures of ZnO and carbon powders are usually heated to high temperatures (e.g., 1100°C) to generate Zn/ZnO molecular species within the tube furnace; upon cooling down, these molecular species nucleate and grow ZnO NWs. When Bi powders were placed downstream and were heated to generate high Bi vapor pressure the morphology and the structure of the final product depends on the degree of mixing between the Bi vapor and the Zn/ZnO molecular species. By changing the amount of Bi additive and controlling the Bi partial vapor pressure, we can adjust the morphology and composition of the final products.

4.2.3 Results

SEM was used to examine the morphologies of Bi_2O_3/ZnO nanostructures. Figure 4.11a-f show the morphology variations of the Bi_2O_3/ZnO compound nanostructures when the Bi partial vapor pressure is decreased. With high Bi vapor pressure, big particles consisting of both Bi_2O_3 and ZnO were produced. When the Bi vapor pressure was decreased, thick and segmented microwires were produced (Figure 4.11a), where Bi_2O_3 and ZnO phases were separated and some Bi_2O_3 grew on the outside of the ZnO microwires, forming a core/shell structure (Figure 4.11b-d). With further reduction of

the Bi vapor pressure, ZnO NWs started to form (Figure 4.11e). When the Bi vapor pressure was extremely low and did not mix with the Zn/ZnO molecular species, ZnO NWs were produced (Figure 4.11f). However, aberration-corrected STEM images revealed that the surfaces of the ZnO NWs were coated with single Bi atoms or small clusters of BiO_x. Based on these observations, we propose that the presence of Bi or BiO_x species modifies the nucleation and growth of the ZnO micro and nano-structures; they facilitate the growth of ZnO on surfaces other than the {0001} surface, resulting in modified growth along different directions.

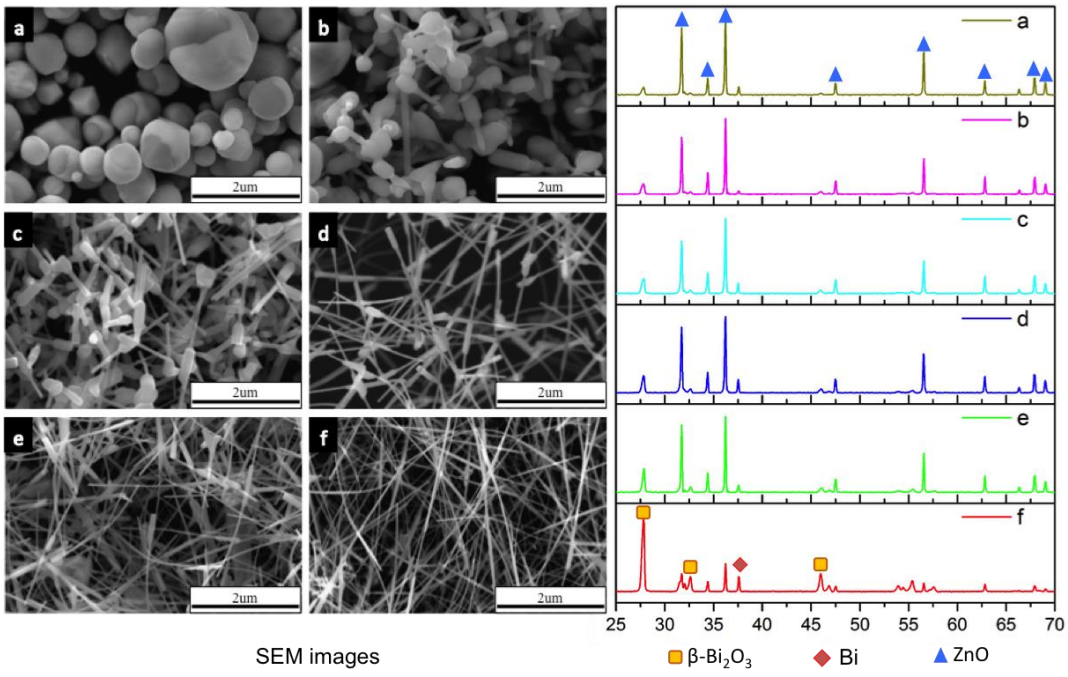

Figure 4.11 SEM images and corresponding XRD spectra of BiO_x/ZnO composites

the XRD spectra of Bi_2O_3 /ZnO HS in Figure 4.11 indicating that the HS are mainly composed of two crystalline phases, i.e., tetragonal β -Bi_2O_3 (ICSD #62979: a = 7.741 Å and c = 5.634 Å) and hexagonal wurtzite ZnO (ICSD #67454: a = 3.2501 Å and c = 5.2071 Å). Other than these two main crystalline phases, three small peaks were also detected and can be indexed to rhombohedral Bi (ICSD #64705: a = 4.533 Å, c = 11.797

Å). The detection of metallic Bi suggests that there is some metallic Bi remained in the structures, which could be probably in the core of the HS.

4.2.4 Discussion on growth mechanism

the growth mechanism of Bi_2O_3 /ZnO nanostructures can be attributed to the self-catalyzed vapor solid (VS) mechanism. Firstly, in the high temperature region, ZnO was reduced by carbon and a Zn vapor abundant atmosphere is provided in that zone. The produced zinc vapor will be continuously transferred to the low temperature region to form nanostructure. Among this process, Bi and BiOx vapor was generated by high temperature evaporation in the downstream low temperature zone (region I, II and III). Schematics in Figure 4.12 show that the growth of Bi_2O_3 /ZnO nanostructures is temperature dependent. The nucleation probability is determined by the temperature and supersaturation ratio in the vapor as shown in the equation by Blackley and Jackson's proposal [163].

$$P_N \propto \exp\{-[\sigma^2\pi/(k^2T^2 ln\alpha)]\}$$

Where σ is the edge energy per atom, k is the Boltzmann constant, T is the temperature in Kelvin, and α is the supersaturation ratio in the vapor. According to the equation, the probability of nucleation is strongly dependent on the temperature and supersaturation of the gas vapor[107, 164] . In our work, the temperature and supersaturation of the gas reactant are highest in ZnO source material zone, and decrease in sequence of region III, II and I. Thus, the nucleation of ZnO is predominant, when the ZnO nuclei or initial grown ZnO nanocrystal transferred into lower temperature zone, Bi or BiO_x molecules aggregate on the surface of ZnO nanocrystal and transferred to even lower temperature zone, finally form Bi_2O_3/ZnO nanostructures. Since the BiO_x molecules

at higher temperature region could move quickly to feed the continuous growth of the heterostructure, the average size of Bi_2O_3 /ZnO is larger than lower temperature region. In addition, the Bi evaporation location is also critical in our case. The further Bi source is located away from ZnO source material, the morphology of formed ZnO nanostructure is more likely to be NWs when BiOx deposit on the surface of it. After the deposition of Bi_2O_3, ZnO crystal lost the preferential growth toward ZnO [0001] direction. Thus, the gradient of evaporation temperature and distance towards ZnO source zone led the growth of Bi_2O_3/ZnO nanostructures from NPs to nanoribbons and NWs.

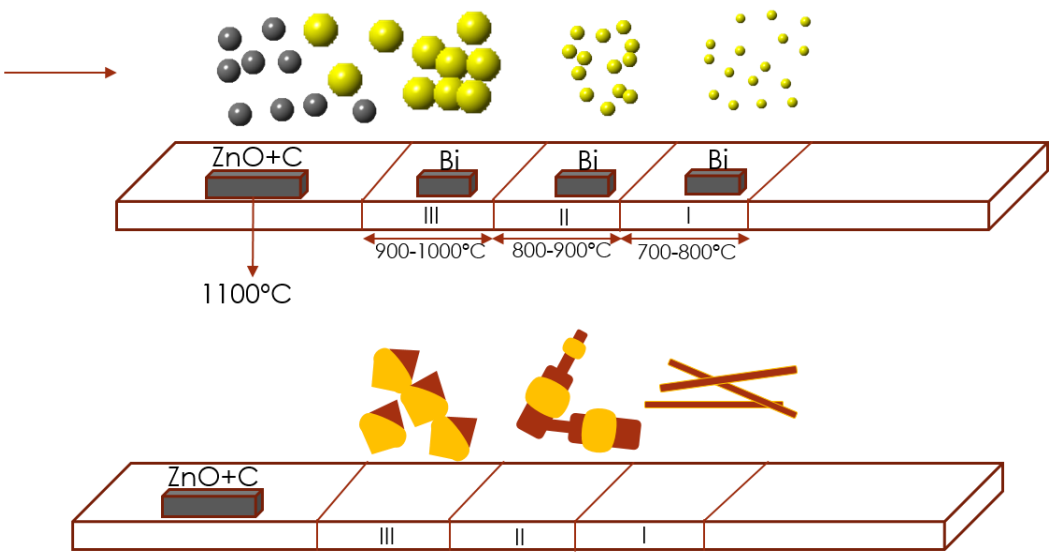

Figure 4.12 Schematics of the growth mechanism of Bi_2O_3/ZnO heterostructure.

When Bi sources are located at region III, there is sufficient Bi vapor and BiOx can nucleate on the side surface of the ZnO and further oxidized to Bismuth oxide. The reason why Bi_2O_3 were selectively grown on the side surface of ZnO crystal is probably related the surface and interfacial energy. Luo has reported that Bi_2O_3 is found to crystallize heteroepitaxially at the {11-20} surface of ZnO, the anisotropy was attributed to induce order between this surface and bismuth oxide structure, which may

lower the interfacial energy [135, 165]. Other works on the growth of Bi_2O_3/ZnO nanonecklace heterostructures also pointed out that Bi_2O_3 phase preferentially grow on the side surface of the ZnO NWs[166]. In addition, Bi_2O_3 is known to enhace grain growth of ZnO ceramics, which is controlled by the transfer of ZnO from small grains to large grains through a solution-precipitation process [167]. Thus, we propose that Bi_2O_3 may promote the lateral growth of ZnO crystals. When ZnO pass through the region III, the deposited bismuth oxide on ZnO is expected to melt (melting point 750°C) and resolve zinc vapor, followed by the precipitation of ZnO on non-polar surfaces and form the spindle like Bi_2O_3/ZnO heterostructures as shown in Figure 4.12(III). Bi catalyzed the lateral growth of ZnO along [11-20] direction has also been reported at low temperature [168].

When Bi sources is located at region II, nano-ribbons structured Bi_2O_3/ZnO can be obtained. Since few amount of Bi_2O_3 is deposited, it is hardly to differentiate the Bi_2O_3 phase and ZnO phase in the SEM images. HAADF imaging, in which the intensity is directly related to atomic number, is performed to show the distribution of Bi_2O_3 phase (Figure 4.13a). It shows that the short nano-ribbons are core shell structure with Bi_2O_3 (brighter phase) covered part of the ZnO side surfaces. This decrease of the amount of Bi_2O_3 phase can be explained by the lower Bi vapor pressure in region II. The growth mechanism in vapor solid (VS) have been proposed that atoms striking the surface will diffuse to the top and contribute to the formation of NWs [169]. ZnO nanowire growth are favorable at lower temperature zone since short circuit diffusion dominate[170]. Since the diffusion coefficient of zinc is higher than that of oxygen, zinc atoms strike on the surface of ZnO where there is no deposition of Bi_2O_3 shell will diffuse along [0001] grow into nanoribbon morphology. The aspect ratio of the nanoribbons is determined

by the competition of growth rate between the vertical preferential growth of ZnO along [0001] and the lateral growth in the solution-precipitation process affected by deposited Bi_2O_3 shell. When the size of Bi_2O_3 droplet is smaller, the enhancement of lateral growth of ZnO decrease and the short circuit diffusion dominate to grow along [0001] direction. At the same time, it activates the sintering of ZnO grains, work as a binder to link different ZnO segments, as shown in Figure 4.13c. By doing FFT from the high magnification image of the Bi_2O_3 films, the phase can be identified to be β- Bi_2O_3 oriented along [001] zone axis.

When Bi sources is located at region III with even lower Bi vapor, fine Bi_2O_3 particles with an average size of 5nm uniformly deposited on the surface of ZnO and will not influence the morphology of ZnO nanowire.

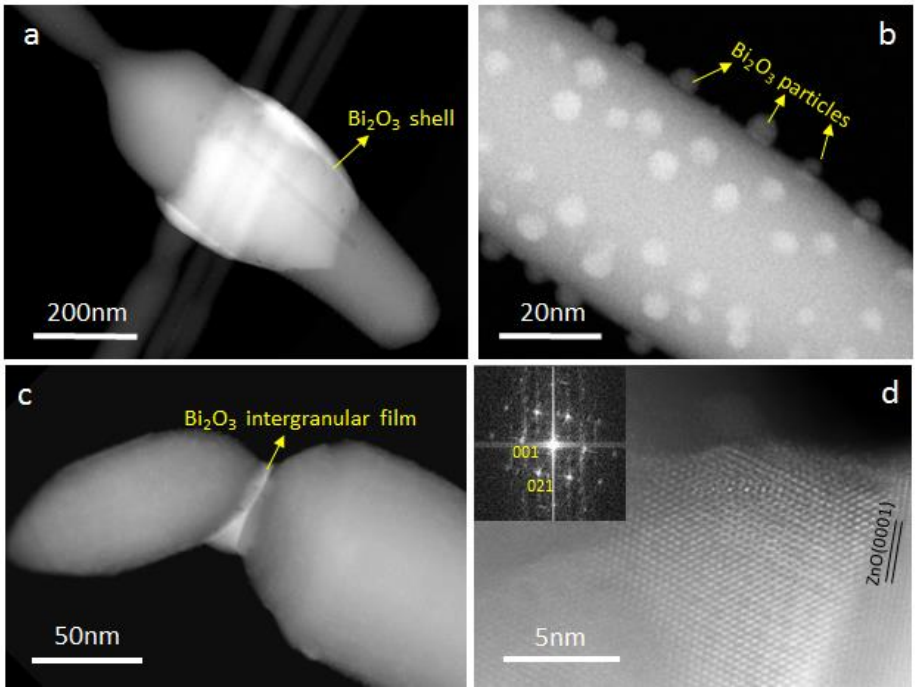

Figure 4.13 HAADF images of Bi_2O_3/ZnO heterostructures: (a) distribution of Bi_2O_3 shell (brighter region) on ZnO nanoribbon. (b) Small Bi_2O_3 nanoparticles dispersed on surface of a representative ZnO nanowire. (c-d) low and high magnification images of Bi_2O_3 intergranular film.

to summarize, Bi_2O_3/ZnO heterostructures has been synthesized in a one-step VPT process. The morphology of the HS can be tuned from NPs to nanoribbons and NWs by control the Bi partial vapor pressure. By studying the growth mechanism of such materials, we hypothesis that the influence of Bi_2O_3 additives on the morphology of ZnO NWs is caused by the competition between the vertical preferential growth of ZnO along [0001] and the lateral growth in the solution-precipitation process affected by deposited Bi_2O_3. This work can also be employed in other semiconductor systems and further tune the chemical and physical properties of the nanomaterials.

Chapter 5 ZnO supported metal NPs catalysts for methanol steam reforming

5.1 ZnO supported Pd catalysts

5.1.1 Introduction

there has been a growing interest on developing technologies that taking advantage of clean energy resources. Hydrogen, as an energy carrier useful for various applications, has gained a considerable interest for various applications, particularly for polymer electrolyte membrane fuel cells (PEMFCs) supply. PEMFCs are zero-pollutants emission systems because they transform the chemical energy of the electrochemical reaction within hydrogen and oxygen into clean electrical power [41]. Reforming of hydrocarbons, from which hydrogen can be extracted, allows a hydrogen production in situ and solve the transportation problem [42-44]. Among the fuel sources, methanol has advantages such as high hydrogen to carbon ratio and low activation temperature (200-300°C [45]) because of the absence of a strong C-C bond. However, the formation of carbon monoxide, which will poison the anodic catalyst, must be controlled lower than 10ppm [46]. Copper based catalysts have been commonly used for the methanol steam reforming (MSR) due to their high activity and selectivity, but suffer from the deactivation caused by thermal sintering at high temperature [171]. Pd/ZnO, which exhibited comparable methanol steam reforming activity as the Cu based catalysts and have low CO selectivity upon proper pretreatment, is also found to have high thermal stability [48]. Since the formation of PdZn alloy on ZnO support attributed to the low CO selectivity, a lot of studies have been done to effects of the PdZn particle size and the extent of PdZn alloy formation [35]. In addition, ZnO support was also found to affect

catalytic activity and CO selectivity [49]. Recently reported unsupported intermetallic PdZn catalysts exhibited limited activity and very high selectivity to CO in MSR [172], whereas the presence of oxidized Zn in near-surface region in the system of PdZn/ZnO was attributed to a high CO2 selectivity [173] . However, It was reported that when the loading of Pd decrease to 0.5wt%, where small PdZn bimetallic particles on ZnO could be expected, shows a very high CO selectivity[174]. The reason why low loading Pd lead to a poor performance in selectivity still needs to be studied.

In this work, different loadings of Pd on faceted ZnO NWs, different pretreatment conditions will be discussed, and our work shows the CO selectivity is strongly dependent on the Pd particle size and we also found that not only PdZn alloy have low CO selectivity but also the single dispersive Pd atoms. The highest CO selectivity at about 0.5%Pd loding comes from the metallic Pd clusters dispersed on surface of ZnO NWs.

5.1.2 Synthesis and pretreatment

A series of Pd/ZnO catalyst were prepared by a modified adsorption method. Briefly, noble metal precursor was mixed with the pre-formed ZnO NWs. The nominal loadings of Pd were 0.05 wt%, 0.1wt%, 0.5wt%, 1wt% were made by drop Pd $(NO_3)_2$ precursor solution into ZnO NWs. For high loading (2wt% and 5wt%) Pd/ZnO catalysts, Na_2CO_3 solution are simultaneously dropped into the solution to control the PH value within a range to maintain the shape of ZnO NWs. The resultant precipitate was filtered, washed and dried. High loading Pd/ZnO samples were calcined in air and reduced in 5%H_2/He before catalytic test. The catalytic performance of the synthesized catalysts for MSR was evaluated in a fixed-bed reactor. 50-200mg of Pd/ZnO catalysts (based on the loading) was loaded between two layers of quartz wool inside the reactor. A pre-

mixture feed of water/methanol (volume ratio of 1:1) was pumped into the reactor at 160°C and carried by flowing He with a flow rate of 33 ml/min. The outlet gas compositions were on-line analyzed by a gas chromatograph and the CO conversion was calculated based on the inlet and outlet CO concentrations.

to analyze the influence of synthesize condition (PH value) and pretreatment (reduction temperature and time) to the performance of Pd/ZnO catalysts, another series of samples synthesized at different PH values were made and reduced in 5%H_2/He at different temperatures. Following the reduction, these catalysts were cooled to 160 °C for catalytic evaluations.

5.1.3 Results and discussion

5.1.3.1 STEM investigations of structure and composition of Pd/ZnO catalysts

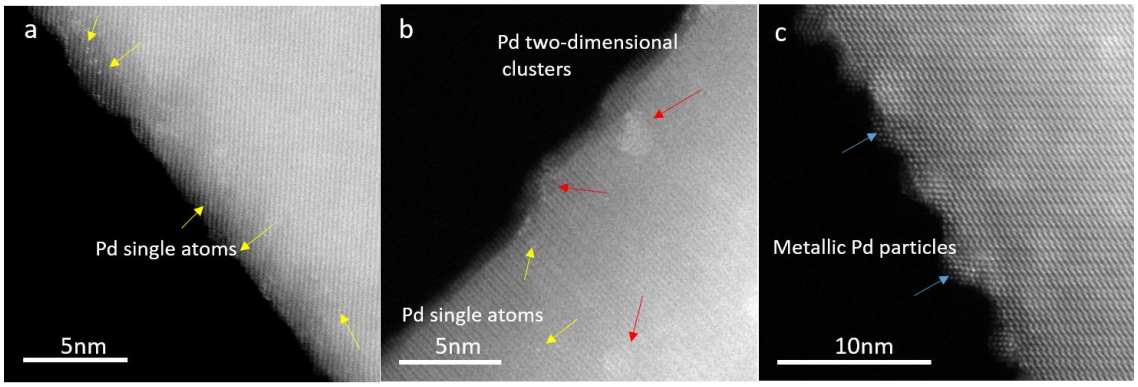

Figure 5.1 High magnification HAADF images of single Pd atoms supported ZnO catalyst (a), single atoms and small clusters supported ZnO catalyst (b) and epitaxially grown, ultrafine metallic Pd NPs(c). The single atoms, small clusters and Pd NPs are indicated by yellow, red and blue arrows, repectiviely.

the pre-prepared ZnO NWs were grown along [0001] direction with an aspect ratio over 100, predominant exposure is identified as {10-10} facets. Because of this morphology can be maintained at elevated temperature, so it can be applied in high-temperature

catalytic reaction such as MSR even at 700K, suggesting that ZnO NWs support itself is stable for MSR.

Figure 5.1 and Figure 5.2 are the HAADF images showing the dispersion of decorated Pd species. It is clearly that the size of the Pd species, from single atoms to NPs, is strongly depended on the loading of Pd. For the 0.05wt%PdZnO catalyst, only Pd single atoms (indicated by yellow arrow in

Figure 5.1a) can be observed on Zn sites. With the increase of Pd loading to 0.1wt%, both single Pd atoms and two-dimensional Pd clusters can be observed, indicated by yellow and red arrow, respectively in

Figure 5.1b. The STEM images of 0.5wt%PdZnO catalyst (

Figure 5.1c and Figure 5.2a) show the uniformly distributed small Pd particles grow on ZnO surfaces with a mean particle size of 1.5nm. When the loading was increased to 2wt% and 5wt%, their mean particle sizes increased to 3.5nm and 4.4nm, respectively (Figure 5.2b-c). For the three catalysts, there exists some amount of very small metallic particles; however, with the increase of Pd loading, the fraction of large particles as well as the average particle size increases.

to explore the phase and composition of the Pd/ZnO catalysts, higher magnification of HAADF images were taken to identify the surface and interfacial structure of Pd/PdZn particles. Figure 5.3a-b show the representative Pd or PdZn NPs grown on the ZnO NWs with Pd loading of 0.5wt% and 2wt%, respectively. The spacing between ZnO planes, which Pd particles were deposited on, is 0.16nm, confirms that the predominantly exposed ZnO facets are non-polar {10-10}. The {10-10} facets are considered of primarily clean, flat and well defined. Pd-like phases, either face centered

cubic (FCC) metallic Pd or a solid solution of Zn in FCC Pd, with a ratio of Pd to Zn much larger to 1, were observed on the 0.5%wt PdZnO samples. Reported CO-FTIR results indicate that metallic Pd like phase was present when the Pd loading or reduction temperature is low [35].

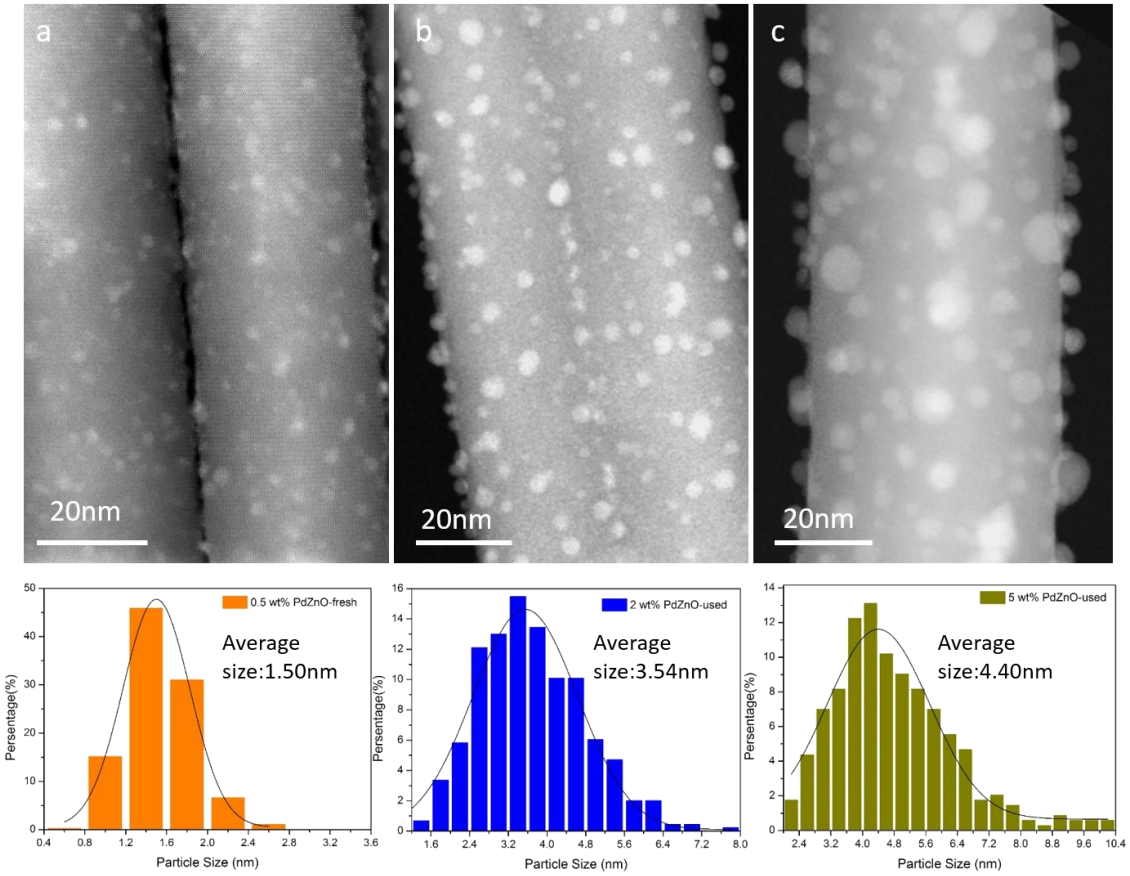

Figure 5.2 Low magnification HAADF images show particle distributions of PdZnO with Pd loadings of 0.5wt%, 2wt% and 5wt%. The mean size of the particle sizes is 1.5nm, 3.54nm and 4.4nm.

Corresponding schematics in Figure 5.3a clearly show that the epitaxially grown Pd NPs were highly faceted with predominantly {111} facets and some {100} facets. They share the epitaxy relationship with ZnO as ZnO (0001) [11-20]//Pd (111) [110]. The lattice mismatch between ZnO (0001) and Pd (111) is calculated to be 9%. The mismatch can be reduced by introducing interfacial dislocations and explained by the domain matching epitaxy mechanism [34].

the formation of PdZn nanoparticle on 2wt%PdZnO can be observed from the atomic resolution HAADF image in Figure 5.3b, obtained after 5%H_2/He reduction at 400°C for 2hrs. It is worthy to mention that the PdZn alloy nanoparticles epitaxially grew into ZnO NWs, which may allow these particles to be anchored by ZnO substrate and resistant to sintering even at higher temperature according to our previous work [34]. The bright dots represent columns of Pd atoms and the grey dots represent columns of Zn atoms. The dominant exposed facets of PdZn is {100} and {110}, as shown in Figure 5.3b. The epitaxy relationship between the PdZn alloy nanoparticles and the ZnO NWs is PdZn[001] (100)//ZnO[11-20](0001). The epitaxial growth of PdZn alloy in our work can be attributed to two factors: alkali effects when prepare the catalyst and hydrogen reduction at high temperature (400℃). The addition of Na_2CO_3 when prepare the catalyst with high loading of Pd is designed to both maintain the morphology of ZnO NWs at a moderate PH value and to ensure the epitaxial growth of Pd NPs. The epitaxial growth of Pd particles will effectively make them resistant to the sintering when further reduced in hydrogen, which will favor the conversion rate of methonal in the MSR. The formation of PdZn alloy under reducing environment is well-studied [175, 176]. For the catalyst reduced in hydrogen at room temperature, metallic palladium is discerned. With the increase in the reduction temperature, the ratio of metallic palladium decrease gradually and fully transform to PdZn alloys upon reduction at 623 K [175]. It was found that amount of metallic Zn produced by the reduction of ZnO is in close agreement with that of Pd loaded. Hence it is highly probable that the spillover of H adatoms on Pd to the surface of ZnO is readily quenched once metallic Pd is completely converted to PdZn. Thus, all the Pd loaded is selectively transformed to Pd–Zn alloy. Such isolation

of surface sites through alloying changes the electronic and geometric structure of the active sites, which will greatly enhance the CO_2 selectivity of PdZnO catalysts.

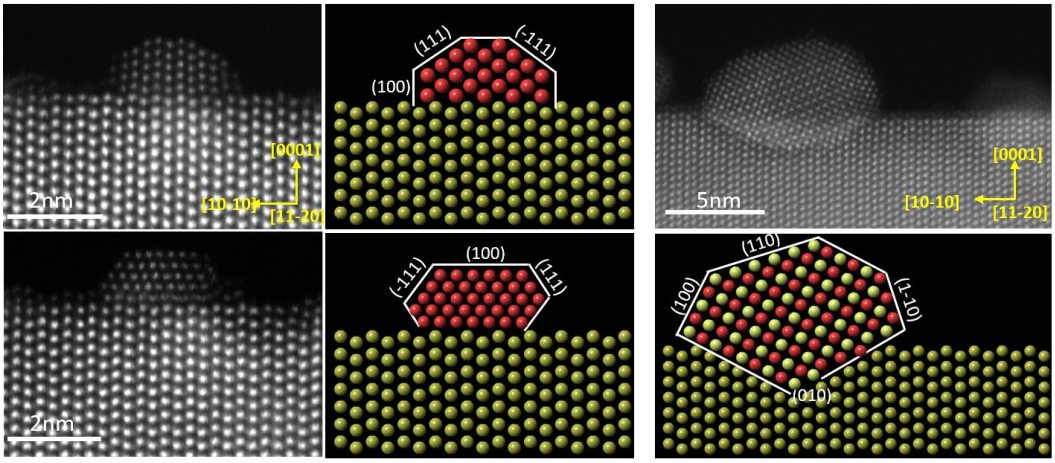

Figure 5.3 Atomic resolved HAADF images of metallic Pd particles and PdZn particles clearly show that the particles are highly faceted and were grown epitaxially on ZnO . Schematics based on experimental data show the exposed facets and the epitaxy relasionship: ZnO (0001) [11-20]//Pd (111) [110] and PdZn[001] (100)//ZnO[11-20](0001).

5.1.3.2 Which one is the best catalyst?

In our work, Pd/ZnO catalysts with different Pd loadings were tested in MSR reaction to investigate the catalytic performace of ZnO supported Pd single atoms, metallic Pd particles and PdZn alloy. For heterogeneous catalysis, it is known that the size of metal particles is quite an important factor that dictate the performance of a catalyst, and the surface atoms of the catalyst play a critical role [177]. The unique of surface atoms come from their unsaturated coordination environment, which make them have higher activity. Recent theoretical and experimental results demonstrated that sub-nanometer clusters have better catalytic activity and/or selectivity than nanometer-sized particles [178-180]. Research on single-atom catalysts (SACs) has been further promoted based on

the understanding of sample preparation and strong metal-support interactions (SMSIs) [31, 181, 182]. But to the best of our knowledge, there hasn't been any systemic study on the ZnO supported Pd catalysts for MSR yet, from single Pd atoms to PdZn alloy NPs. The conversion of methanol over 0.05wt%PdZnO and were tested with the increased temperature as shown in Figure 5.4. Compared with pure ZnO NWs, which works as a reference, 0.05wt%PdZnO shows a pretty high activity. Catalysts with higher loadings of 0.1wt%~2wt% were also tested and normalized to compare the catalytic activity. At 300°C, 0.05wt%Pd/ZnO sample gave a specific reaction rate of 0.212 $mol_{CH3OH}\, h^{-1}\, g_{pd}^{-1}$, which is almost double that of 0.5wt%Pd/ZnO and quadruple that of 2wt%PdZnO catalyst. Thus, our single-atom Pd catalyst was the most active one for the MSR reaction. Later work shows that it is also quite active for CO oxidation, which will be discussed in section 5.2. Several cycles were repeated and not much difference can be observed, which also indicate the good performance in stability of such single-atoms supported catalysts. We believe that such stability is attributed to the SMSIs, which could anchor individual atoms tightly through direct supported metal atom and the metal cation of the support.

the CO selectivity is quite an important factor to evaluate the performance of catalysts for MSR. Previously reports have been given that the CO2 selectivity depends only on the presence of PdZn alloy, whereas the crystallite size of PdZn alloy affects the methanol conversion [183]. Over the catalysts having an PdZn alloy phase which formed among reduction over 300°C, the reactions proceeded selectively to produce CO2, whereas over the catalysts having a metallic Pd phase, methanol was decomposed to carbon monoxide and hydrogen predominantly [175]. Figure 5.5 shows the results by comparing the CO selectivity as a function of Pd loading amount.

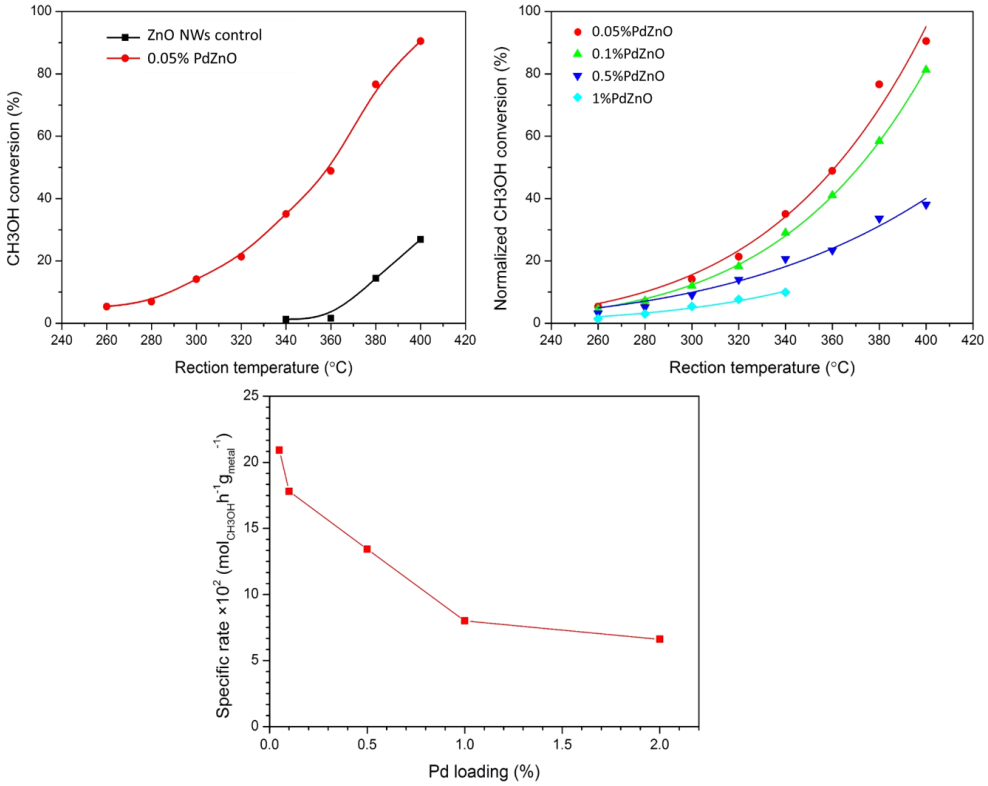

Figure 5.4 Methanol conversion of PdZnO catalysts with different Pd loadings. 0.05wt%PdZnO is shown highly active compared with ZnO control sample (a). Normalized conversion and specific rate show that o.o5wt% PdZnO is the most active one and the conversion per gram of catalyst decrease with the increase of Pd loading.

Typically, there are three types of Pd species dispersion on ZnO nanofacets as shown in the schematics (Figure 5.5): single Pd atoms supported ZnO catalyst (0.05wt%) nominated as Pd_1-ZnO, metallic Pd NPs (0.5wt%) supported ZnO catalyst nominated as Pd-ZnO and PdZn alloy supported ZnO catalyst (over 1wt%) nominated as PdZn-ZnO. The highest CO selectivity occurs on the Pd-ZnO catalyst, and that CO selectivity decreases with an increase in the Pd loading. This is not surprising because methanol dehydrogenation was significant on the metallic Pd particles[184], which was observed to be uniformly dispersed in Pd-ZnO catalyst as shown in Figure 5.2 and Figure 5.3.

It was reported that almost 41% of the adsorbed methanol dehydrogenates and results in the yield of CO [184]. Catalyst with higher Pd loading and reduced (PdZn-ZnO) typically gives larger PdZn particle size, which should exhibit a lower CO selectivity in MSR [174]. Differ from metallic Pd NPs, the energy barrier for methanol dehydrogenation on PdZn surface is much higher and and methanol desorption dominated over dehydrogenation, thus no significant amounts of CO desorption can be found [185].

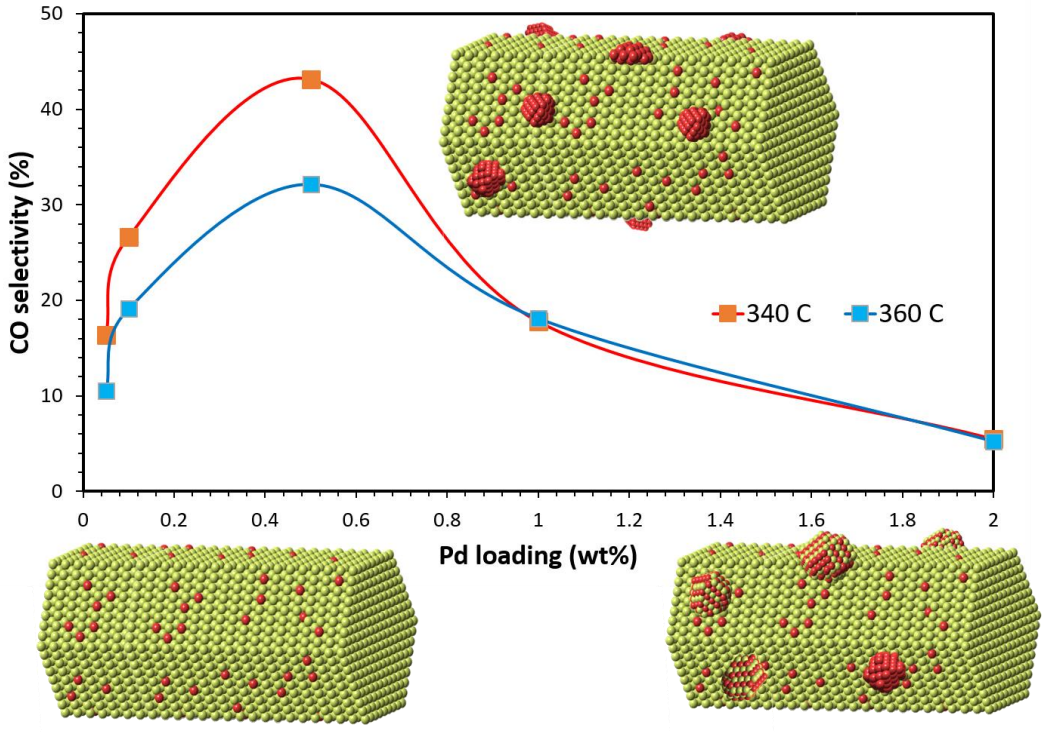

Figure 5.5 CO selectivity increases with the increase of Pd loading at first and then drop rapidly from 0.5wt% of Pd. The model of single Pd atoms supported ZnO, metallic Pd NPs supported ZnO and PdZn NPs supported ZnO were shown in the schematics. Each model has a unique metal-support interaction and determines the difference in CO selectivity.

Intrigued by the excellent activity of Pd1-ZnO, we studied, for the first time, the CO selectivity of single Pd atoms supported ZnO catalysts. Surprisingly, CO selectivity decrease when decrease the loading of Pd (below 0.5wt%) to 10% at 360°C. For the

0.1wt%PdZnO sample, as shown in Figure 5.1b, few Pd species on the sub-nanometer scale are isolated atoms sitting on the support close to each other, which may not have the Pd-Pd bonding. However, there are also several larger clusters, which may have metallic Pd bonding and contribute to the higher CO selectivity compared with Pd_1ZnO catalyst with Pd atoms totally single dispersed. Schwab proposed that a synergetic promotion refers to the energetic interaction between the support and the active metallic component, resulting in the formation of a new type of active entity [186, 187]. The catalytic performance of such SAC may not only cause by the active Pd atoms, but also attributed by the Pd atoms modified ZnO support influenced via the electronic transfer.

5.1.3.3 Influence of preparation conditions and pre-treatment on Pd/ZnO catalysts

the size of metal particles is one of the most important factors that dictate the performance of a catalyst. A series samples with a loading of 1wt% were prepared with different PH value and reduction temperature. Methanol conversion and CO selectivity as a function of temperature is shown in Figure 5.6a-b. It is obviously that the activity of these samples are comparable but with quite different CO selectivity. Based on our results, higher PH value of the solution when prepare catalysts and higher reduction temperature both give larger supported particles. But based on our observation, we found that still a lot of single Pd atoms were dispersed on 1wt%PdZnO catalyst, which dominated the activity. But the existence of metallic Pd may greatly increase the CO selectivity. Since the CO selectivity may be directly related to the formation of surface PdZn layers both in the reduction and in the process of MSR reaction. In the reduction process, hydrogen dissociates to atomic hydrogen on metallic Pd and spill over to initiate the reduction of ZnO and form PdZn alloy. Even at the reduction temperature below 300°C, the temperature at which PdZn alloy forms, ZnO adjacent to metallic

palladium can be partially reduced by the hydrogen produced in the MSR reaction to form PdZn surface layers. Higher PH value and higher reduction temperature will decrease the ratio of metallic Pd NPs and give a lower CO selectivity. Since the ZnO reduction extent in the spent catalyst is much less than that in the catalyst pre-reduced in hydrogen, the pre-reduced PdZnO catalyst has the lowest CO selectivity.

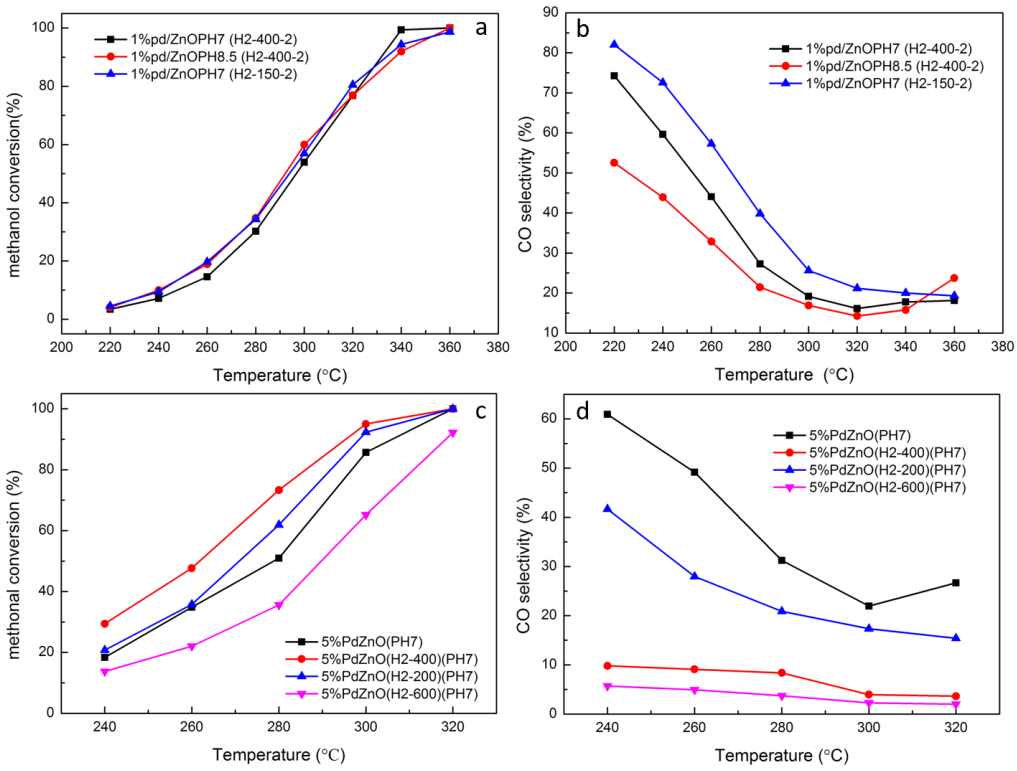

Figure 5.6 the influence of PH value and reduction temperature on the catalytic performances. The change of activity of the catalyst is not only influenced by such conditions but also on Pd loadings (a,c). Higher PH value and higher reduction temperature make larger metal particles , leading to the decrease the CO selectivity (b,d).

to fully understand the influence of reduction temperature on both activity and CO selectivity, 5wt%PdZnO, in which the ratio of single Pd atoms is much smaller and the activity is dominated by Pd NPs, were chosen to do a pre-treatment in hydrogen at room temperature, 200°C, 400°C and 600°C respectively.

As shown in Figure 5.6c-d, CO selectivity decreases with the increase of reduction temperature, which is the same with 1wt%PdZnO catalyst. The activity of 5wt%PdZnO catalyst increased with the reduction temperature below 400°C, but decreased rapidly when reduced at 600°C. Such decrease in activity may cause either by the sintering of PdZn NPs or by the re-deposition of ZnO on PdZn.

to summarize, a series PdZnO catalysts with different loadings were prepared and the catalytic performance were studied. the CO selectivity increases first and drop very quickly with the decrease of Pd loading, strongly dependent on the size of Pd particles. By comparing the performance of these catalysts, single atom Pd supported ZnO catalyst was proved to has best activity and relatively low CO selectivity. Such work may greatly reduce the cost and help improve the performance of PdZnO catalyst for other reactions.

5.2 ZnO supported Ag NPs

Three-Zone high temperature tube furnace was initially used to grow Ag NPs supported ZnO NWs. As the vapor pressure of Ag is higher than Zn, the temperature of the zone used to evaporate Ag need to be over 1100°C. The obtained Ag particle is very large (over 10nm) and with low density. The reason is that when produced ZnO NWs flying through the Ag zone, they instantly have the same temperature, Ag atoms that firstly deposited on the surface of ZnO NWs sinter very quickly at the surface because of they have higher mobility at higher temperature. With the increase need to cut the cost of precious metal supported catalyst and improve the overall efficiency, we were trying to downsize the deposited Ag NPs to smaller size and even 2-D clusters and single atoms. To achieve this goal, a newly designed method with an extra heater was used to control

the temperature of ZnO surfaces when Ag atoms were evaporated and condensed onto it (experimental set up described in chapter 2.1b).

with this method, now we successfully control the size and distribution of the supported Ag species. HAADF images of small Ag NPs, clusters and single atoms supported ZnO NWs are shown in Figure 5.7. Initial test of the catalytic performance over the Ag/ZnO catalyst (Figure 5.7a) for Methanol Steam Reforming (MSR) show that the prepared Ag NPs/ZnO is has activity but very low compared with bare ZnO NWs (Figure 5.8). In order to get uniformly dispersed Ag single atoms and clusters on ZnO NWs, the flow rate that carries ZnO NWs out need to be extremely low, resulted in very low yield of Ag/ZnO single atom and can't be tested for catalytic reactions.

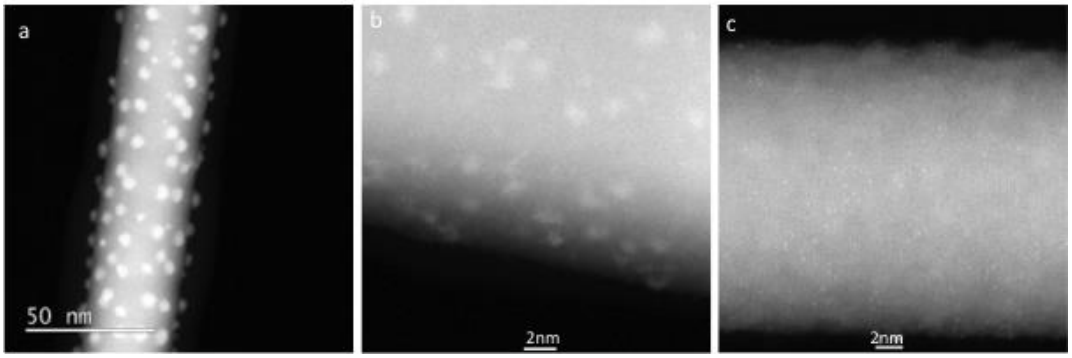

Figure 5.7 Ag NPs, clusters and single atoms were decorated on the surface of ZnO NWs.

ZnO supported Ag clusters catalyst with similar Ag loading was also prepared by modified adsorption (wet chemistry) as comparison (collaborated with Jiaxin Liu).

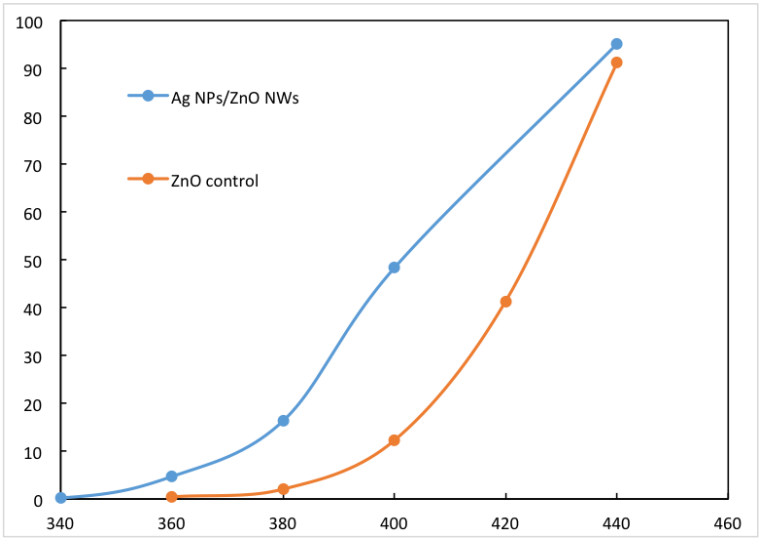

Figure 5.8 AgNPs/ZnO NWs is active compared with bare ZnO NWs for MSR.

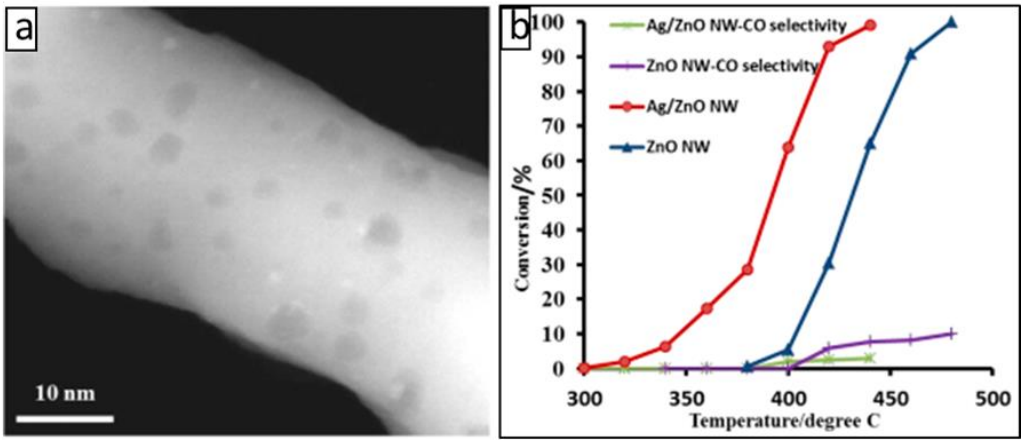

Figure 5.9 (a) HAADF images of a Ag/ZnO NW, revealing small Ag clusters etch pits on the ZnO NW surfaces. Methanol conversion as a function of reaction temperature on the Ag/ZnO-NW catalyst for MSR reaction the bare ZnO NWs were tested as a control.

Figure 5.9a displays a low magnification HAADF image of a representative Ag/ZnO NW, revealing small clusters of Ag on the ZnO NW. It is interesting to note that some etch pits (dark patches), often associated with the small Ag clusters, can be clearly seen on the surfaces of the ZnO NWs. The performance of the Ag/ZnO NW catalyst was

evaluated at different temperatures (Figure 5.9b). Pure ZnO NWs, also a catalyst for the MSR reaction, was tested as a control. It should be noted that the Ag/ZnO NW catalyst has a much higher activity and better selectivity toward CO_2 than ZnO NWs.

5.3 ZnO supported Cu NPs and Cu NWs

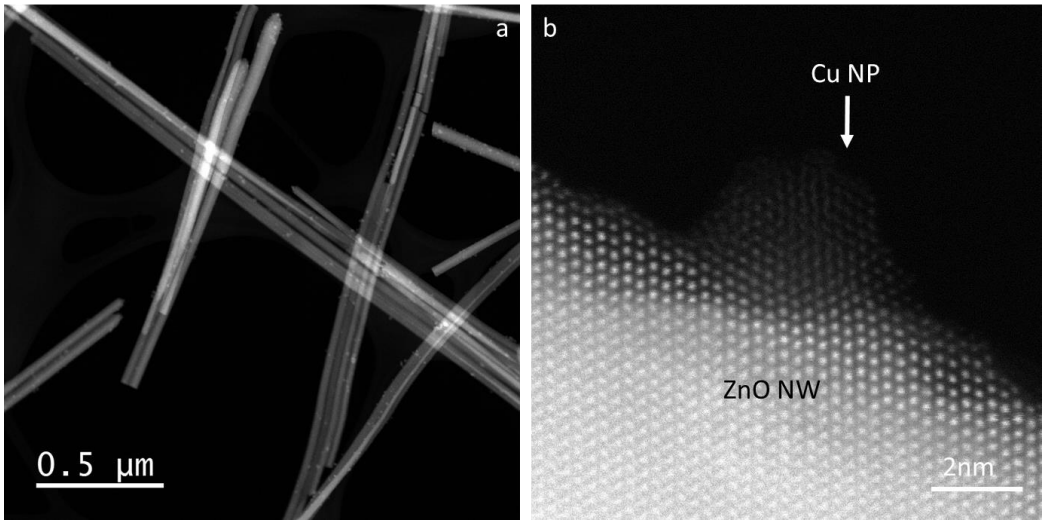

Figure 5.10 Low (a) and high (b) magnification of 5%Cu(P)ZnO NWs. The Cu NP, marked by white arrow, grew epitaxially on ZnO (10-10) facet.

Cu/ZnO has been always being the industry-favored catalyst for methanol steam reforming, but it suffers from the severe sintering in elevated temperature and deactivation. By grow uniform and ultrathin Cu NWs, we could prepare Cu/ZnO NWs resistant to sinter. Two samples, 5%Cu NWs mixed with ZnO nominated as 5%Cu (N) ZnO and 5% prepared Cu nanoparticles grown on surface of ZnO NWs nominated as 5%Cu (P) ZnO were prepared. As the Cu NWs has similar diameter and shapes to ZnO NWs, we didn't figure out how to differentiate these two by taking HAADF images. Figure 5.10 show the low and high HAADF images of 5%Cu(P)ZnO NWs. It is clearly that the Cu NPs grow epitaxially and disperse well on ZnO nanowires. As the epitaxy

relationship can effectively anchor the Cu NPs in elevated temperature, we expect the Cu(P)ZnO catalyst will be stale in MSR reactions.

the initial stability performances were conducted for MSR. Both samples were tested with a temperature program from 240°C to 420°C (cycle 1) and remained at 420°C for 800min. Then the samples were cool down to room temperature and redo the test (cycle 2). From the catalytic activity performances shown in Figure 5.12a, 2nd run of 5%Cu(N)ZnO has higher activity compared with 1st run, whereas the activity of 5%Cu(P)ZnO doesn't change much after long time test. The change of methanol conversion with in 800min for both samples is shown in Figure 5.11. The initial increase may be caused by the continued reduction of CuZnO samples, no deactivation was observed on these catalysts.

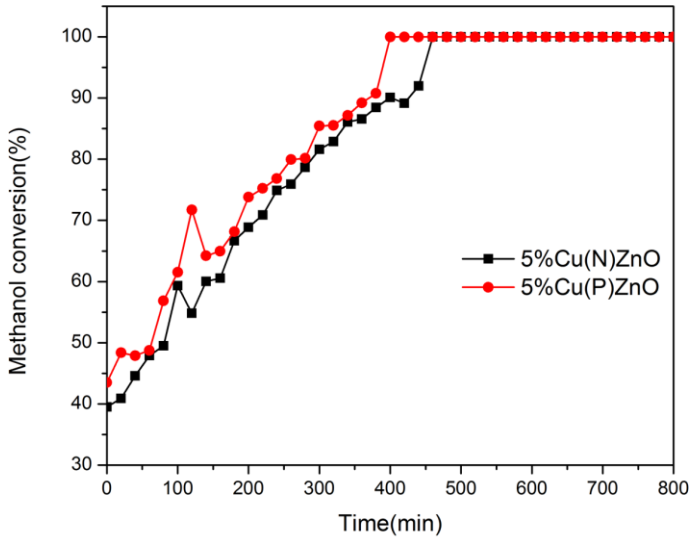

Figure 5.11 Stability test of 5%Cu(N)ZnO and 5%(P)ZnO catalyst for 800min. The methanol conversion of both samples increases as time and finally saturated.

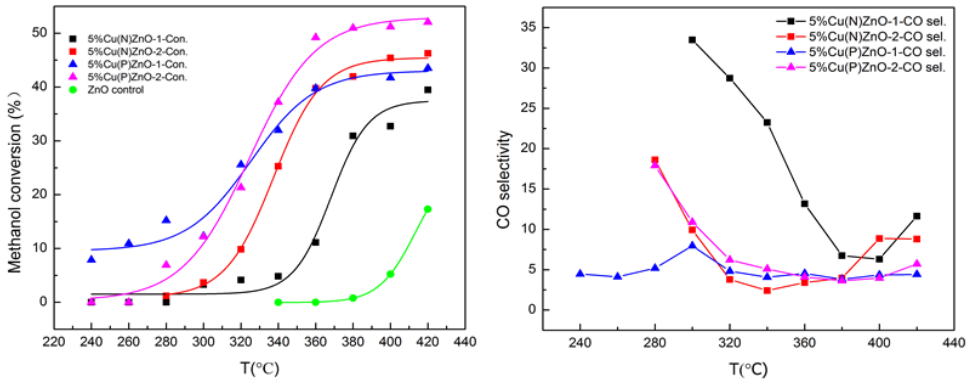

Figure 5.12 Catalytic performances of prepared 5%Cu(N)ZnO and 5%Cu(P)ZnO are tested. After long time (20h) reaction, 5%Cu(N)ZnO is getting better compared with the 1st run, indicate that the stability of such catalyst is quite good.

Combine the catalytic results from Figure 5.12 and Figure 5.11, we can get a conclusion that the epitaxy growth of Cu NPs on ZnO NWs make the catalyst sintering resistant at high temperature and the physical mixture of ZnO NWs and Cu NWs also active and stale. The reason why Cu(N)ZnO catalyst is getting better after long time run may be attributed to the enhanced interaction between Cu NWs and ZnO NWs.

Chapter 6 Catalytic reactions for ZnO NWs supported metal single atoms catalysts

6.1 Catalytic Behavior of ZnO NWs supported Pd_1 Single-atom Catalysts

6.1.1 Introduction

Single-atom catalysts (SACs) have proved to be active for many catalytic reactions and are proposed to significantly increase atom efficiency which is important for sustainability and lowering the cost of manufactured goods [106, 177, 188-194]. More importantly, SACs may possess unique catalytic properties that their nanoparticle (NP) counterparts do not have[105]. The superior catalytic performances of selected SACs can be attributed to the synergistic effect between the highly dispersed metal atoms and the surface properties of the supports. For example, single Pt atoms (Pt_1) dispersed onto FeO_x nanocrystallites showed excellent activity and stability for both CO oxidation and PROX [192].

It has been proposed that the metal (Pt_1)-support interaction weakens the adsorption strength of a CO molecule on the Pt_1, facilitates the generation of oxygen vacancies on the FeO_x surfaces, and subsequently reduces the activation barriers for CO oxidation [192]. Discuss unique features of SAC that explains the above applications.

We have previously reported the catalytic behavior of Pt_1 and Au_1, anchored onto ZnO {10-10} surfaces, for methanol steam reforming (MSR) reaction [106]. Both the activity and selectivity of MSR over the Pt_1/ZnO and Au_1/ZnO SACs were found to be different, primarily due to the intrinsic differences of the different elements and the different degrees of metal-support interactions [195]. Atomically dispersed Pd atoms have

demonstrated high activity for CO oxidation at low temperatures [195]. ZnO supported Pd atoms were recently reported to exhibit excellent catalytic performance for chemo-selective hydrogenation of acetylene [196]. Pd atoms supported on metal oxides [194, 195], carbon [197] and metal particles [198] exhibited high catalytic activity for hydrogenation reactions.

ZnO supported Pd catalysts are of interest because of their potential applications for hydrogen production via the MSR process. Onboard reforming of methanol has been suggested as an alternative route to produce H_2 for polymer electrolyte membrane fuel cells (PEMFCs)[42, 44]. Previous experiments have showed that for MSR reaction ZnO supported Pd NPs, after appropriate reduction treatment; yield high conversion rate and selectivity towards CO_2 whereas when other types of supports are used, decomposition of methanol to CO dominates [199-201]. The superior CO_2 selectivity of the Pd/ZnO system is attributed to the formation of the intermetallic compound PdZn [97], which possesses a similar valence density of states to that of Cu [202]. The strong metal support interactions (SMSI) of the Pd/ZnO system has been investigated for MSR[97]and methanol synthesis [203]. The Pd/ZnO catalysts have been reported to exhibit high activity and selectivity, via the formation of PdZn alloy NPs, for methanol synthesis through hydrogenation of CO_2 under high, or even atmospheric, pressures [204, 205]. The Pd/ZnO system has also been tested for reverse water-gas-shift (RWGS) reaction and the preferential oxidation of CO in the presence of hydrogen-rich gas environment (PROX)[193, 206]. The CO adsorption and oxidation processes depend on the alloying of Pd with Zn as well [207].

to explore the potential applications of supported metal SACs we dispersed Pd single atoms onto ZnO nanowires (NWs) and evaluated the catalytic performance of the synthesized Pd_1/ZnO SACs for a few selected catalytic reactions (MSR, PROX, WGS,

CO and H_2 oxidation, and hydrogenation of CO and CO_2). The reason for using ZnO NWs as support is that the ZnO NWs consist primarily of flat and clean {10-10) nanoscale facets. It is expected that use of well-defined support surfaces facilitates understanding of the structure-property relationships.

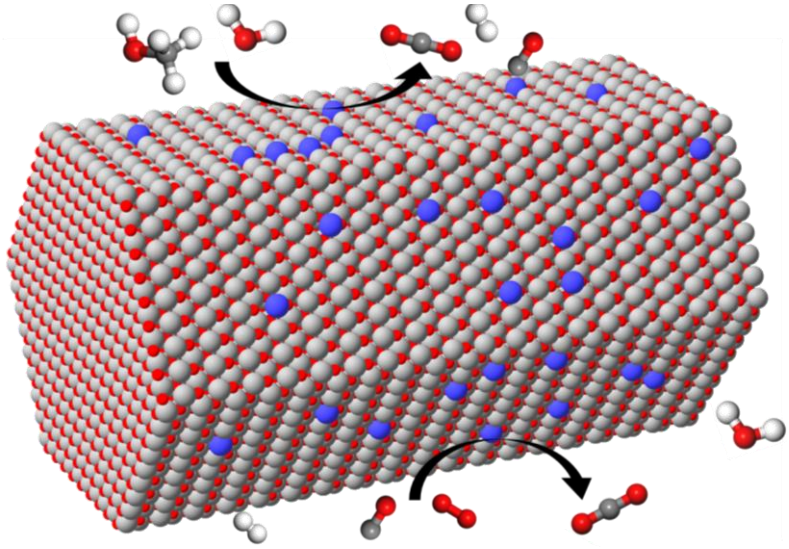

Figure 6.1 Schematic of Pd_1ZnO for different catalytic reactions

6.1.2 Experimental

6.1.2.1 Catalyst preparation

the ZnO NWs were synthesized by a one-step, non-catalytic, and template-free physical vapor deposition process. Briefly, mixed ZnO and carbon powders, in a 1:1 ZnO/C weight ratio, were heated to about 1100°C in a high temperature tube furnace. ZnO NWs, formed in the high temperature zone, were carried, by the carrier gas such as Ar or N_2, to the low temperature zone and were collected for use as catalyst supports the ZnO NWs have a BET surface area of about 16-20 m^2/g with diameters ranging from 20 to 100 nm and lengths of tens of micrometers.

the Pd_1/ZnO NW SACs were synthesized by a strong adsorption method. Typically, the preformed ZnO NWs were dispersed into deionized water under stirring. Calculated amount of aqueous solution of $Pd(NO_3)_2$ was then added dropwise to the ZnO NW suspension under rigorous stirring. After continuously stirring and aging for 2 hrs, the suspension was filtered and washed with deionized water for several times to remove the residual. The resultant solid precipitate was then dried at 60 °C for 12hrs without any further treatment. The nominal Pd loadings for these experiments were 0.05 wt%. The use of low levels of Pd loading assures the successful dispersion of Pd single atoms onto the ZnO NWs without the formation of any Pd clusters or particles.

6.1.2.2 Characterization

the general structure and surface morphology of the prepared Pd_1/ZnO NW SACs were characterized by SEM (JEOL JXA-8350F). Aberration-corrected scanning transmission electron microscopy (AC-STEM), with a nominal image resolution of 0.08 nm in the high-angle annular dark-field imaging mode, was employed to characterize the dispersion of the Pd species. Prior to microscopy examination, the catalyst powders were ultrasonically dispersed in ethanol and then a drop of the solution containing the Pd_1/ZnO NWs was put onto a lacey carbon coated TEM copper grid. Our previous work on SACs and supported metal catalysts have unambiguously demonstrated that atomically dispersed supported metal catalysts can be reliably and fully characterized by the integrated electron microscopy approach [105, 106, 192].

6.1.2.3 Catalytic performance test

the MSR reaction was carried out in a fixed-bed reactor with 100 mg of catalyst. The CH_3OH and deionized water were premixed and pumped to a helium (He) carrier gas and vaporized at 160°C. The final feed gas composition was 8 vol% CH_3OH + 12 vol%

H_2O and He balance. The total gas flow rate was 37 ml/min, providing a gas hourly space velocity (GHSV) of 44,400 $ml \cdot h^{-1}g^{-1}cat$. The reaction products were on-line analyzed by a gas chromatograph (Agilent 7890A, HS-D 100/120 column and thermal conductivity detector). The products consisted of only H_2, CO and CO_2, and no other products were detected. The conversion rate of the MSR reaction was calculated based on the carbon balance.

the WGS tests were conducted in a fixed-bed reactor with 50 mg of catalysts and the reaction feed gas composed of 2vol%CO/10vol%H_2O (0.18 ml/h in liquid) balanced with helium (37 ml/min). The GHSV was 44,400 $ml \cdot h^{-1}g^{-1}cat$. The reaction feed was preheated to 160°C to maintain the vapor H_2O. For the RWGS reaction, the feed gas consisted of 5 vol% H_2/ 0.6 vol%CO_2 balanced with helium with a GHSV of 96,000 $ml \cdot h^{-1}g^{-1}cat$. The CO conversion was calculated based on the difference between inlet and outlet CO concentrations.

the catalytic performance of the Pd_1/ZnO SACs for CO and H_2 oxidation, and PROX was evaluated in a fixed bed, plug-flow reactor. Typically, 50mg of the catalyst was loaded in a quartz tube and then the feed gas pass through the reactor at a flow rate of 33ml/min, resulting in a GHSV of 39,600 $ml \cdot h^{-1}g^{-1}cat$. The feed gas composed of 1vol% CO, 1vol% O_2 and balanced with He for CO oxidation; 1vol% H_2, 1vol% O_2 and balanced with He for hydrogen oxidation and 1~40% vol% H_2, 1 vol% CO, 1 vol% O_2 and balance He for PROX. The outlet gas composition was on-line analyzed by a gas chromatograph (HP 7980) equipped with an Agilent SC-ST 800/100 column and a thermal conductivity detector using He as carrier gas. The stability measurements under reaction conditions were performed at 185°C. The H_2 conversion and CO conversion was calculated based on the inlet and outlet H_2 and CO concentrations, respectively.

6.1.3 Results and discussion

6.1.3.1 Characterization of Pd_1/ZnO

Figure 6.2a is the SEM image of prepared Pd_1ZnO NWs. The NWs show their general morphology with an average diameter of ~ 50 nm and length of ~10 micrometers, resulting in a high aspect ratio of about 200. HAADF-STEM imaging was used to characterize the location and dispersion of deposited Pd atoms. It is capable of differentiating heavy elements from light elements because its image intensity is directly related to the atomic number of the probed species [208]. Representative low and high magnification of high-angle annular dark-field (HAADF) images of the Pd_1/ZnO are shown in Figure 6.2b-c, where the ZnO NWs were tilted with the electron beam close to [1010] zone axis of ZnO. After analyses of many low- and high-magnification HAADF images, we concluded that there were no Pd clusters/particles in the Pd_1ZnO catalyst. The brighter dots represent single Pd atoms (indicated by the yellow arrows in Figure 6.2c) located on the Zn columns of the ZnO NWs. These isolated single atoms were relatively stable under electron beam irradiation, suggesting that they were

anchored onto ZnO {1010}.

the catalyst used in MSR and CO oxidation for 15hrs is also examined in STEM. Figure 6.3a and Figure 6.3c is typical low and high magnification HAADF images of Pd_1ZnO catalyst used in MSR, and Figure 6.3b and Figure 6.3d for CO oxidation reaction. Observable small clusters (marked by red arrows in Figure 6.3a) and particles (marked by the green arrows in Figure 6.3b) indicate that the single dispersed Pd atoms aggregate in the process of MSR and CO oxidation reaction. Higher magnification images (Figure 6.3c-d) show that the clusters formed in the MSR reaction is two-dimensional with a size of ~1nm, however, round large particles with an average size

of ~3nm formed in the CO oxidation reaction. We will discuss later that the different morphology and size of the aggregated clusters and particles will greatly influence the catalytic performance of the catalysts.

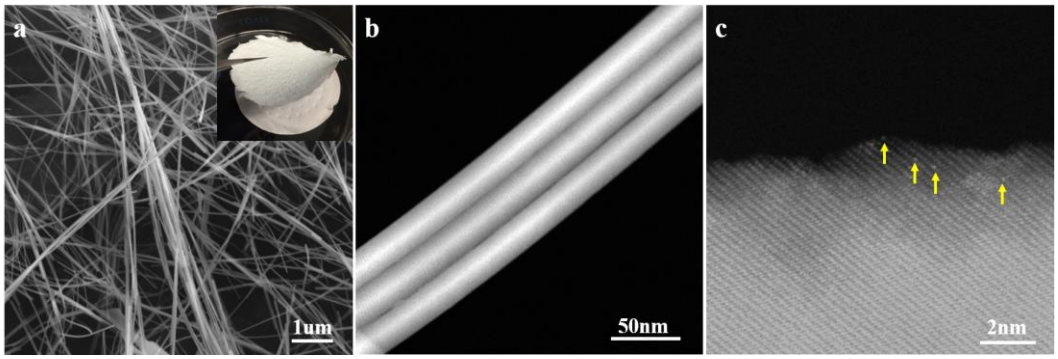

Figure 6.2 a) SEM image of Pd1/ZnO catalyst, shows the high aspect ratio and uniformity of the products. Low (a) and high (b)magnification HAADF images of Pd_1ZnO catalyst, only single atoms(indicated by yellow arrows) but no particles were observed.

6.1.3.2 Catalytic testing of Pd1/ZnO

6.1.3.2.1 Methanol steam reforming, Water gas shift and Reverse water gas shift

Pristine ZnO NWs and Pd_1/ZnO NWs were tested in MSR experiments. Only H_2, CO, CO_2 and H_2O were detected and the conversion is calculated based on the carbon balance. The methanol conversions on Pd_1ZnO NWs and bare ZnO NWs as a function of temperature and the stability of Pd_1ZnO catalyst at 390°C are shown in Figure 6.4a-b, respectively.

Both conversions increase gradually as the temperature increase. However, the Pd_1ZnO catalyst is much more active than pristine ZnO NWs. For instance, methanol conversion on Pd_1ZnO reaches 73% at 380°C and 100% at 400°C while at the same temperature, only 15% and 27% of corresponding methanol conversion on pristine ZnO NWs. We previously reported that the calculated TOF at 380 °C for pure ZnO NWs is 1.8×10^{-2}

s^{-1} [106]. For the Pd_1/ZnO, the corresponding TOF for MSR were estimated to be $3.2s^{-1}$, about two orders of magnitude higher than that of ZnO support.

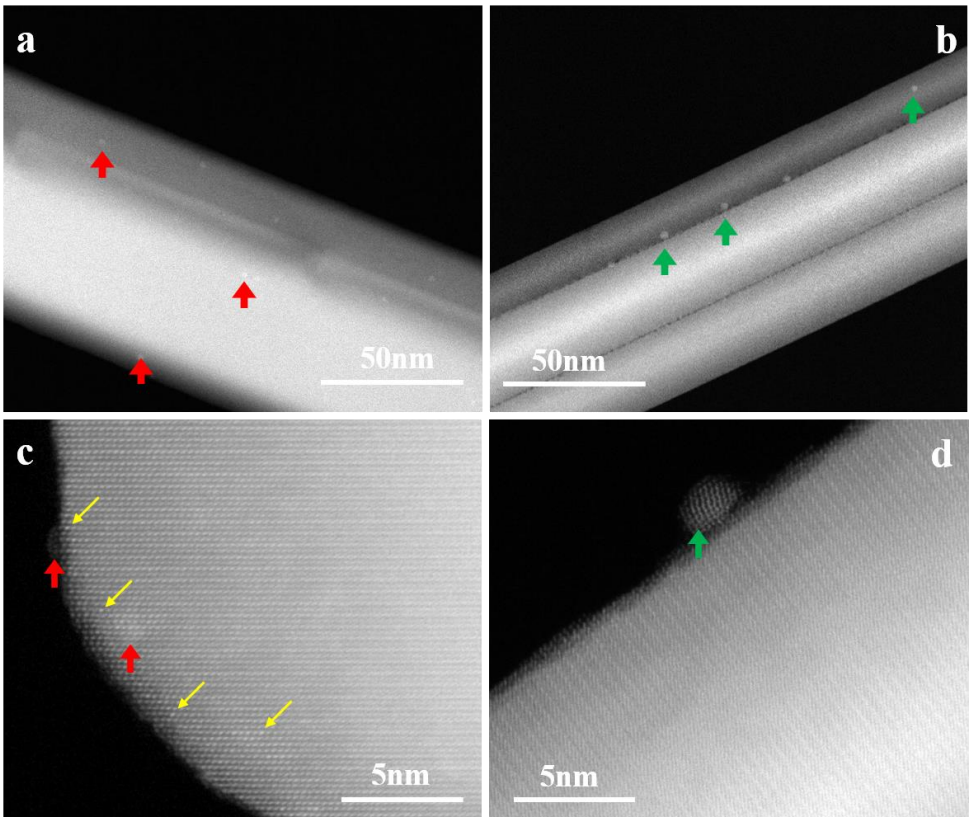

Figure 6.3 Low (a,b) and high(c, d) magnification HAADF images of Pd_1ZnO after long time MSR(a,c) and CO(b,d) reactions. At low magnification (a,b) images, small particles can be observed in both of the catalyst with a particle size of 1-2nm(a) and 2-3nm(b),respectively. High magnification images shows that the Pd atoms form two dimensional clusters (indicated by red arrows in c) after MSR reaction but 3-dimensional particles (indicated by green arrow in d) after CO oxidation reaction.

On ZnO NWs, the selectivity toward CO is very low, which is about 3% and independent with temperature. The CO selectivity on Pd_1ZnO at 1st cycle at 260°C is relatively high (25%), but it decrease rapidly with temperature and reaches low CO selectivity as pristine ZnO NWs over 340°C. Typically Pd metal particles on ZnO is very much selective to methanol decomposition ($CH_3OH \rightarrow CO+H_2$) and yield CO[97, 176], while PdZn alloy that forms during calcination and reduction processes enhances the

selectivity MSR towards CO_2 production[209]. Our result shows that Pd single atoms, similar to PdZn,, have very good CO_2 selectivity (over 97%) after 380°C. the catalyst was quite stable at 360°C after 800min run, as shown in Figure 6.4b. Low and high magnification HAADF images of used catalysts are shown in Figure 6.3a and Figure 6.3c. Both single atoms (indicated by yellow arrows) and two-dimensional clusters (indicated by red arrows) were observed. The two-dimensional clusters are composed of one or two atomic layer Pd atoms as shown in Figure 6.3c. Since no deactivation of the catalyst was observed, we propose that such two-dimensional clusters also exhibit high activity and low CO selectivity in MSR.

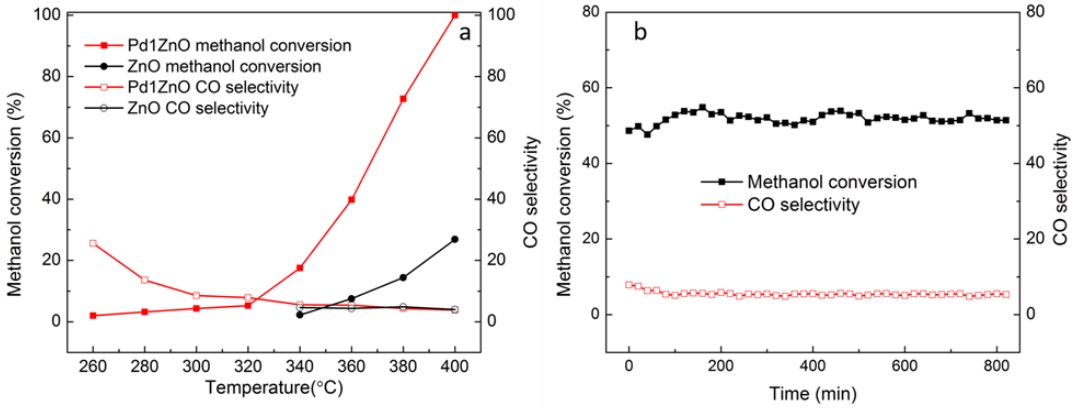

Figure 6.4 Methanol conversion (solid) and CO selectivity (blank) over Pd_1ZnO catalyst in a cycle test (a) and stability test at 360°C (b).

It was reported that the reaction pathways towards CO_2 could be classified into two: one is the association of formaldehyde from methanol with hydroxyl from water and another is decomposition of formaldehyde to CO followed by WGS reaction [210]. We previously reported that on Pt_1/ZnO and Au_1/ZnO, complete dehydrogenation of formaldehyde rather than its association with hydroxyl is favorable [106]. In order to evaluate the process of the pathways on Pd_1ZnO, we performed WGS and RWGS tests on Pd_1ZnO NWs at the temperature range of 260°C -440°C. There is no activity in

WGS reaction, while CO_2 can be partially converted in RWGS reaction, is shown in Figure 6.5. This result shows the inability of Pd_1/ZnO to convert CO to CO_2 below 400°C, which indicates that it has a different pathway with Pt_1 and Au_1 on ZnO[106]. We propose that the catalytic process on Pd_1/ZnO is similar to that on PdZn, which is limited by the dehydrogenation of methoxyl (CH_3O*) and the reaction between formaldehyde and hydroxyl is involved to eventually form CO_2 [195]. Although PdZnO has been reported to be active for the methanol synthesis in the hydrogenation of CO_2 under atmospheric pressure [204], methanol product was not observed in our test.

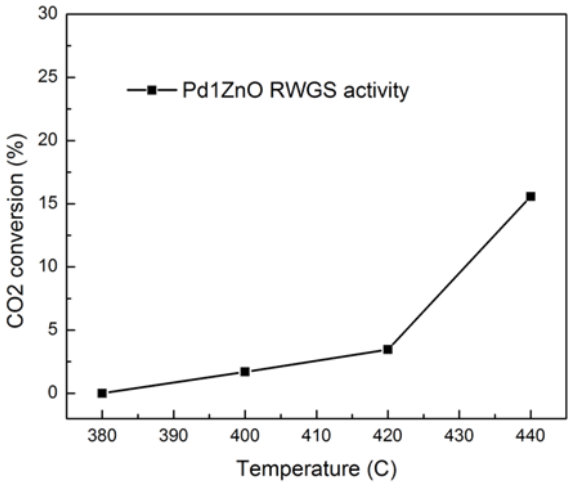

Figure 6.5 CO_2 conversion vs. temperature of Pd_1ZnO catalyst for RWGS reaction.

6.1.3.2.2 CO oxidation

the catalytic performance of Pd_1ZnO in CO oxidation was shown in Figure 6.6. Under reaction conditions, the CO conversion begins at about 140°C and increases gradually with the increasing temperature. A sharp increase of CO conversion can be observed when the temperature close to T100 (100% CO conversion), which is achieved at 196°C. The ZnO NWs support, as a control, was totally inactive with CO conversion in this temperature range. The stability of the Pd_1ZnO catalyst at 185°C is shown in Figure 6.6b. The conversion reaches about 40% at the initial and drops to 30% after

150min, and it becomes lower than 20% after 800min. The deactivation of supported Pd catalyst was reported in other catalysts, such as Pd/grapheme [11] and Pd_1/Al_2O_3 [193]. It was suggested that the Pd^{2+} is being reduced during the reaction and forming metallic Pd, which shows a negative order of reaction with respect to CO [193]. In our catalyst, after 800min run, we observe aggregation of the deposited Pd single atoms into particles with an average size of 3nm (Figure 6.3b and Figure 6.3d), which may be the main reason of the deactivation of the Pd_1ZnO catalyst. From the slope of the Arrhenius plot, as shown in the inset of Figure 6.6a, the apparent activation energy (Ea) can be estimated to be 69.3kJ mol. We previously reported that Pd_1/ZnO has the highest CO oxidation activity compared with other M_1/ZnO catalysts [211] (M=Pt, Rh, Ir). We propose that the CO oxidation should be accomplished in a catalytic cycle, which is initiated by the adsorption of CO onto Pd and then reacts with a lattice oxygen coordinated with Pd. Desorption of CO_2 produced will promptly remove lattice oxygen coordinated with Pd and form new oxygen vacancy. The oxygen molecule absorbed at the vacancy is highly active and react with adsorbed CO.

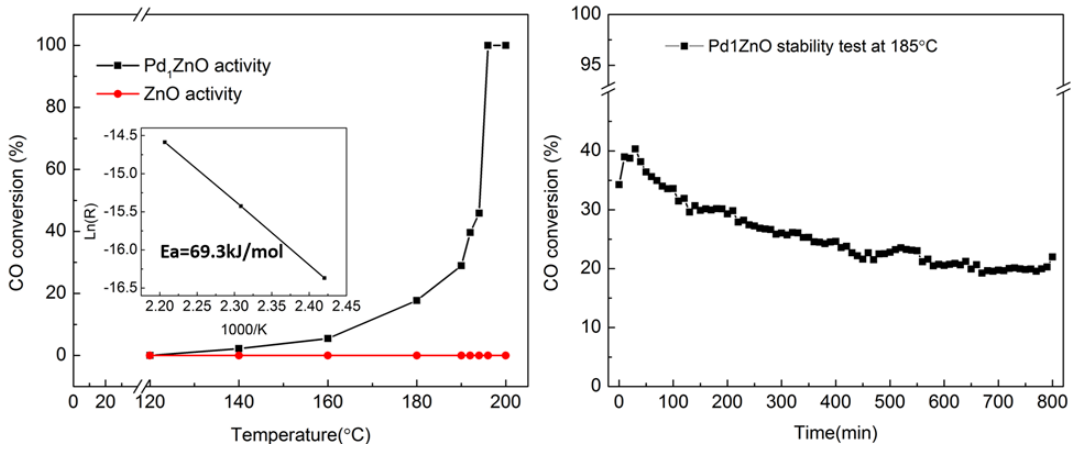

Figure 6.6 CO conversion (a) and stability test at 185°C (b) over Pd_1/ZnO catalyst. Activation energy is 69.3kJ/mol, calculated from the inset Arrhenius plot in (a). The Pd_1ZnO deactivated about 50% after 800 min run at 185°C.

6.1.3.2.3 Hydrogen oxidation

Hydrogen oxidation reaction was performed in 1 vol% H2, 1 vol% O2 and balanced with He. The hydrogen conversion increased with the increasing temperature and

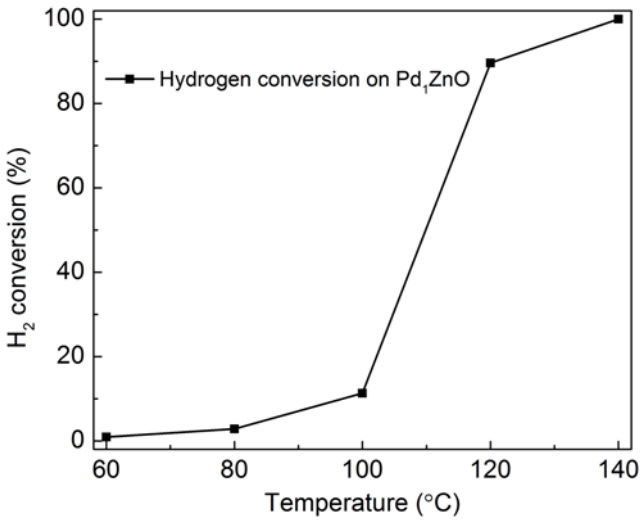

Figure 6.7 Hydrogen conversion on Pd_1ZnO

complete conversion temperature is 140°C, as shown in Figure 6.7. The TOF values are calculated to be 0.03 and 0.93 at 60°C and 120°C, which is 1-2 orders higher than reported Pd/Al_2O_3 [212] and Au_1/CeO_2 catalyst [213]. The experimentally obtained high activity of H_2 oxidation is proposed to be a result of the good capability of supported Pd_1 atoms to activate molucules. Although there has been conclusion that at least two contiguous Pd atoms are required for H_2 activation, density functional theory calculations indicated that Pd monomers may be capable of H_2 activation [214] and Pd monomers on Au (111) surface has been reported to catalyze the dissociative adsorption of H_2 [198].

6.1.3.2.4 Preferential CO oxidation in hydrogen

PROX reaction with 40 vol% H_2, 1 vol% CO and 1vol% O_2 were performed on Pd_1ZnO in the temperature range of 100-200°C. Figure 6.8a shows CO conversion increased gradually with reaction temperature and reached the maximum of 19% at 160°C and then decreased at higher temperatures. Such behavior is caused by the competitive H_2 oxidation with increased temperature and has been observed on supported Au [213] and Pd[206] catalysts. The O_2 conversion on Pd_1ZnO for PROX (Figure 6.8b) is low below 140°C and increases significantly at 160°C and then gradually at higher temperatures. Thus, as the reaction temperature is raised, the CO oxidation is suppressed while the H_2 oxidation is enhanced with the present catalyst and conditions. The reaction was also conducted at different H_2 concentrations for Pd_1ZnO in the range of 180-200°C. CO conversion is lower in the absence of H_2 below 160°C, which indicates that H_2 is needed for the Pd_1ZnO catalyst to be active for the oxidation of CO at low temperature. However, the presence of H_2, even as low as 1vol%, hinders the oxidation of CO when the temperature is higher than 190°C. The O_2 conversion of hydrogen oxidation on Pd_1ZnO achieves ~50%, the highest O_2 conversion value, at 120°C while almost no conversion in the presence of H_2. The CO_2 selectivity is extremely low compared with other reports 37. Such catalytic performance indicates that single Pd atoms have higher H_2 activation ability compared with Pd or PdZn particles.

At low temperature, ranging from 100 to 140°C, the O_2 conversion in hydrogen oxidation is much higher compared with that in PROX, as shown in Figure 6.8b. The only difference between these two reactions is the existence of CO. For instance, the O_2 is totally converted at 100°C when CO is absent while no O_2 conversion at all when CO exists. This result indicates that CO binds to Pd sites and blocks the adsorption and

activation of H_2 at low temperature. Similar results have been reported in bimetallic Pd-Au and Pd-Cu single atom alloys where CO selectivity binds to the single Pd atoms and blocks the Pd entrance/exit sites for H_2 adsorption/desorption [198, 210].

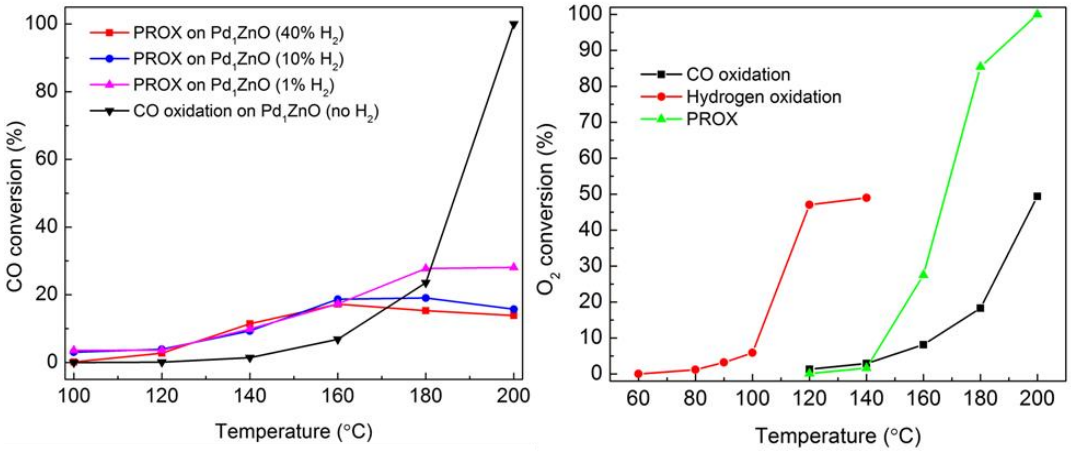

Figure 6.8. (a) CO conversion in PROX and CO oxidation over Pd_1/ZnO with different H_2 concentration. Below 160°C, the existence of hydrogen activate CO oxidation but after 180°C, H_2 hinders the CO conversion to CO_2. (b) O_2 conversion in hydrogen oxidation and PROX over Pd_1ZnO. Below 140°C, CO adsorption on Pd atoms poisons the hydrogen oxidation reaction.

6.1.4 Summary

to summarize, single Pd supported by ZnO NWs were prepared and tested in several typical catalytic reactions and the mechanism of these reactions has been discussed. . The Pd_1ZnO shows good activity and stability at high temperature, most importantly, it also has very high selectivity towards CO_2, makes it a very good catalyst for MSR. The Pd_1/ZnO is active for CO oxidation but it deactivate after long time reaction. In the PROX reaction, CO adsorption is dominant and H_2 can help to activate Pd_1ZnO catalyst in CO oxidation at low temperature. H_2 adsorption is dominant and hinders the CO oxidation at higher temperature.

6.2 ZnO supported M_1 single atom catalysts for CO oxidation

6.2.1 Introduction

CO oxidation in catalytic chemistry is of great importance for both fundamental and practical reasons. The ability of removing toxic CO from environmental exhausts [215] and tracing of CO from H_2-rich fuel cells [216, 217] have stimulated numerous investigations over a variety of catalysts. The simplicity of CO oxidation in turn makes it an ideal reaction model to study the elementary process involved in the reaction. Supported noble metal particles, clusters and recently studied atomically dispersed single atoms have been extensively studied for the CO oxidation [22, 180, 192, 218-223]. For now, we understand that the catalytic performance of supported catalysts is determined by several factors, including their electronic structure, nanostructure, structural flexibility and most importantly, interaction with the support {counting electron}. As the presence of low-coordination sites is thought to be responsible for the enhanced catalytic activity [224], two-dimensional clusters and single atom catalysts (SACs) show its superior overall efficiency [188, 192, 225, 226]. The active centers in SACs consist of isolated individual metal atoms and their immediate neighbor atoms of the support. The strong metal-support interaction result in charge transfer and thus generates new ensembles which may possess unique catalytic properties different from those of the corresponding supported metal NPs. Such interaction will be affected either by the type of single atoms or the metal oxide substrate.

Qiao et al. successfully synthesized single Pt atoms dispersed on a reducible FeO_x support and it shows high activity and stability for CO oxidation [192]. The same group also reported the experimental and theoretical study of Ir_1/FeO_x SACs in CO oxidation [191], demonstrating that Ir_1/FeO_x catalyst has a lower activity for CO oxidation than

Pt_1/FeO_x. Other single metal atoms, including Au, Rh, Pd, Co, Cu, Ru and Ti on FeO_x were theoretically investigated for CO oxidation [223]. They found that oxygen defective Pd_1/FeO_x and Rh_1/FeO_x SACs has higher activity than reported Pt1/FeOx catalyst. Abbet et al. studied CO oxidation on single Pd atom supported on MgO[227]. Experimental performances of Rh_1/ Al_2O_3 [228], Pt_1/ Al_2O_3 [229] and theoretical studies of other Al_2O_3 supported single metal atoms (Pd, Fe, Co and Ni)[230] in CO oxidation were also reported. The supported noble metal catalysts can also promote the participation of oxygen atoms of Al_2O_3 in chemical reactions even though the Al_2O_3 is chemically inert and thermodynamically stable. Pd single atoms anchored on the Al_2O_3 surface and surface oxygen participate in the reaction, showing high catalytic activity and stability toward CO oxidation [195].

In order to better understand how single atoms of different noble metals dispersed on the same support material affect a specific catalytic reaction, we dispersed various single noble metal atoms on ZnO NWs. Our ZnO NWs are mainly clean and flat {10-10} exposed, and the M_1 atoms may occupy the Zn sites, the illustration of the designed catalyst is shown in Figure 6.9. The catalytic performance of various M_1-ZnO (M=Pd, Pt, Rh and Ir) were systemically examined, aiming at the in-depth understanding of the strong metal-support interaction and developing even more efficient and low cost nanocatalysts for CO oxidation.

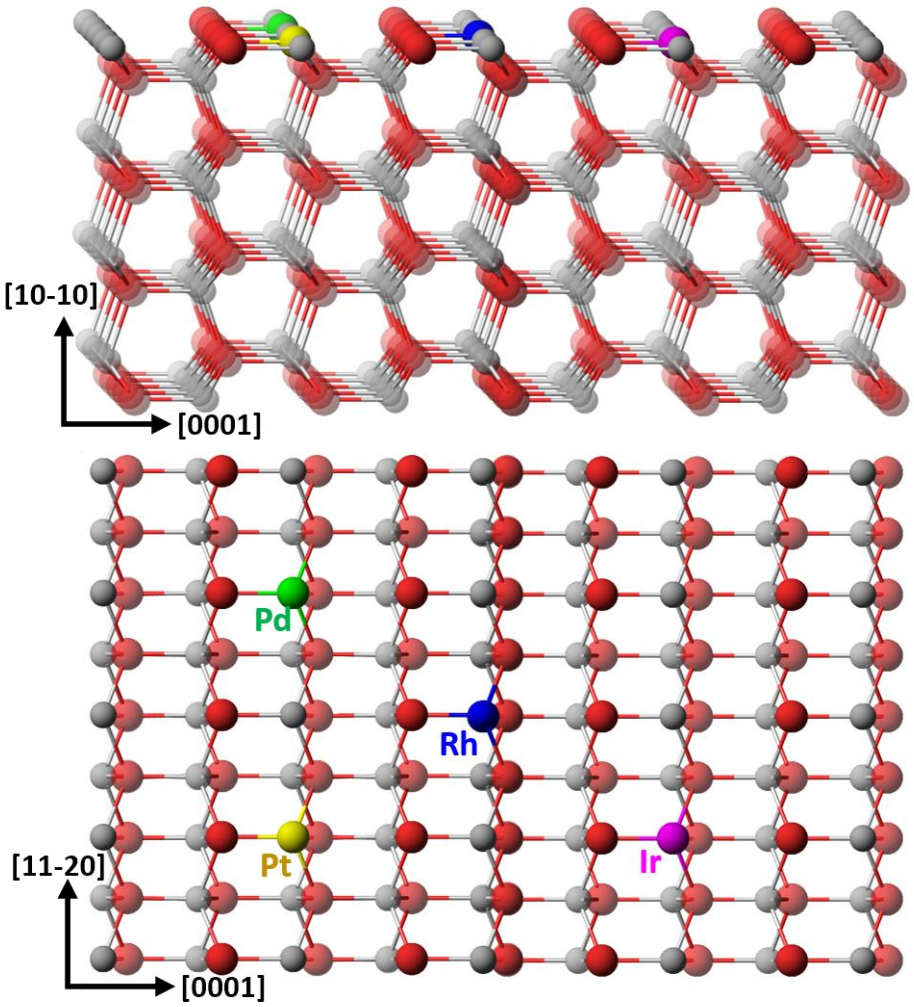

Figure 6.9 Illustrations of M_1/ZnO catalyst. Different types of metal atoms (Pd, Rh, Pt and Ir) were marked with green, blue, yellow and pink, respectively. The M1 atoms grow in the cation position on ZnO{10-10} surface.

6.2.2 Sample preparation and test condition

the SACs were synthesized by a modified adsorption method. Briefly, noble metal precursors were mixed with the pre-formed ZnO NWs. The resultant precipitate was filtered, washed with deionized water and dried in an oven. The nominal loading level of the various noble metals was ~0.05 wt% and the corresponding SAC catalysts were denoted as 0.05Pd/ZnO, 0.05Pt/ZnO, 0.05Rh/ZnO, and 0.05Ir/ZnO, respectively. The CO oxidation reaction was evaluated in a fixed-bed, plug-flow reactor. The feed gas

composition was 1vol% CO + 1vol% O_2 and balance He with a flow rate of 33 ml/min. For all the catalytic tests, 50 mg catalyst was directly used without further treatment. The outlet gas composition was on-line analyzed by a gas chromatograph and the CO conversion was calculated based on the inlet and outlet CO concentrations. Aberration-corrected high-angle annular dark-field STEM (HAADF-STEM), indispensable for investigating the atomic level structures of nanostructured catalysts, was used to examine the synthesized SACs.

6.2.3 Results and discussion

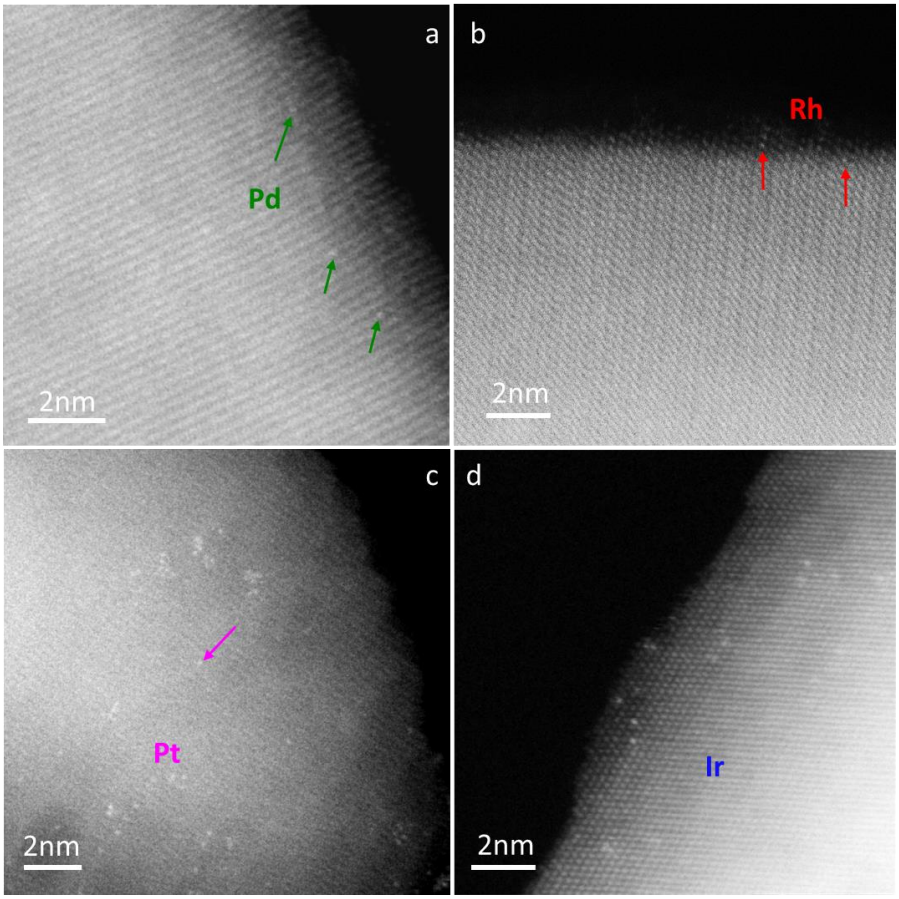

Figure 6.10 HAADF images of M_1ZnO SACs.

HAADF-STEM images of the synthesized SACs were obtained to provide information on the dispersion and distribution of the noble metal atoms on the ZnO NWs. Four representative images are shown in Figure 6.10. The isolated and highly dispersed individual Pd, Rh, Pt and Ir atoms (indicated by the yellow arrows in Figure 6.10.a-d) are clearly revealed. At low levels of noble metal loading the synthesized SACs contained only single noble metal atom. One of the key factors that induce the different performances over M_1-ZnO catalyst is the location and geometric effects of single atoms on supports. For M_1 on ZnO {10-10} surfaces, as shown in our HAADF images, individual metal atoms occupy exactly the positions of the Zn atoms（See Figure 6.11).

Although plan-view HAADF images which represent the projection of atoms along the incident beam direction, induce the difficulty in distinguish the surface atoms from substrate, we successfully confirm that the observed metal atoms were located on the surface of ZnO nanofacets by slightly tilt the electron beam off zone axis (Figure 6.11).

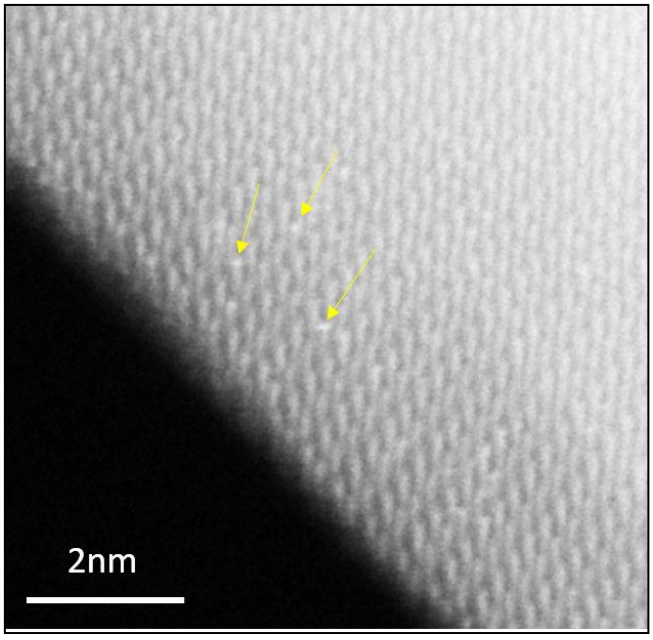

Figure 6.11 HAADF image obtained by slightly tilt electron beam shows the supported metal atoms located on surface of ZnO. Yellow arrows indicate the metal atoms.

Our previous work also gets this conclusion by varying the focus of the electron beam (or 'depth sectioning')[181]. After the examination of many HAADF images, we didn't observe any displace to the bridge sites between Zn and O atoms, which would cause unstable metal atoms positioned on top of the surface Zn sites. Thus, we assume that the metal atoms may anchor either onto the corresponding {10-10} surface Zn vacancy positions or substitute Zn lattice sites. It was reported that the Pt_1 anchor onto surface Zn vacancy positions are more energetically favorable compared with substitute at the substrate Zn lattice site [181].

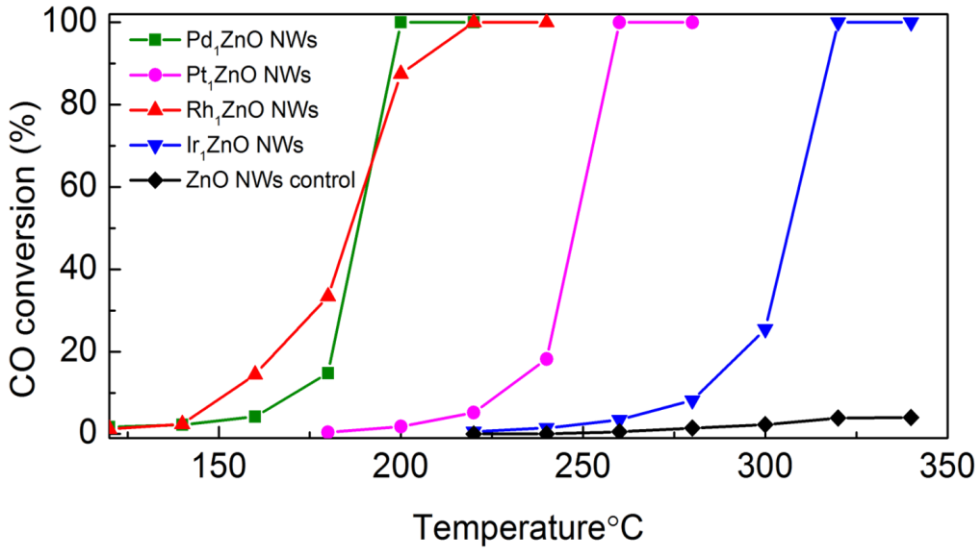

Figure 6.12 CO conversion vs. reaction temperature for various noble metal M_1/ZnO SACs, clearly demonstrating the differences in activity of ZnO NW supported noble metal SACs. The nominal metal loading for all the SACs was 0.05wt%. The condition for the CO oxidation was the same for all the tested noble metal SACs. Among the four SACs tested, the Pd_1/ZnO and Rh_1/ZnO NW has similar activity and much higher than Pt_1ZnO and Ir_1ZnO. All of these catalysts are active compared with bare ZnO NWs.

CO oxidation catalytic reaction is selected to study the catalytic performance of prepared M_1/ SACs. Although the CO oxidation process is facet influenced, our prepared ZnO NWs were predominantly exposed with {10-10} facets, which are quite inactive. The kinetic study of CO oxidation to CO_2 over ZnO showed that there are two

reaction paths: 1) the surface reaction of gaseous CO with O^-, followed by the rapid desorption of CO2 formed; 2) the process is controlled by both the surface reaction of gaseous CO with neutral atomic oxygen species and the desorption of CO2 formed [231]. But there is a rapid build-up of surface carbonate and CO can only bind weakly to Zn^{2+} sites and does not form CO_2 or CO_3[2-231].Thus any differences in catalytic performances between these SACs are directly related to the MSI. Figure 6.12 displays the CO conversion vs. temperature for the as-synthesized SACs. The bare ZnO NWs were also tested as a reference and confirmed to be inactive for CO oxidation. The catalytic test data clearly show that all the fabricated noble metal SACs are active for CO oxidation. Their activities, however, were very different. Among the four noble metals (Rh, Pd, Ir and Pt) the Pd_1/ZnO SAC is most active over 180°C and Rh_1ZnO is most active below 180°C, while the Ir_1/ZnO shows the lowest activity. These test results clearly demonstrate that different noble metal atoms interact differently with the ZnO {10-10} surfaces and hence generate different types of active centers for CO oxidation.

the presence of surface embedded single metal can dramatically change reaction energetics and barriers for the reactant and intermediates involved in CO oxidation. It was reported that Rh_1/FeOx and Pd_1/FeOx exhibit superior catalytic performance for CO oxidation than Pt_1/FeOx [223]. Ir_1/FeOx has also been reported with lower catalytic activity for CO oxidation compared with Pt_1/FeOx [191]. Compared with Pt_1/FeO_x catalyst, the reaction activation barrier on Ir_1/FeO_x for CO oxidation is higher and the adsorption energy for CO molecule is larger. Comparing with other 5d metals, Ir has a higher melting point and surface energy, leading to a good dispersion on the surface and strong interactions of Ir particles with the supports [232]. For unsupported Pt group metals, Pd was reported to has the lowest calculated CO adsorption energy of the most

favorable site on close packed metal surfaces while Ir has the highest[233, 234], indicating that the strong CO adsorption may be the main reason for the lowest activity of Ir_1ZnO catalyst.One of the key points to achieve a high effective catalyst for CO oxidation is to decrease the adsorption strength of CO because the strong CO adsorption and activation of O_2. A weaker adsorption strength of CO at a lower temperature is more favorable. The charge transfer and catalytic properties of different single metal atoms on the same supports, including niobium oxide, silica surfaces [235] and boron nitride nanosheets [222] are also quite different. The differences in activity are mainly caused by the different absorption energy of the reactants on different combination of precious single atoms and substrate. Based on

our results and previous studies, we believe that the interaction between single metal atoms and support is influenced both by the type of M_1 atoms and by the intrinsic nature of the supports.

the electronic structures of elements, which are the basis of adsorption ability, provide deep insight into the interaction between adsorbates and surfaces. Both covalent bonds due to the overlap of orbitals and ionic bonds induced by the charge transfer influence the adsorption between CO molecular and metallic surfaces. Because the outer electron configuration for Pd is full-filled 4d, its adsorption ability should be weaker because of the extra stability from the d orbital. The oxidation rate of CO under steady-state conditions on various Pt group metal crystals is compared reported (Figure 6.13). The metal-oxygen bound energies of platinum group metals are within the range of 320-390kJ mol^{-1} and they are all quite active for CO oxidation. The CO oxidation rate follows the order of Pd, Rh>Pt>Ir. Similarly, the presence of surface embedded single metal can also dramatically change reaction energetics and barriers for the reactant and

intermediates involved in the reaction. The order of CO oxidation rate on Pt group metals is the same with our experimental results that the catalytic activity follow the order of Pd, Rh>Pt >Ir.

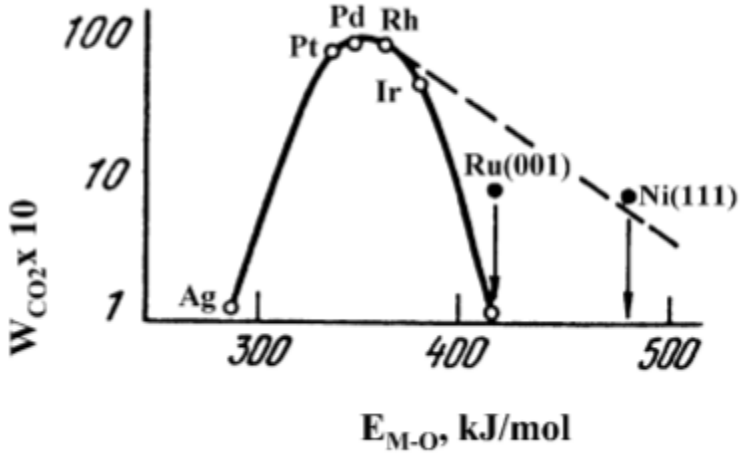

Figure 6.13 Dependence of the rate of CO oxidation on metals on the oxygen bond energy E_{M-O} (793K)[1]

On the other hand, to investigate the facet dependence of catalytic behavior, ZnO NPs with same mass of metal loading were synthesized. For ZnO NWs, the predominant crystal surfaces are {10-10} facets while different facets are exposed in ZnO NPs. The CO conversion vs. temperature curves of ZnO NWs and ZnO NPs supported single metal atoms catalysts is shown in Figure 6.14. We can clearly see that the activity is similar for supported Ir_1 catalysts. However, the Rh_1ZnO (NPs) SACs has decreased activity compared with Rh_1ZnO (NWs) while Pt_1ZnO (NPs) SACs has increased activity compared with Pt_1ZnO (NWs). Given the identical experimental parameters control, the catalytic activity difference between the NPs and NWs catalysts is due to the different facets exposed, which further verifies the catalytic performance of such SACs is determined by the unity of single atoms and supports.

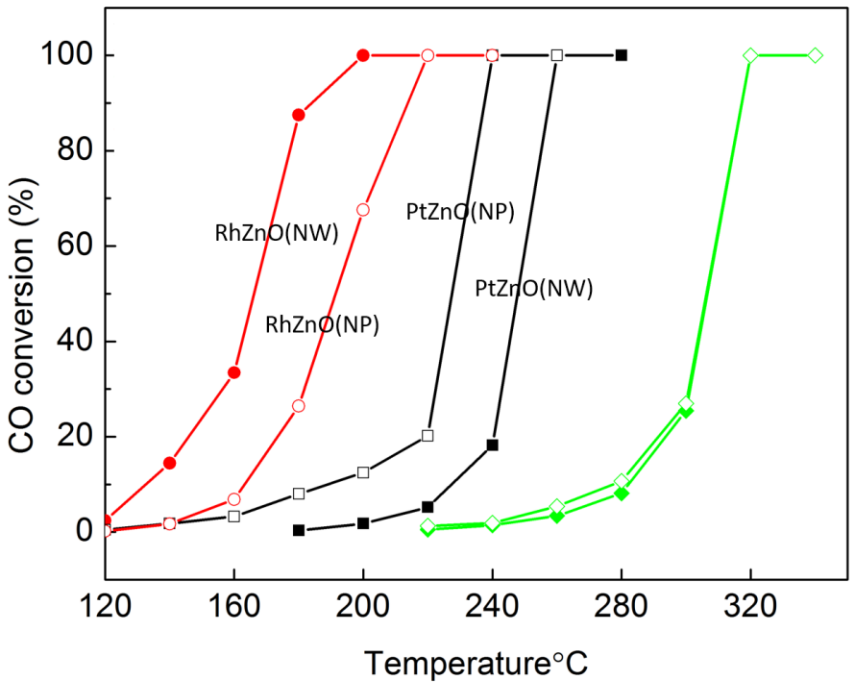

Figure 6.14 CO conversion vs. reaction temperature for various noble metal M_1/ZnO (NW) SACs and M_1/ZnO (NP) SACs. The order of activity is different on two sets experiments.

the stability of prepared M_1ZnO NWs catalysts was also tested for 800min. As shown in Figure 6.15c-d, both of Rh_1ZnO and Ir_1ZnO are quite stable after long time run at 210°C and 320°C, respectively. The oscillation in the CO conversion rate of Ir_1ZnO is repeatable but not clear yet. Since some of the Ir atoms have lower contrast when imaged in STEM, we currently suspect that single Ir atoms come in and out of ZnO surfaces in the reaction process. The high magnification HAADF images clearly show the individually dispersed Rh and Ir atoms, as marked with red and blue arrows in Figure 6.15a-b. Ir has a higher melting point and surface energy, leading to a good dispersion on the surface and strong interactions of Ir particles with the supports [232]. Rh single atoms were observed diffusive on Al_2O_3 surface at catalytic temperatures but not aggregated. The main reason is that the adsorption energy of Rhn per Rh atom decreases

with increasing cluster size, showing less affinity to form clusters when they are monodispersed on the surface.

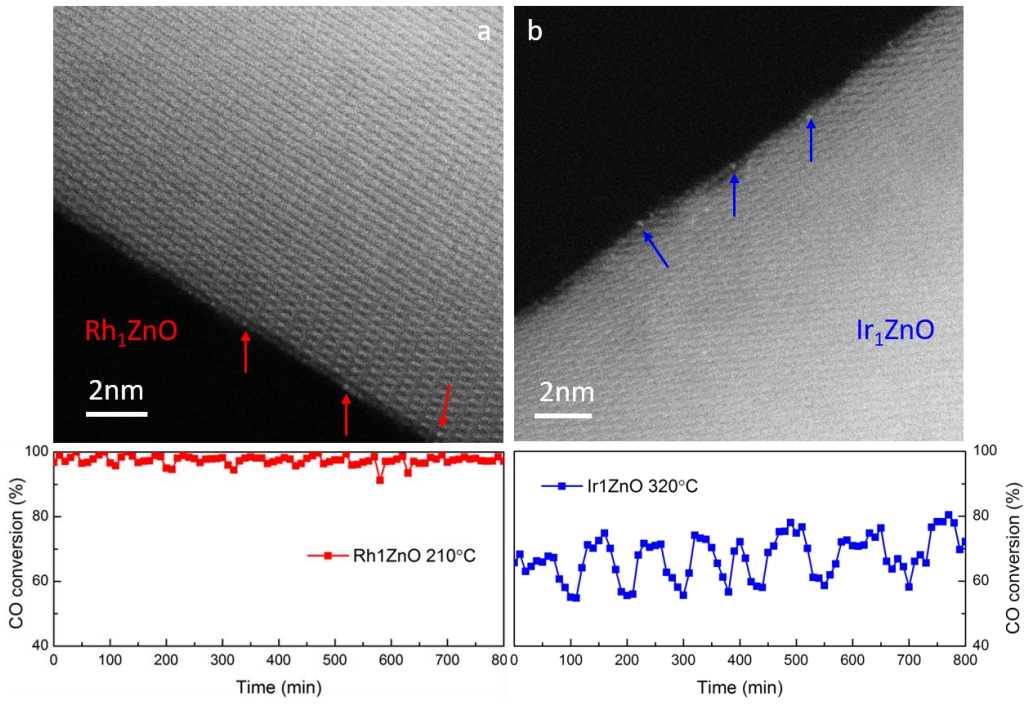

Figure 6.15 Stability test of Rh_1ZnO at 210°C and Ir_1ZnO at 320°C and the HAADF images of used catalysts. Both samples are quite stable after 800min test. Rh and Ir atoms, marked with red arrows and blue arrows in (a) and (b), remain atomically dispersion.

the Pd_1 and Pt_1 atoms grow into NPs after long time under catalytic conditions, marked by green arrow and pink arrow, respectively in Figure 6.16a-b. The average size of Pd and Pt NPs is around 2-3nm. Few single atoms can be observed in these samples. The CO conversion rate decreased about 50% in PdZnO catalyst and 10% in PtZnO catalyst after 800 min run, as shown in Figure 6.16c-d.

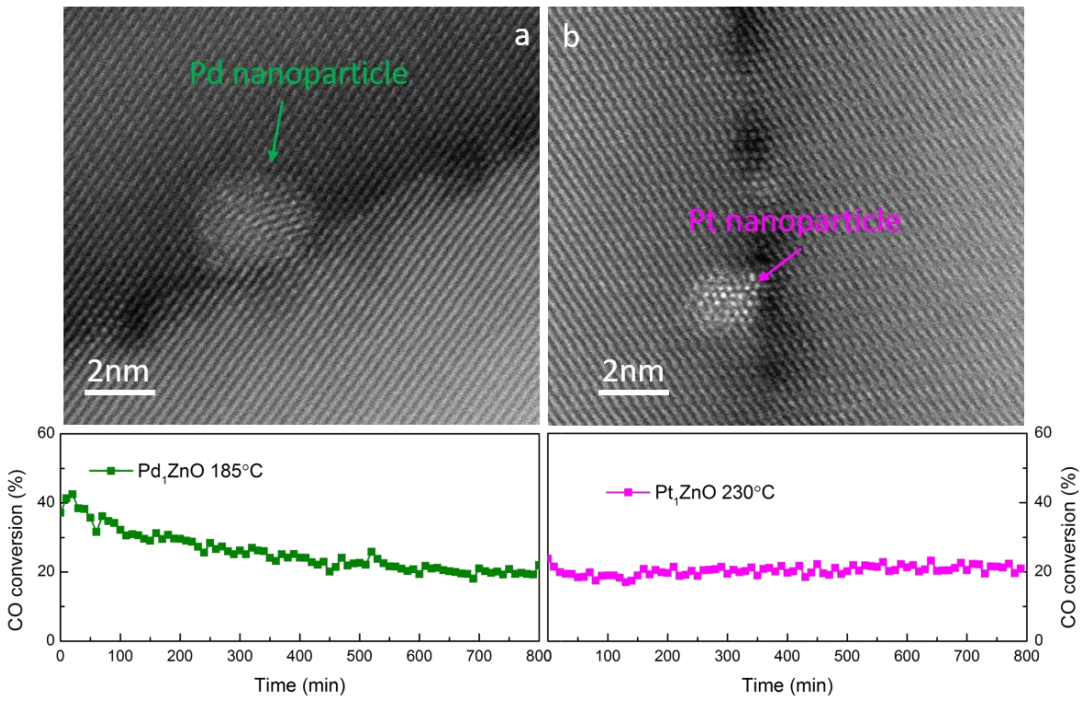

Figure 6.16 Stability test of Pd_1ZnO at 185°C and Pt_1ZnO at 320°C and the HAADF images of used catalysts. After 800min test, both of Pd and Pt single atoms grow into NPs, as indicated by green and pink arrows, respectively. The activity of PdZnO and PtZnO catalyst decrease with time and finally stabilized.

the experimental and theoretical results revealed that as the CO oxidation reaction proceeds, oxygen vacancies will anneal, resulting in coalescence of the remaining Pd to form large clusters [227]. In addition, the existence of CO can also induce coalescence of isolated Pd atoms [236]. As the reaction going on, single Pd atoms may form highly mobile Pd carbonyl complexes, which account for the cluster nucleation and coarsening. Similarly, CO also induces mobility among Pt adatoms through the formation of Pt carbonyls (Pt_1–CO), leading to agglomeration into clusters [237]. However, the Pt clusters formed is more like two-dimensional growth, which is different with Pd NPs. This may be explained by the strong interaction between Pt and ZnO support. The strong interaction between Pt NPs (below 2nm) may enable the heteroepitaxy relationship between Pt NPs and ZnO support [98]. Such two-dimentianal initial-stage Pt NPs have also been characterized on TiO2 support[238].

to summarize, M_1/ZnO (M=Pd, Pt, Rh, Ir) SACs were synthesized for CO oxidation. All of the SACs are highly active for CO oxidation compared with bare ZnO NWs. But their catalytic activities are quite different, which is caused by the different charge transfer between single M_1 metal atoms and ZnO supports. Rh_1ZnO and Ir_1ZnO catalysts is very stable and remain SACs even after 800min reaction while Pd_1ZnO and Pt_1ZnO catalysts deactivate and form Pd and Pt small NPs on the surface of ZnO NWs. By evaluating the activity and stability over the four catalysts, we conclude that Rh_1ZnO SACs is most promising among these catalysts.

Chapter 7 Future work

7.1 Pt_1/CeO_2-ZnO Nanowire Single-Atom Catalysts for Water-Gas Shift Reaction

Ceria supported Au and Pt nanocatalysts have demonstrated superior activity, selectivity and stability for water-gas shift (WGS) reaction [239, 240]. Downsizing noble metal nanoparticles (NPs) to small clusters or even single atoms is highly desirable for maximizing the effective use of rare and expensive noble metals provided that their catalytic performances are not compromised. It is believed that the active center in a supported SAC consists of the isolated individual metal atom plus its immediate neighbor atoms of the support. Therefore, it is highly desirable to fabricate SACs that are composed of individual metal atoms supported on small clusters of an appropriate metal oxide which are supported on another relatively inert and inexpensive material. In this work, we demonstrate the feasibility of this new approach by dispersing Pt single atoms onto CeO_2 nanoclusters which are supported on ZnO nanowires (NWs) and test the synthesized Pt_1/CeO_2-ZnO SACs for the WGS reaction.

ZnO NWs were fabricated by a thermal evaporation-condensation method in a high temperature tube furnace. The CeO_2-ZnO NW nanocomposites (5wt% of CeO_2) were prepared by adsorbing Ce salt onto the ZnO NWs via a wet chemistry method. The Ce-containing precipitates were then washed with deionized water, dried at 60°C overnight and calcined at 400°C for 4 h. The as-prepared CeO_2-ZnO NWs were then soaked into deionized water and a specific amount of Pt salt precursor was dropwise added into the solution and the resultant precipitates were filtered, thoroughly washed and dried at 60°C for 5h. The final Pt_1/CeO_2-ZnO SACs contained a nominal amount of 0.5wt% Pt.

The activity tests were conducted in a fixed-bed reactor with 50 mg of catalysts and the reaction feed gas composed of 2vol% CO/10vol% H_2O balanced with helium. The gas hourly space velocity (GHSV) was 48,000 ml/g_{cat}/h. The reaction feed gas mixture was preheated to 165°C. The effluent gas compositions were on-line analyzed by a gas chromatograph (HP 7890) equipped with a HayeSep DB column. The CO conversion was calculated based on the difference between inlet and outlet CO concentrations.

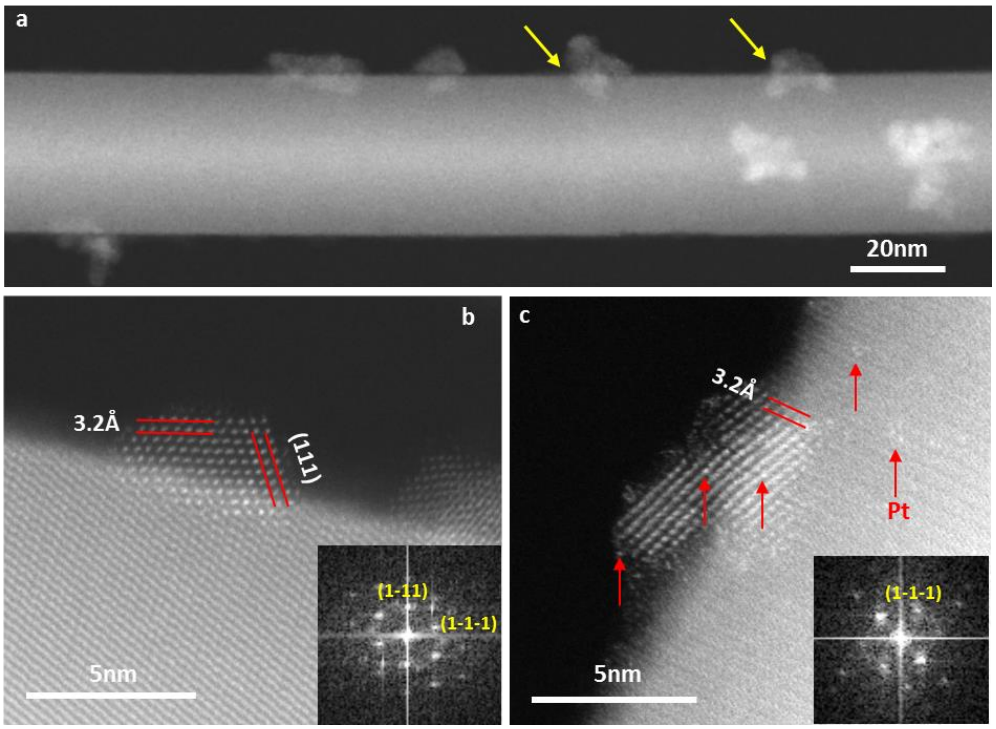

Figure 7.1 (a) Low magnification HAADF image of a typical CeO_2-ZnO NW. The aggregated CeO_2 NPs are indicated by the yellow arrows; (b) and (c) are atomic resolution HAADF images of a CeO_2-ZnO nanocomposite and a Pt_1/CeO_2-ZnO SAC. The exposed CeO_2 facets were identified as {111}.

Atomically dispersed Pt atoms are indicated by the red arrows. Figure 7.1a displays a HAADF image of a typical CeO_2-ZnO NW, revealing aggregates of small CeO_2 NPs with an average size of ~ 5 nm. Atomic resolution HAADF images, for example, Figure 7.1b, of the CeO_2-ZnO nanocomposites reveal that the CeO_2 NPs are well-faceted with primarily exposed {111} surfaces. Because of the 4 h calcination treatment at 400°C

there were few Ce single atoms on the ZnO NWs. Single Pt atoms were atomically dispersed onto both the CeO_2 NPs and the ZnO NWs as clearly revealed in Figure 7.1c (indicated by the red arrows). We did not observe any Pt clusters or NPs dispersed onto either the CeO_2 nanocystallites or the ZnO NWs. Therefore, we have successfully synthesized a 0.5 wt% Pt_1/CeO_2-ZnO NWs SAC.

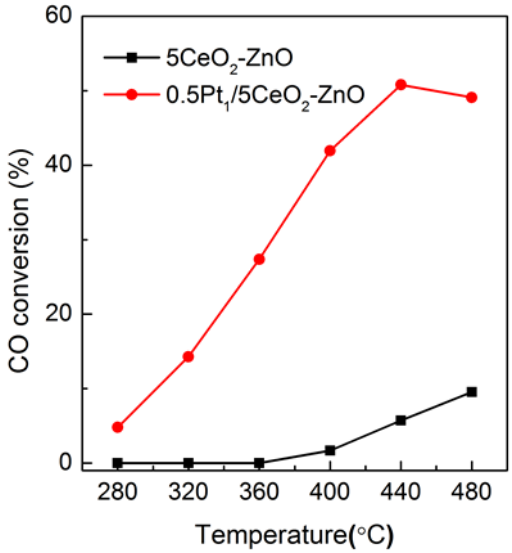

Figure 7.2 CO conversion vs temperature for WGS reaction on bare CeO_2-ZnO and 0.5wt% Pt_1/CeO_2-ZnO SAC. The SAC exhibited much higher activity.

Figure 7.2 shows the CO conversion profile as a function of reaction temperature over the as-synthesized $0.5Pt_1/CeO_2$-ZnO SAC. The CeO_2-ZnO nanocomposites were also tested as a control. The addition of the Pt single atoms clearly significantly enhanced the CO conversion rate in the temperature range of 280°C - 500°C. The strong interaction between the Pt_1 atoms and the CeO_2 surfaces may be responsible for the observed activity enhancement. The activity drop at reaction temperatures > ~ 440°C is related to the activation of the reverse WGS reaction. It is expected that when the sizes of the supported CeO_2 clusters become much smaller (< 1 nm) the catalytic properties of the Pt_1/CeO_2-ZnO SACs will be significantly modified.

7.2 Facet Selective Growth of Iridium Chains/Wires of Single-Atom Width on the {10-10} Surfaces of ZnO Nanowires

Self-assembly of individual atoms into ordered nanostructures is not only of fundamental interest but also provides unique electronic, magnetic or catalytic properties. Noble metal such as Pd or Ir were reported to form atomic chains on W (110)[241]. Recent work on fabricating Ir wires of atomic dimensions on Ge (001) surface suggests that electronic effects play a major role in stabilizing atomic size metal wires [242]. All the previous studies, however, focused on clean single crystal substrates and ultrahigh vacuum manipulation. We developed a unique process to synthesize high-surface area, ultra-clean ZnO nanowires (NWs) that primarily consist of ZnO {10-10} and {11-20} facets. In this work, we report, for the first time, the synthesis and characterization of Ir chains/wires of single-atom width that selectively grow on the {10-10} nanofacets of ZnO NWs. More importantly, we achieved fabrication of Ir atomic chains by a scalable wet chemistry and post-synthesis treatment process. Aberration-corrected HAADF-STEM images reveal that all the {10-10} nanofacets of the ZnO NWs were decorated with single-atom wide Ir chains/wires or Ir atoms. The strong metal-support interaction is responsible for the growth and stabilization of such atomic wide Ir wires.

the Ir/ZnO sample was synthesized by a modified adsorption method. Briefly, Ir precursors were dropwise added into the solution of pre-formed ZnO NWs. The resultant precipitate was filtered, washed with deionized water and dried. Then the Ir/ZnO NWs were calcined in air at 300°C - 500°C for 2-10 hrs.

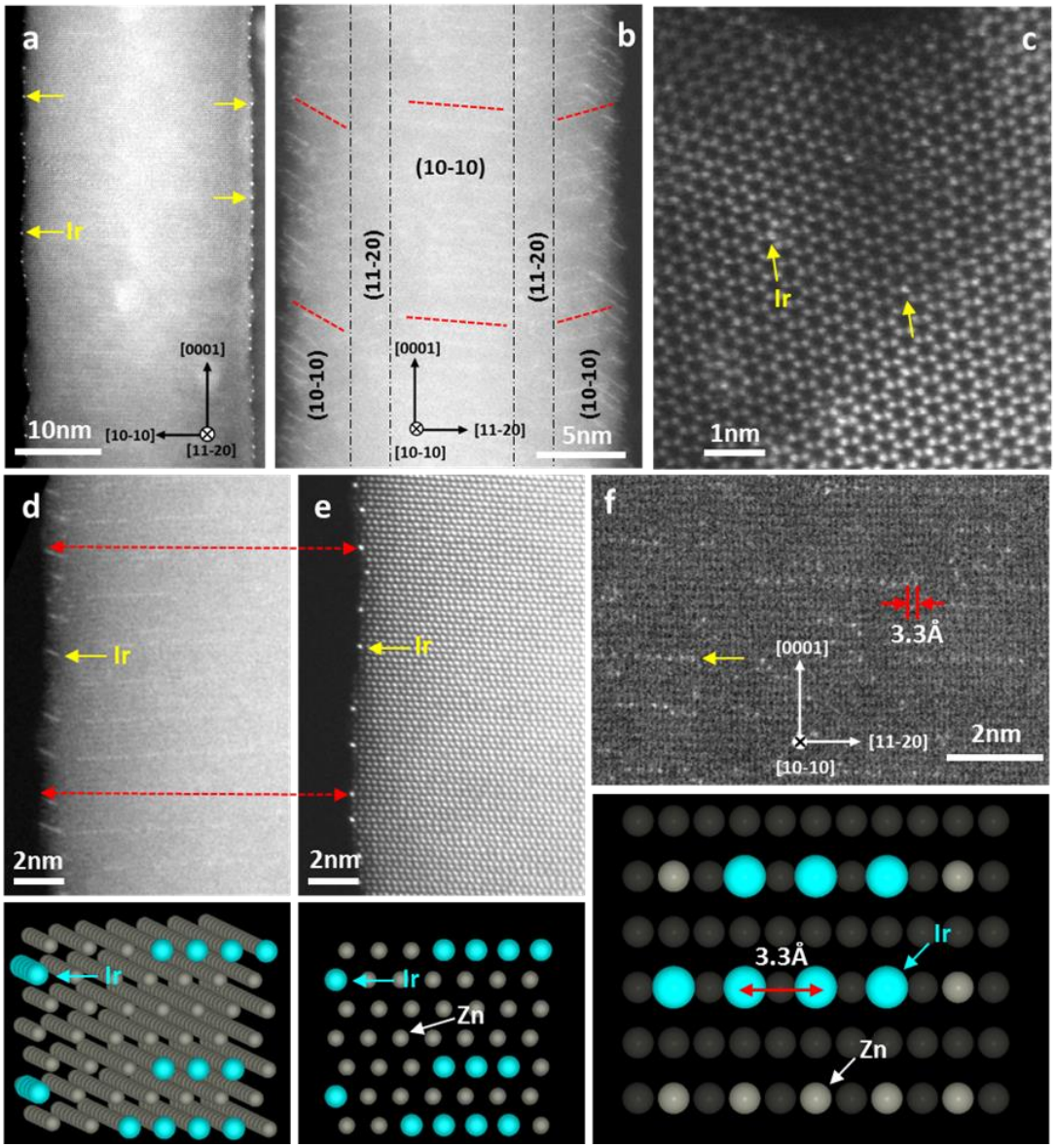

Figure 7.3 HAADF images of a typical Ir/ZnO NW with electron beam close to [11-20] (a, d, e), [10-10] (b, f) and [0001] (c) zone, respectively. The bright dots and lines represent Ir atoms. The schematic models are shown below the HAADF images (d-f). The single-atom wide Ir chains preferentially grow on the {10-10} surfaces of the ZnO NWs.

Figure 7.3a shows a representative HAADF image of the synthesized Ir/ZnO NWs with the electron beam oriented close to the ZnO [11-20] zone axis. The bright dots (indicated by the yellow arrows) represent columns of Ir atoms decorating the ZnO {10-10} surfaces. Figure 7.3b shows an image of another ZnO NW with the [10-10] zone

axis titled toward the [0001] direction in order to reveal the Ir atoms on the different facets of the ZnO NW. It is clearly seen that atomic wide lines of Ir atoms (indicated by the dashed red lines) preferentially grew on the ZnO {10-10} but not on the {11-20} facets. Figure 7.3c shows an image of an Ir/ZnO NW oriented to the [0001] zone axis revealing the presence of individual Ir atoms without the occurrence of Ir chains on the ZnO {0001} surfaces. To clearly understand the structure of the Ir chains Figure 7.3d and e show exactly the same region of a ZnO NW but with different tilting angles. When the electron beam was along the ZnO [11-20] zone axis the bright Ir atoms were perfectly aligned with respect to the electron beam (Figure 7.3e). When the electron beam tilted away from the [11-20] zone axis the Ir chains were represented by the bright short lines (Figure 7.3d). Figure 1f shows an image with the electron beam close to the [10-10] zone axis, clearly revealing the arrangement of the Ir atoms with respect to the Zn atoms on the ZnO {10-10} surface (see the schematic illustration). The growth processes of the atom-size Ir wires, their structures, and their catalytic properties will be further investigated.

References:

1. Savchenko, V.; Boreskov, G.; Kalinkin, A.; Salanov, A., State of oxygen on metal surfaces and catalytic activity for the oxidation of carbon monoxide. *Kinet. Catal.(Engl. Transl.);(United States)* **1983,** 24, (5).

2. Pokropivny, V. V.; Skorokhod, V. V., Classification of nanostructures by dimensionality and concept of surface forms engineering in nanomaterial science. *Materials Science and Engineering: C* **2007,** 27, (5-8), 990-993.

3. Weintraub, B.; Zhou, Z.; Li, Y.; Deng, Y., Solution synthesis of one-dimensional ZnO nanomaterials and their applications. *Nanoscale* **2010,** 2, (9), 1573-1587.

4. Xia, Y.; Yang, P.; Sun, Y.; Wu, Y.; Mayers, B.; Gates, B.; Yin, Y.; Kim, F.; Yan, H., One-dimensional nanostructures: synthesis, characterization, and applications. *Advanced materials* **2003,** 15, (5), 353-389.

5. Kuchibhatla, S. V. N. T.; Karakoti, A. S.; Bera, D.; Seal, S., One dimensional nanostructured materials. *Progress in Materials Science* **2007,** 52, (5), 699-913.

6. Goldthorpe, I. A.; Marshall, A. F.; McIntyre, P. C., Inhibiting strain-induced surface roughening: dislocation-free Ge/Si and Ge/SiGe core− shell nanowires. *Nano letters* **2009,** 9, (11), 3715-3719.

7. Chen, L.; Luo, L.; Chen, Z.; Zhang, M.; Zapien, J. A.; Lee, C. S.; Lee, S. T., ZnO/Au composite nanoarrays as substrates for surface-enhanced Raman scattering detection. The *Journal of Physical Chemistry C* **2009,** 114, (1), 93-100.

8. Gao, W.; Manesh, K. M.; Hua, J.; Sattayasamitsathit, S.; Wang, J., Hybrid nanomotor: A catalytically/magnetically powered adaptive nanowire swimmer. *Small* **2011,** 7, (14), 2047-2051.

9. Gentile, P.; David, T.; Dhalluin, F.; Buttard, D.; Pauc, N.; Den Hertog, M.; Ferret, P.; Baron, T., the growth of small diameter silicon nanowires to nanotrees. *Nanotechnology* **2008,** 19, (12), 125608.

10. Law, M.; Greene, L. E.; Radenovic, A.; Kuykendall, T.; Liphardt, J.; Yang, P., ZnO-Al2O3 and ZnO-TiO2 core-shell nanowire dye-sensitized solar cells. *J Phys Chem B* **2006,** 110, (45), 22652-63.

11. Kamat, P. V., Manipulation of Charge Transfer Across Semiconductor Interface. A Criterion That Cannot Be Ignored in Photocatalyst Design. *J Phys Chem Lett* **2012,** 3, (5), 663-72.

12. Tang, J.; Huo, Z.; Brittman, S.; Gao, H.; Yang, P., Solution-processed core-shell nanowires for efficient photovoltaic cells. *Nature nanotechnology* **2011**.

13. Wang, K.; Chen, J.; Zhou, W.; Zhang, Y.; Yan, Y., Direct growth of highly mismatched type II ZnO/ZnSe core/shell nanowire arrays on transparent conducting oxide substrates for solar cell applications. *Advanced …* **2008**.

14. Wang, X.; Ren, P.; Fan, H., Room-temperature solid state synthesis of ZnO/Bi_2O_3 heterojunction and their solar light photocatalytic performance. *Materials Research Bulletin* **2015,** 64, 82-87.

15. Tak, Y.; Hong, S. J.; Lee, J. S.; Yong, K., Fabrication of ZnO/CdS core/shell nanowire arrays for efficient solar energy conversion. *Journal of Materials Chemistry* **2009,** 19, (33), 5945.

16. Tak, Y.; Yong, K., A novel heterostructure of Co3O4/ZnO nanowire array fabricated by photochemical coating method. The *Journal of Physical Chemistry C* **2008,** 112, (1), 74-79.

17. Bi, Y.; Hu, H.; Ouyang, S.; Jiao, Z.; Lu, G.; Ye, J., Selective growth of Ag3PO4 submicro-cubes on Ag nanowires to fabricate necklace-like heterostructures for photocatalytic applications. *J. Mater. Chem.* **2012**.

18. Cozzoli, P. D.; Fanizza, E.; Comparelli, R., Role of metal nanoparticles in TiO2/Ag nanocomposite-based microheterogeneous photocatalysis. The *Journal of …* **2004**.

19. Hinnemann, B.; Moses, P. G.; Bonde, J., Biomimetic hydrogen evolution: MoS2 nanoparticles as catalyst for hydrogen evolution. *Journal of the …* **2005**.

20. Wang, X.; Peng, K. Q.; Pan, X. J.; Chen, X.; Yang, Y.; Li, L.; Meng, X. M.; Zhang, W. J.; Lee, S. T., High-Performance Silicon Nanowire Array Photoelectrochemical Solar Cells through Surface Passivation and Modification. *Angewandte Chemie International Edition* **2011,** 50, (42), 9861-9865.

21. Barroso, M.; Mesa, C. A.; Pendlebury, S. R.; Cowan, A. J.; Hisatomi, T.; Sivula, K.; Grätzel, M.; Klug, D. R.; Durrant, J. R., Dynamics of photogenerated holes in surface modified α-Fe2O3 photoanodes for solar water splitting. *Proceedings of the National Academy of Sciences* **2012,** 109, (39), 15640-15645.

22. Kast, P.; Friedrich, M.; Girgsdies, F.; Kröhnert, J.; Teschner, D.; Lunkenbein, T.; Behrens, M.; Schlögl, R., Strong metal-support interaction and alloying in Pd/ZnO catalysts for CO oxidation. *Catalysis today* **2016,** 260, 21-31.

23. Pal, J.; Pal, T., Faceted metal and metal oxide nanoparticles: design, fabrication and catalysis. *Faceted metal and metal oxide nanoparticles: design, fabrication and catalysis* **2015**.

24. Harju, H.; Lehtonen, J.; Lefferts, L., Steam- and autothermal-reforming of n-butanol over Rh/ZrO2 catalyst. *Catalysis today* **2015,** 244, 47-57.

25. Ding, K.; Gulec, A.; Johnson, A. M.; Schweitzer, N. M.; Stucky, G. D.; Marks, L. D.; Stair, P. C., Identification of active sites in CO oxidation and water-gas shift over supported Pt catalysts. *Science* **2015,** 350, (6257), 189-92.

26. Zhang, J.; Zhong, Z.; Cao, M. X.; Hu, P.; Sullivan, M. B.; Chen, L., Ethanol Steam Reforming on Rh Catalysts: theoretical and Experimental Understanding. *ACS Catalysis* **2014,** 4, (2), 448-456.

27. Liu, X.; Liu, M. H.; Luo, Y. C.; Mou, C. Y.; Lin, S. D.; Cheng, H.; Chen, J. M.; Lee, J. F.; Lin, T. S., Strong metal-support interactions between gold nanoparticles and ZnO nanorods in CO oxidation. *J Am Chem Soc* **2012,** 134, (24), 10251-8.

28. Zhang, Y.; Xiang, Q.; Xu, J.; Xu, P.; Pan, Q., Self-assemblies of Pd nanoparticles on the surfaces of single crystal ZnO nanowires for chemical sensors with enhanced performances. *Self-assemblies of Pd nanoparticles on the surfaces of single crystal ZnO nanowires for chemical sensors with enhanced performances* **2009**.

29. Ramos-Fernández, E. V.; Sepúlveda-Escribano, A., Enhancing the catalytic performance of Pt/ZnO in the vapour phase hydrogenation of crotonaldehyde by the addition of Cr to the support. *Enhancing the catalytic performance of Pt/ZnO in the vapour phase hydrogenation of crotonaldehyde by the addition of Cr to the support* **2008**.

30. Henry, C. R., Surface studies of supported model catalysts. *Surface Science Reports* **1998,** 31, (7), 231-325.

31. Liu, J. Y., Advanced Electron Microscopy of Metal-Support Interactions in Supported Metal Catalysts. *Chemcatchem* **2011,** 3, (6), 934-948.

32. Gorbenko, O. Y.; Samoilenkov, S.; Graboy, I.; Kaul, A., Epitaxial stabilization of oxides in thin films. *Chemistry of materials* **2002,** 14, (10), 4026-4043.

33. Liu, J.; Qiao, B.; Song, Y.; Huang, Y.; Liu, J. J., Hetero-epitaxially anchoring Au nanoparticles onto ZnO nanowires for CO oxidation. *Chemical Communications* **2015**.

34. Liu, J.; Qiao, B.; Song, Y.; Tang, H.; Huang, Y.; Liu, J. J., Highly active and sintering-resistant heteroepitaxy of Au nanoparticles on ZnO nanowires for CO oxidation. *Journal of Energy Chemistry* **2016**.

35. Zhang, H.; Sun, J.; Dagle, V. L.; Halevi, B.; Datye, A. K.; Wang, Y., Influence of ZnO Facets on Pd/ZnO Catalysts for Methanol Steam Reforming. *ACS Catalysis* **2014,** 4, (7), 2379-2386.

36. Wang, Z. L., Zinc oxide nanostructures: growth, properties and applications. *Journal of Physics: Condensed Matter* **2004,** 16, (25), R829-R858.

37. Janotti, A.; Van de Walle, C. G., Fundamentals of zinc oxide as a semiconductor. *Reports on Progress in Physics* **2009,** 72, (12), 126501.

38. Bagnall, D.; Chen, Y.; Zhu, Z.; Yao, T.; Koyama, S.; Shen, M. Y.; Goto, T., Optically pumped lasing of ZnO at room temperature. *Applied Physics Letters* **1997,** 70, (17), 2230-2232.

39. Reynolds, D. C.; Look, D. C.; Jogai, B., Optically pumped ultraviolet lasing from ZnO. *Solid State Communications* **1996,** 99, (12), 873-875.

40. Moses, W. W., Current trends in scintillator detectors and materials. *Nuclear Instruments and Methods in Physics Research Section A: Accelerators, Spectrometers, Detectors and Associated Equipment* **2002,** 487, (1), 123-128.

41. Wee, J.-H., Applications of proton exchange membrane fuel cell systems. *Renewable and sustainable energy reviews* **2007,** 11, (8), 1720-1738.

42. Choi, Y.; Stenger, H. G., Fuel cell grade hydrogen from methanol on a commercial Cu/ZnO/Al 2 O 3 catalyst. *Applied Catalysis B: Environmental* **2002,** 38, (4), 259-269.

43. Ahmed, S.; Krumpelt, M., Hydrogen from hydrocarbon fuels for fuel cells. *International journal of hydrogen energy* **2001,** 26, (4), 291-301.

44. Damle, A. S., Hydrogen production by reforming of liquid hydrocarbons in a membrane reactor for portable power generation—model simulations. *Journal of Power Sources* **2008,** 180, (1), 516-529.

45. Brown, L. F., A comparative study of fuels for on-board hydrogen production for fuel-cell-powered automobiles. *International Journal of Hydrogen Energy* **2001,** 26, (4), 381-397.

46. Dhar, H.; Christner, L.; Kush, A., Nature of CO adsorption during H 2 oxidation in relation to modeling for CO poisoning of a fuel cell anode. *Journal of the Electrochemical Society* **1987,** 134, (12), 3021-3026.

47. Mateos-Pedrero, C.; Silva, H.; Tanaka, D. A.; Liguori, S.; Iulianelli, A.; Basile, A.; Mendes, A., CuO/ZnO catalysts for methanol steam reforming: the role of the support polarity ratio and surface area. *Applied Catalysis B: Environmental* **2015,** 174, 67-76.

48. Iwasa, N.; Masuda, S.; Takezawa, N., Steam reforming of methanol over Ni, Co, Pd and Pt supported on ZnO. *Steam reforming of methanol over Ni, Co, Pd and Pt supported on ZnO* **1995**.

49. Karim, A. M.; Conant, T.; Datye, A. K., Controlling ZnO morphology for improved methanol steam reforming reactivity. *Physical chemistry chemical physics : PCCP* **2008,** 10, (36), 5584-5590.

50. Bai, X.; Gao, P.; Wang, Z. L.; Wang, E., Dual-mode mechanical resonance of individual ZnO nanobelts. *Applied Physics Letters* **2003,** 82, (26), 4806-4808.

51. Xiong, Y.; Wiley, B.; Chen, J.; Li, Z. Y.; Yin, Y.; Xia, Y., Corrosion-Based Synthesis of Single-Crystal Pd Nanoboxes and Nanocages and their Surface Plasmon Properties. *Angewandte Chemie International Edition* **2005,** 44, (48), 7913-7917.

52. Wu, X.; Qu, F.; Zhang, X.; Cai, W.; Shen, G., Fabrication of ZnO ring-like nanostructures at a moderate temperature via a thermal evaporation process. *Journal of Alloys and Compounds* **2009,** 486, (1), L13-L16.

53. Cao, C.; Xia, G.; Holladay, J.; Jones, E.; Wang, Y., Kinetic studies of methanol steam reforming over Pd/ZnO catalyst using a microchannel reactor. *Applied Catalysis A: General* **2004,** 262, (1), 19-29.

54. Chang, P.-C.; Fan, Z.; Wang, D.; Tseng, W.-Y.; Chiou, W.-A.; Hong, J.; Lu, J. G., ZnO nanowires synthesized by vapor trapping CVD method. *Chemistry of materials* **2004,** 16, (24), 5133-5137.

55. Lupan, O.; Emelchenko, G.; Ursaki, V.; Chai, G.; Redkin, A.; Gruzintsev, A.; Tiginyanu, I.; Chow, L.; Ono, L.; Cuenya, B. R., Synthesis and characterization of ZnO nanowires for nanosensor applications. *Materials Research Bulletin* **2010,** 45, (8), 1026-1032.

56. Pan, Z. W.; Dai, Z. R.; Wang, Z. L., Nanobelts of semiconducting oxides. *Science* **2001,** 291, (5510), 1947-1949.

57. Huang, M. H.; Wu, Y.; Feick, H.; Tran, N.; Weber, E.; Yang, P., Catalytic growth of zinc oxide nanowires by vapor transport. *Advanced Materials* **2001,** 13, (2), 113-116.

58. Wang, Z. L., Splendid One-Dimensional Nanostructures of Zinc Oxide: A New Nanomaterial Family for Nanotechnology. *Acs Nano* **2008,** 2, (10), 1987-1992.

59. Wang, J.; Yang, C.; Chen, P.; Su, C.; Chen, W.; Chiu, K.; Chou, W., Catalyst-free highly vertically aligned ZnO nanoneedle arrays grown by plasma-assisted molecular beam epitaxy. *Applied Physics A* **2009,** 97, (3), 553-557.

60. Xu, S.; Wang, Z. L., One-dimensional ZnO nanostructures: Solution growth and functional properties. *Nano Research* **2011,** 4, (11), 1013-1098.

61. Dang, H.; Wang, J.; Fan, S., the synthesis of metal oxide nanowires by directly heating metal samples in appropriate oxygen atmospheres. *Nanotechnology* **2003,** 14, (7), 738.

62. Law, J.; Boothroyd, C.; Thong, J., Site-specific growth of ZnO nanowires from patterned Zn via compatible semiconductor processing. *Journal of Crystal Growth* **2008,** 310, (10), 2485-2492.

63. Li, F.; Li, Z.; Jin, F., Fabrication and characterization of ZnO micro and nanostructures prepared by thermal evaporation. *Physica B: Condensed Matter* **2008,** 403, (4), 664-669.

64. Fan, Z.; Wang, D.; Chang, P.-C.; Tseng, W.-Y.; Lu, J. G., ZnO nanowire field-effect transistor and oxygen sensing property. *Applied Physics Letters* **2004,** 85, (24), 5923-5925.

65. Tang, Y.; Hu, X.; Chen, M.; Luo, L.; Li, B.; Zhang, L., CdSe nanocrystal sensitized ZnO core-shell nanorod array films: preparation and photovoltaic properties. *Electrochimica Acta* **2009,** 54, (10), 2742-2747.

66. Chen, C.-Y.; Lin, C.; Chen, M.; Lin, G.; He, J.-H., ZnO/Al2O3 core–shell nanorod arrays: growth, structural characterization, and luminescent properties. *Nanotechnology* **2009,** 20, (18), 185605.

67. Panda, S. K.; Dev, A.; Chaudhuri, S., Fabrication and luminescent properties of c-axis oriented ZnO-ZnS core-shell and ZnS nanorod arrays by sulfidation of aligned ZnO nanorod arrays. The *Journal of Physical Chemistry C* **2007,** 111, (13), 5039-5043.

68. Plank, N. O.; Howard, I.; Rao, A.; Wilson, M. W.; Ducati, C.; Mane, R. S.; Bendall, J. S.; Louca, R. R.; Greenham, N. C.; Miura, H., Efficient ZnO Nanowire Solid-State Dye-Sensitized Solar Cells Using Organic Dyes and Core− shell Nanostructures. The *Journal of Physical Chemistry C* **2009,** 113, (43), 18515-18522.

69. Shi, L.; Xu, Y.; Hark, S.; Liu, Y.; Wang, S.; Peng, L.-m.; Wong, K.; Li, Q., Optical and electrical performance of SnO2 capped ZnO nanowire arrays. *Nano letters* **2007,** 7, (12), 3559-3563.

70. Wang, X.; Zhu, H.; Xu, Y.; Wang, H.; Tao, Y.; Hark, S.; Xiao, X.; Li, Q., Aligned ZnO/CdTe core− shell nanocable arrays on indium tin oxide: synthesis and photoelectrochemical properties. *ACS nano* **2010,** 4, (6), 3302-3308.

71. Plank, N. O.; Snaith, H. J.; Ducati, C.; Bendall, J. S.; Schmidt-Mende, L.; Welland, M. E., A simple low temperature synthesis route for ZnO-MgO core-shell nanowires. *Nanotechnology* **2008,** 19, (46), 465603.

72. Yang, Y.; Xu, L.; Su, C.; Che, J.; Sun, W.; Gao, H., Electrospun ZnO/Bi 2 O 3 Nanofibers with Enhanced Photocatalytic Activity. *Journal of Nanomaterials* **2014,** 2014.

73. Leutwyler, W. K.; Bürgi, S. L.; Burgl, H., Semiconductor clusters, nanocrystals, and quantum dots. *Science* **1996,** 271, (5251), 933-937.

74. Ding, H.; Shao, J.; Ding, Y.; Liu, W.; Tian, H.; Li, X., One-Dimensional Au-ZnO Heteronanostructures for Ultraviolet Light Detectors by a Two-Step Dielectrophoretic Assembly Method. *ACS Appl Mater Interfaces* **2015,** 7, (23), 12713-8.

75. Guo, J.; Zhang, J.; Zhu, M.; Ju, D.; Xu, H.; Cao, B., High-performance gas sensor based on ZnO nanowires functionalized by Au nanoparticles. *Sensors and Actuators B: Chemical* **2014,** 199, 339-345.

76. Chen, T.; Xing, G. Z.; Zhang, Z.; Chen, H. Y.; Wu, T., Tailoring the photoluminescence of ZnO nanowires using Au nanoparticles. *Nanotechnology* **2008,** 19, (43), 435711.

77. Lin, C. A.; Tsai, D. S.; Chen, C. Y.; He, J. H., Significant enhancement of yellow-green light emission of ZnO nanorod arrays using Ag island films. *Nanoscale* **2011,** 3, (3), 1195-9.

78. Deng, S.; Fan, H. M.; Zhang, X.; Loh, K. P.; Cheng, C. L.; Sow, C. H.; Foo, Y. L., An effective surface-enhanced Raman scattering template based on a Ag nanocluster-ZnO nanowire array. *Nanotechnology* **2009,** 20, (17), 175705.

79. Lin, J. M.; Lin, H. Y.; Cheng, C. L.; Chen, Y. F., Giant enhancement of bandgap emission of ZnO nanorods by platinum nanoparticles. *Nanotechnology* **2006,** 17, (17), 4391-4394.

80. Katoch, A.; Choi, S.-W.; Sun, G.-J.; Kim, S. S., Pt Nanoparticle-Decorated ZnO Nanowire Sensors for Detecting Benzene at Room Temperature. *Journal of nanoscience and nanotechnology* **2013,** 13, (10), 7097-7099.

81. Bera, A.; Ghosh, T.; Basak, D., Enhanced photoluminescence and photoconductivity of ZnO nanowires with sputtered Zn. *ACS Appl Mater Interfaces* **2010,** 2, (10), 2898-903.

82. Bera, A.; Basak, D., Pd-nanoparticle-decorated ZnO nanowires: ultraviolet photosensitivity and photoluminescence properties. *Nanotechnology* **2011,** 22, (26), 265501.

83. Park, S.; Kim, S.; Ko, H.; Lee, C., Surface Plasmon Resonance-Enhanced Luminescence in Pd-Functionalized ZnO Nanowires. *Journal of Nanoscience and Nanotechnology* **2015,** 15, (7), 5301-5305.

84. Liu, H.; Liu, J., Faceted ZnO Nanowire Supported Pd Catalyst for the Methanol Steam Reforming. *Microscopy and Microanalysis* **2010,** 16, (S2), 1206-1207.

85. Tang, Y.; Zhao, D.; Zhang, J.; Shen, D., Quenching of the surface-state-related photoluminescence in Ni-coated ZnO nanowires. *Physica B: Condensed Matter* **2010,** 405, (21), 4551-4555.

86. Sakano, T.; Tanaka, Y.; Nishimura, R.; Nedyalkov, N. N.; Atanasov, P. A.; Saiki, T.; Obara, M., Surface enhanced Raman scattering properties using Au-coated ZnO nanorods grown by two-step, off-axis pulsed laser deposition. *Journal of Physics D: Applied Physics* **2008,** 41, (23), 235304.

87. Zheng, Y.; Zheng, L.; Zhan, Y.; Lin, X.; Zheng, Q.; Wei, K., Ag/ZnO heterostructure nanocrystals: synthesis, characterization, and photocatalysis. *Inorganic chemistry* **2007,** 46, (17), 6980-6986.

88. Wei, J.; Jiang, N.; Xu, J.; Bai, X.; Liu, J., Strong Coupling between ZnO Excitons and Localized Surface Plasmons of Silver Nanoparticles Studied by STEM-EELS. *Nano Lett* **2015,** 15, (9), 5926-31.

89. Kenanakis, G.; Giannakoudakis, Z.; Vernardou, D.; Savvakis, C.; Katsarakis, N., Photocatalytic degradation of stearic acid by ZnO thin films and nanostructures deposited by different chemical routes. *Catalysis today* **2010,** 151, (1), 34-38.

90. Yin, X.; Que, W.; Fei, D.; Shen, F.; Guo, Q., Ag nanoparticle/ZnO nanorods nanocomposites derived by a seed-mediated method and their photocatalytic properties. *Journal of Alloys and Compounds* **2012,** 524, (0), 13-21.

91. Lin, S.-L.; Hsu, K.-C.; Hsu, C.-H.; Chen, D.-H., Hydrogen treatment-improved uniform deposition of Ag nanoparticles on ZnO nanorod arrays and their visible-light photocatalytic and surface-enhanced Raman scattering properties. *Nanoscale research letters* **2013,** 8, (1), 1-9.

92. Liu, J.; Xu, J.; Huang, Y.; Liu, J., ZnO nanowire-supported Ag catalyst for methanol steam reforming. *Microscopy and Microanalysis* **2014,** 20, (S3), 508-509.

93. Iwasa, N.; Masuda, S.; Takezawa, N., Steam Reforming of Methanol over Ni, Co, Pd and Pt Supported on ZnO. *Reaction Kinetics and Catalysis Letters* **1995,** 55, (2), 349-353.

94. Gupta, M.; He, J.; Nguyen, T.; Petzold, F.; Fonseca, D.; Jasinski, J. B.; Sunkara, M. K., "Nanowire catalysts for ultra-deep hydro-desulfurization and aromatic hydrogenation". *Applied Catalysis B: Environmental* **2016,** 180, 246-254.

95. Song, C., An overview of new approaches to deep desulfurization for ultra-clean gasoline, diesel fuel and jet fuel. *Catalysis today* **2003,** 86, (1), 211-263.

96. Trimm, D. L.; Önsan, Z. I., Onboard fuel conversion for hydrogen-fuel-cell-driven vehicles. *Catalysis Reviews* **2001,** 43, (1-2), 31-84.

97. Iwasa, N.; Masuda, S.; Ogawa, N.; Takezawa, N., Steam reforming of methanol over Pd/ZnO: Effect of the formation of PdZn alloys upon the reaction. *Applied Catalysis A: General* **1995,** 125, (1), 145-157.

98. Liu, J.; Qiao, B.; Song, Y.; Huang, Y.; Liu, J. J., Synthesis of Anchored Bimetallic Catalysts via Epitaxy. *Catalysts* **2016,** 6, (6), 88.

99. Spencer, M. J. S., Gas sensing applications of 1D-nanostructured zinc oxide: Insights from density functional theory calculations. *Progress in Materials Science* **2012,** 57, (3), 437-486.

100. Kim, K.; Song, Y.-W.; Chang, S.; Kim, I.-H.; Kim, S.; Lee, S. Y., Fabrication and characterization of Ga-doped ZnO nanowire gas sensor for the detection of CO. *Thin Solid Films* **2009,** 518, (4), 1190-1193.

101. Hu, Y.; Liu, Y.; Xu, H.; Liang, X.; Peng, L.-M.; Lam, N.; Wong, K.; Li, Q., Quantitative study on the effect of surface treatments on the electric characteristics of ZnO nanowires. The *Journal of Physical Chemistry C* **2008,** 112, (37), 14225-14228.

102. Tien, L.; Sadik, P.; Lin, J.; Pearton, S.; Norton, D.; Wang, H.; Ren, F.; Kang, B., Hydrogen-selective sensing at room temperature with ZnO nanorods. **2005**.

103. Pala, R. G. S.; Metiu, H., Selective promotion of different modes of methanol adsorption via the cation substitutional doping of a ZnO surface. *Journal of Catalysis* **2008,** 254, (2), 325-331.

104. Zhao, Y.; Shen, B.; Zhang, W.; Tian, R.; Zhang, Z.; Gao, J., Hydrodesulfurization and hydrodearomatization activities of catalyst containing ETS-10 and AlPO 4-5 on Daqing FCC diesel. *Fuel* **2008,** 87, (10), 2343-2346.

105. Liu, J., Catalysis by Supported Metal Single Atoms. *ACS Catalysis* **2016**.

106. Gu, X.-K.; Qiao, B.; Huang, C.-Q.; Ding, W.-C.; Sun, K.; Zhan, E.; Zhang, T.; Liu, J.; Li, W.-X., Supported Single Pt1/Au1Atoms for Methanol Steam Reforming. *ACS Catalysis* **2014,** 4, (11), 3886-3890.

107. Kar, S.; Pal, B. N.; Chaudhuri, S.; Chakravorty, D., One-dimensional ZnO nanostructure arrays: Synthesis and characterization. The *Journal of Physical Chemistry B* **2006,** 110, (10), 4605-4611.

108. Kubo, M.; Oumi, Y.; Takaba, H.; Chatterjee, A.; Miyamoto, A.; Kawasaki, M.; Yoshimoto, M.; Koinuma, H., Homoepitaxial growth mechanism of ZnO (0001): Molecular-dynamics simulations. *Physical Review B* **2000,** 61, (23), 16187.

109. Subannajui, K.; Ramgir, N.; Grimm, R.; Michiels, R.; Yang, Y.; Müller, S.; Zacharias, M., ZnO nanowire growth: a deeper understanding based on simulations and controlled oxygen experiments. *Crystal Growth & Design* **2010,** 10, (4), 1585-1589.

110. Borchers, C.; Müller, S.; Stichtenoth, D.; Schwen, D.; Ronning, C., Catalyst-nanostructure interaction in the growth of 1-D ZnO nanostructures. The *Journal of Physical Chemistry B* **2006,** 110, (4), 1656-1660.

111. Im, S.; Jin, B.; Yi, S., Ultraviolet emission and microstructural evolution in pulsed-laser-deposited ZnO films. *Journal of Applied Physics* **2000,** 87, (9), 4558-4561.

112. Wager, J. F., Transparent electronics. *Science* **2003,** 300, (5623), 1245-1246.

113. Grunwaldt, J. D.; Molenbroek, A. M.; topsøe, N. Y.; topsøe, H.; Clausen, B. S., In Situ Investigations of Structural Changes in Cu/ZnO Catalysts. *Journal of Catalysis* **2000,** 194, (2), 452-460.

114. Rensmo, H.; Keis, K.; Lindström, H.; Södergren, S.; Solbrand, A.; Hagfeldt, A.; Lindquist, S. E.; Wang, L. N.; Muhammed, M., High light-to-energy conversion efficiencies for solar cells based on nanostructured ZnO electrodes. *Journal of Physical Chemistry B* **1997,** 101, (14), 2598-2601.

115. Wan, Q.; Li, Q. H.; Chen, Y. J.; Wang, T. H.; He, X. L.; Li, J. P.; Lin, C. L., Fabrication and ethanol sensing characteristics of ZnO nanowire gas sensors. *Applied Physics Letters* **2004,** 84, (18), 3654-3656.

116. Briseno, A. L.; Holcombe, T. W.; Boukai, A. I.; Garnett, E. C.; Shelton, S. W.; Fréchet, J. J. M.; Yang, P., Oligo-and polythiophene/ZnO hybrid nanowire solar cells. *Nano letters* **2009,** 10, (1), 334-340.

117. Guillén, E.; Azaceta, E.; Vega-Poot, A.; Idígoras, J.; Echeberría, J.; Anta, J. A.; Tena-Zaera, R., ZnO/ZnO Core-Shell Nanowire Array Electrodes: Blocking of Recombination and Impressive Enhancement of Photovoltage in Dye-Sensitized Solar Cells. The *Journal of Physical Chemistry C* **2013,** 117, (26), 13365-13373.

118. Law, M.; Greene, L. E.; Radenovic, A.; Kuykendall, T.; Liphardt, J.; Yang, P., ZnO-Al2O3 and ZnO-TiO2 core-shell nanowire dye-sensitized solar cells. The *Journal of Physical Chemistry B* **2006,** 110, (45), 22652-22663.

119. Zhao, R.; Zhu, L.; Cai, F.; Yang, Z.; Gu, X.; Huang, J.; Cao, L., ZnO/TiO2 core–shell nanowire arrays for enhanced dye-sensitized solar cell efficiency. *Applied Physics A* **2013**, 1-7.

120. Sharma, S.; Chawla, S., Enhanced UV emission in ZnO/ZnS core shell nanoparticles prepared by epitaxial growth in solution. *Electronic Materials Letters* **2013,** 9, (3), 267-271.

121. Richters, J. P.; Voss, T.; Kim, D. S.; Scholz, R.; Zacharias, M., Enhanced surface-excitonic emission in ZnO/Al(2)O(3) core-shell nanowires. *Nanotechnology* **2008,** 19, (30), 305202.

122. Liu, M.; Chen, R.; Adamo, G.; MacDonald, K. F.; Sie, E. J.; Sum, T. C.; Zheludev, N. I.; Sun, H.; Fan, H. J., Tuning the influence of metal nanoparticles on ZnO photoluminescence by atomic-layer-deposited dielectric spacer. *Nanophotonics* **2013,** 2, (2), 153-160.

123. Chang, C. M.; Hon, M. H.; Leu, I. C., Improvement in CO sensing characteristics by decorating ZnO nanorod arrays with Pd nanoparticles and the related mechanisms. *Rsc Advances* **2012,** 2, (6), 2469-2475.

124. Sun, S.; Kong, C.; You, H.; Song, X.; Ding, B.; Yang, Z., Facet-selective growth of Cu–Cu 2 O heterogeneous architectures. *CrystEngComm* **2012,** 14, (1), 40-43.

125. Liu, X.-W., Selective growth of Au nanoparticles on (111) facets of Cu2O microcrystals with an enhanced electrocatalytic property. *Langmuir* **2011,** 27, (15), 9100-9104.

126. Li, R.; Zhang, F.; Wang, D.; Yang, J.; Li, M.; Zhu, J.; Zhou, X.; Han, H.; Li, C., Spatial separation of photogenerated electrons and holes among {010} and {110} crystal facets of BiVO4. *Nature communications* **2013,** 4, 1432.

127. Mankin, M. N.; Day, R. W.; Gao, R.; No, Y.-S.; Kim, S.-K.; McClelland, A. A.; Bell, D. C.; Park, H.-G.; Lieber, C. M., Facet-Selective Epitaxy of Compound Semiconductors on Faceted Silicon Nanowires. *Nano letters* **2015,** 15, (7), 4776-4782.

128. KSR, K. K. R., Zinc oxide based photocatalysis: tailoring surface-bulk structure and related interfacial charge carrier dynamics for better environmental applications. *RSC Adv.* **2015,** 5, 3306-3351.

129. Pacholski, C.; Kornowski, A.; Weller, H., Site-Specific Photodeposition of Silver on ZnO Nanorods. *Angewandte Chemie* **2004,** 116, (36), 4878-4881.

130. Balachandran, S.; Swaminathan, M., Facile Fabrication of Heterostructured Bi_2O_3–ZnO Photocatalyst and Its Enhanced Photocatalytic Activity. The *Journal of Physical Chemistry C* **2012,** 116, (50), 26306-26312.

131. Gong, W.; Chen, W.; He, J.; tong, Y.; Liu, C.; Su, L.; Gao, B.; Yang, H.; Zhang, Y.; Zhang, X., Substrate-independent and large-area synthesis of carbon nanotube thin films using ZnO nanorods as template and dopamine as carbon precursor. *Carbon* **2015,** 83, 275-281.

132. Proffit, D. L.; Bai, G. R.; Fong, D. D.; Fister, T. T.; Hruszkewycz, S. O.; Highland, M. J.; Baldo, P. M.; Fuoss, P. H.; Mason, T. O.; Eastman, J. A., Phase stabilization of delta-Bi_2O_3 nanostructures by epitaxial growth onto single crystal SrTiO3 or DyScO3 substrates. *Applied Physics Letters* **2010,** 96, (2).

133. Daneshvar, N.; Salari, D.; Khataee, A., Photocatalytic degradation of azo dye acid red 14 in water on ZnO as an alternative catalyst to TiO 2. *Journal of photochemistry and photobiology A: chemistry* **2004,** 162, (2), 317-322.

134. Harwig, H. A.; Gerards, A. G., the polymorphism of bismuth sesquioxide. The*rmochimica Acta* **1979,** 28, (1), 121-131.

135. Luo, J.; Chiang, Y. M., Existence and stability of nanometer-thick disordered films on oxide surfaces. *Acta materialia* **2000,** 48, (18), 4501-4515.

136. de Sousa, V. C.; Morelli, M. R.; Kiminami, R. H. G., Combustion process in the synthesis of ZnO–Bi_2O_3. *Ceramics International* **2000,** 26, (5), 561-564.

137. Yu, D.; Trad, T.; McLeskey Jr, J. T.; Craciun, V.; Taylor, C. R., ZnO nanowires synthesized by vapor phase transport deposition on transparent oxide substrates. *Nanoscale research letters* **2010,** 5, (8), 1333-1339.

138. de la Rubia, M. A.; Fernandez, J. F.; Caballero, A. C., Equilibrium phases in the Bi_2O_3-rich region of the ZnO–Bi_2O_3 system. In *Journal of the European Ceramic Society*, 2005; Vol. 25, pp 2215-2217.

139. Li, D.; Haneda, H., Morphologies of zinc oxide particles and their effects on photocatalysis. *Chemosphere* **2003,** 51, (2), 129-137.

140. Rashad, A.-G.; Shahidan, R.; Razak, A.; Nouar, T.; Yarub, A.-D., XPS and optical studies of different morphologies of ZnO nanostructures prepared by microwave methods. **2013**.

141. Yi, S.; Yue, X.; Xu, D.; Liu, Z.; Zhao, F.; Wang, D.; Lin, Y., Study on photogenerated charge transfer properties and enhanced visible-light photocatalytic activity of p-type Bi 2 O 3/n-type ZnO heterojunctions. *New Journal of Chemistry* **2015,** 39, (4), 2917-2924.

142. Oropeza, F. E.; Villar-Garcia, I. J.; Palgrave, R. G.; Payne, D. J., A solution chemistry approach to epitaxial growth and stabilisation of Bi 2 Ti 2 O 7 films. *Journal of Materials Chemistry A* **2014,** 2, (43), 18241-18245.

143. Liu, J., Advanced electron microscopy characterization of nanostructured heterogeneous catalysts. *Microscopy and Microanalysis* **2004,** 10, (01), 55-76.

144. Warner, J. H.; Liu, Z.; He, K.; Robertson, A. W.; Suenaga, K., Sensitivity of Graphene Edge States to Surface Adatom Interactions. *Nano letters* **2013,** 13, (10), 4820-4826.

145. Luo, J.; Chiang, Y.-M.; Cannon, R. M., Nanometer-thick surficial films in oxides as a case of prewetting. *Langmuir* **2005,** 21, (16), 7358-7365.

146. Gurlo, A., Nanosensors: towards morphological control of gas sensing activity. SnO2, In2O3, ZnO and WO3 case studies. *Nanoscale* **2011,** 3, (1), 154-165.

147. Scarano, D.; Spoto, G.; Bordiga, S.; Zecchina, A.; Lamberti, C., Lateral interactions in CO adlayers on prismatic ZnO faces: a FTIR and HRTEM study. *Surface Science* **1992,** 276, (1), 281-298.

148. Wander, A.; Harrison, N. M., An ab-initio study of ZnO(11-20). *Surface Science* **2000,** 468, (1-3), L851-L855.

149. Meyer, B.; Marx, D., Density-functional study of the structure and stability of ZnO surfaces. *Physical Review B* **2003,** 67, (3), 035403.

150. Marana, N. L.; Longo, V. M.; Longo, E.; Martins, J. B. L.; Sambrano, J. R., Electronic and structural properties of the (1010) and (1120) ZnO surfaces. The *Journal of Physical Chemistry A* **2008,** 112, (38), 8958-8963.

151. Kazi, Z., AlGaAs/GaAs Laser Diodes with GaAs Islands Active Region on a Si Substrate with Higher Characteristic Temperature. *Japanese journal of applied physics.Part 1, Regular papers & short notes* **1999,** 38, (part 1, no. 1a), 74; 74-76; 76.

152. Frank, F.; van der Merwe, J. H., One-dimensional dislocations. I. Static theory. *Proceedings of the Royal Society of London. Series A, Mathematical and Physical Sciences* **1949**, 205-216.

153. Frank, F.; Van der Merwe, J. In *One-dimensional dislocations. II. Misfitting monolayers and oriented overgrowth*, Proceedings of the Royal Society of London A:

Mathematical, Physical and Engineering Sciences, 1949; the Royal Society: 1949; pp 216-225.

154. Ait Ahcene, T.; Monty, C.; Kouam, J.; Thorel, A.; Petot-Ervas, G.; Djemel, A., Preparation by solar physical vapor deposition (SPVD) and nanostructural study of pure and Bi doped ZnO nanopowders. In *Journal of the European Ceramic Society*, 2007; Vol. 27, pp 3413-3424.

155. Qin, Q.; Zhou, L.; Wang, Y.; Sang, R.; Xu, L., Linear triatomic [ZnBi2]4- in K4ZnBi2. *Dalton Trans* **2014,** 43, (16), 5990-3.

156. Gajović, A.; Silva, A. M. T.; Segundo, R. A.; Šturm, S.; Jančar, B.; Čeh, M., Tailoring the phase composition and morphology of Bi-doped goethite–hematite nanostructures and their catalytic activity in the degradation of an actual pesticide using a photo-Fenton-like process. *Applied Catalysis B: Environmental* **2011,** 103, (3-4), 351-361.

157. Lam, S. M.; Sin, J. C.; Abdullah, A. Z.; Mohamed, A. R., Efficient Photodegradation of Endocrine-Disrupting Chemicals with Bi_2O_3-ZnO Nanorods Under a Compact Fluorescent Lamp. *Water Air and Soil Pollution* **2013,** 224, (5).

158. Štengl, V.; Henych, J.; Slušná, M.; tolasz, J.; Zetková, K., ZnO/Bi 2 O 3 nanowire composites as a new family of photocatalysts. *Powder Technology* **2015,** 270, 83-91.

159. Ait Ahcene, T.; Monty, C.; Kouam, J.; Thorel, A.; Petot-Ervas, G.; Djemel, A., Preparation by solar physical vapor deposition (SPVD) and nanostructural study of pure and Bi doped ZnO nanopowders. *Journal of the European Ceramic Society* **2007,** 27, (12), 3413-3424.

160. Xu, C.; Rho, K.; Chun, J.; Kim, D. E., Fabrication and photoluminescence of ZnO hierarchical nanostructures containing Bi_2O_3. *Nanotechnology* **2006,** 17, (1), 60.

161. Na, H. G.; Yang, J. C.; Kwak, D. S.; Kim, H. W., Bismuth-catalyzed synthesis of ZnO nanowires and their photoluminescence properties. *Ceramics International* **2012,** 38, (5), 3659-3666.

162. Qiu, Y.; Yang, M.; Fan, H.; Zuo, Y.; Shao, Y.; Xu, Y.; Yang, X.; Yang, S., Nanowires of α-and β-Bi 2 O 3: phase-selective synthesis and application in photocatalysis. *CrystEngComm* **2011,** 13, (6), 1843-1850.

163. Blakely, J.; Jackson, K., Growth of crystal whiskers. The *Journal of Chemical Physics* **1962,** 37, (2), 428-430.

164. Yin, Y.; Zhang, G.; Xia, Y., Synthesis and characterization of MgO nanowires through a vapor-phase precursor method. *Advanced Functional Materials* **2002,** 12, (4), 293-298.

165. Xu, J.; Liu, J., Preferential Growth of δ-Bi_2O_3 Layers on the {11-20} Facets of ZnO Nanowires. *Microscopy and Microanalysis* **2013,** 19, (S2), 1516-1517.

166. Ling, B.; Sun, X. W.; Shen, Y. Q.; Dong, Z. L., Hierarchical ZnO/Bi_2O_3 nanostructures: synthesis, characterization, and electron-beam modification. *Applied Physics A* **2010,** 98, (1), 91-96.

167. Senda, T.; Bradt, R. C., Grain Growth in Sintered ZnO and ZnO-Bi_2O_3 Ceramics. *Journal of the American Ceramic Society* **1990,** 73, (1), 106-114.

168. Xu, C.; Rho, K.; Chun, J.; Kim, D.-E., Low-temperature (~250 °C) route to lateral growth of ZnO nanowires. *Applied Physics Letters* **2005,** 87, (25), 253104.

169. Parker, R.; Anderson, R.; Hardy, S., Growth and evaporation kinetics and surface diffusion of K and Hg crystal whiskers. *Applied Physics Letters* **1963,** 3, (6), 93-95.

170. Saunders, R. B.; Garry, S.; Byrne, D.; Henry, M. O.; McGlynn, E., Length versus Radius Relationship for ZnO Nanowires Grown via Vapor Phase Transport. *Crystal Growth & Design* **2012,** 12, (12), 5972-5979.

171. Holladay, J. D.; Wang, Y.; Jones, E., Review of developments in portable hydrogen production using microreactor technology. *Chemical Reviews* **2004,** 104, (10), 4767-4790.

172. Friedrich, M.; Teschner, D.; Knop-Gericke, A.; Armbrüster, M., Influence of bulk composition of the intermetallic compound ZnPd on surface composition and methanol steam reforming properties. *Journal of Catalysis* **2012,** 285, (1), 41-47.

173. Friedrich, M.; Penner, S.; Heggen, M.; Armbruster, M., High CO2 selectivity in methanol steam reforming through ZnPd/ZnO teamwork. *Angew Chem Int Ed Engl* **2013,** 52, (16), 4389-92.

174. Dagle, R. A.; Chin, Y.-H.; Wang, Y., the Effects of PdZn Crystallite Size on Methanol Steam Reforming. To*pics in Catalysis* **2007,** 46, (3-4), 358-362.

175. Iwasa, N.; Mayanagi, T.; Nomura, W.; Arai, M.; Takezawa, N., Effect of Zn addition to supported Pd catalysts in the steam reforming of methanol. *Applied Catalysis A: General* **2003,** 248, (1-2), 153-160.

176. Takezawa, N.; Iwasa, N., Steam reforming and dehydrogenation of methanol: Difference in the catalytic functions of copper and group VIII metals. *Catalysis today* **1997,** 36, (1), 45-56.

177. Liang, S.; Hao, C.; Shi, Y., the Power of Single-Atom Catalysis. *ChemCatChem* **2015,** 7, (17), 2559-2567.

178. Lei, Y.; Mehmood, F.; Lee, S.; Greeley, J.; Lee, B.; Seifert, S.; Winans, R. E.; Elam, J. W.; Meyer, R. J.; Redfern, P. C., Increased silver activity for direct propylene epoxidation via subnanometer size effects. *Science* **2010,** 328, (5975), 224-228.

179. Turner, M.; Golovko, V. B.; Vaughan, O. P.; Abdulkin, P.; Berenguer-Murcia, A.; Tikhov, M. S.; Johnson, B. F.; Lambert, R. M., Selective oxidation with dioxygen

by gold nanoparticle catalysts derived from 55-atom clusters. *Nature* **2008,** 454, (7207), 981-983.

180. Herzing, A. A.; Kiely, C. J.; Carley, A. F.; Landon, P.; Hutchings, G. J., Identification of active gold nanoclusters on iron oxide supports for CO oxidation. *Science* **2008,** 321, (5894), 1331-1335.

181. Qiao, B.; Wang, A.; Yang, X.; Allard, L. F.; Jiang, Z.; Cui, Y.; Liu, J.; Li, J.; Zhang, T., Single-atom catalysis of CO oxidation using Pt1/FeOx. *Nat Chem* **2011,** 3, (8), 634-41.

182. Yang, X. F.; Wang, A.; Qiao, B.; Li, J.; Liu, J.; Zhang, T., Single-atom catalysts: a new frontier in heterogeneous catalysis. *Acc Chem Res* **2013,** 46, (8), 1740-8.

183. Wang, Y.; Zhang, J.; Hengyong, X. U., Interaction between Pd and ZnO during Reduction of Pd/ZnO Catalyst for Steam Reforming of Methanol to Hydrogen. *Chinese Journal of Catalysis* **2006,** 27, (3), 217-222.

184. Holzapfel, H. H.; Wolfbeisser, A.; Rameshan, C.; Weilach, C.; Rupprechter, G., PdZn Surface Alloys as Models of Methanol Steam Reforming Catalysts: Molecular Studies by LEED, XPS, TPD and PM-IRAS. To*pics in Catalysis* **2014,** 57, (14-16), 1218-1228.

185. Chen, Z.-X.; Neyman, K. M.; Lim, K. H.; Rösch, N., CH3O decomposition on PdZn (111), Pd (111), and Cu (111). A theoretical study. *Langmuir* **2004,** 20, (19), 8068-8077.

186. SCI-IWAB, G.-M., Electronics of supported catalysts. *Advances in Catalysis* **1979,** 27, 1.

187. Liu, J. J., Advanced electron microscopy of metal–support interactions in supported metal catalysts. *ChemCatChem* **2011,** 3, (6), 934-948.

188. Yang, X.-F.; Wang, A.; Qiao, B.; Li, J.; Liu, J.; Zhang, T., Single-atom catalysts: a new frontier in heterogeneous catalysis. *Accounts of chemical research* **2013,** 46, (8), 1740-1748.

189. Lin, J.; Wang, A.; Qiao, B.; Liu, X.; Yang, X.; Wang, X.; Liang, J.; Li, J.; Liu, J.; Zhang, T., Remarkable performance of Ir1/FeO(x) single-atom catalyst in water gas shift reaction. *J Am Chem Soc* **2013,** 135, (41), 15314-7.

190. Yang, M.; Liu, J.; Lee, S.; Zugic, B.; Huang, J.; Allard, L. F.; Flytzani-Stephanopoulos, M., A common single-site Pt(II)-O(OH)x- species stabilized by sodium on "active" and "inert" supports catalyzes the water-gas shift reaction. *J Am Chem Soc* **2015,** 137, (10), 3470-3.

191. Liang, J.-X.; Lin, J.; Yang, X.-F.; Wang, A.-Q.; Qiao, B.-T.; Liu, J.; Zhang, T.; Li, J., theoretical and Experimental Investigations on Single-Atom Catalysis: Ir1/FeOxfor CO Oxidation. The *Journal of Physical Chemistry C* **2014,** 118, (38), 21945-21951.

192. Qiao, B.; Wang, A.; Yang, X.; Allard, L. F.; Jiang, Z.; Cui, Y., Single-atom catalysis of CO oxidation using Pt1/FeOx. *Single-atom catalysis of CO oxidation using Pt1/FeOx* **2011**.

193. Lebarbier, V.; Dagle, R.; Datye, A.; Wang, Y., the effect of PdZn particle size on reverse-water–gas-shift reaction. *Applied Catalysis A: General* **2010,** 379, (1-2), 3-6.

194. Zhang, S.; Chang, C. R.; Huang, Z. Q.; Li, J.; Wu, Z.; Ma, Y.; Zhang, Z.; Wang, Y.; Qu, Y., High Catalytic Activity and Chemoselectivity of Sub-nanometric Pd Clusters on Porous Nanorods of CeO_2 for Hydrogenation of Nitroarenes. *J Am Chem Soc* **2016,** 138, (8), 2629-37.

195. Peterson, E. J.; DeLaRiva, A. T.; Lin, S.; Johnson, R. S.; Guo, H.; Miller, J. T.; Hun Kwak, J.; Peden, C. H.; Kiefer, B.; Allard, L. F.; Ribeiro, F. H.; Datye, A. K., Low-temperature carbon monoxide oxidation catalysed by regenerable atomically dispersed palladium on alumina. *Nat Commun* **2014,** 5, 4885.

196. Zhou, H.; Yang, X.; Wang, A.; Miao, S.; Liu, X.; Pan, X.; Su, Y.; Li, L.; Tan, Y.; Zhang, T., Pd/ZnO catalysts with different origins for high chemoselectivity in acetylene semi-hydrogenation. *Chinese Journal of Catalysis* **2016,** 37, (5), 692-699.

197. Vilé, G.; Albani, D.; Nachtegaal, M.; Chen, Z.; Dontsova, D.; Antonietti, M.; López, N.; Pérez-Ramírez, J., A Stable Single-Site Palladium Catalyst for Hydrogenations. *Angewandte Chemie International Edition* **2015,** 54, (38), 11265-11269.

198. Lucci, F. R.; Darby, M. T.; Mattera, M. F.; Ivimey, C. J.; therrien, A. J.; Michaelides, A.; Stamatakis, M.; Sykes, E. C., Controlling Hydrogen Activation, Spillover, and Desorption with Pd-Au Single-Atom Alloys. *J Phys Chem Lett* **2016,** 7, (3), 480-5.

199. Chen, Z.-X.; Neyman, K. M.; Gordienko, A. B.; Rösch, N., Surface structure and stability of PdZn and PtZn alloys: Density-functional slab model studies. *Physical Review B* **2003,** 68, (7), 075417.

200. Hokenek, S.; Kuhn, J. N., Methanol decomposition over palladium particles supported on silica: Role of particle size and co-feeding carbon dioxide on the catalytic properties. *ACS Catalysis* **2012,** 2, (6), 1013-1019.

201. Schauermann, S.; Hoffmann, J.; Johánek, V.; Hartmann, J.; Libuda, J., Adsorption, decomposition and oxidation of methanol on alumina supported palladium particles. *Physical Chemistry Chemical Physics* **2002,** 4, (15), 3909-3918.

202. Shen, W.-J.; Matsumura, Y., Interaction between palladium and the support in Pd/CeO 2 prepared by deposition–precipitation method and the catalytic activity for methanol decomposition. *Journal of Molecular Catalysis A: Chemical* **2000,** 153, (1), 165-168.

203. Ryndin, Y. A.; Hicks, R.; Bell, A.; Yermakov, Y. I., Effects of metal-support interactions on the synthesis of methanol over palladium. *Journal of Catalysis* **1981,** 70, (2), 287-297.

204. Iwasa, N.; Suzuki, H.; Terashita, M.; Arai, M.; Takezawa, N., Methanol synthesis from CO2 under atmospheric pressure over supported Pd catalysts. *Catalysis letters* **2004,** 96, (1-2), 75-78.

205. Bahruji, H.; Bowker, M.; Hutchings, G.; Dimitratos, N.; Wells, P.; Gibson, E.; Jones, W.; Brookes, C.; Morgan, D.; Lalev, G., Pd/ZnO catalysts for direct CO2 hydrogenation to methanol. *Journal of Catalysis* **2016**.

206. Iwasa, N.; Arai, S.; Arai, M., Selective oxidation of CO with modified Pd/ZnO catalysts in the presence of H 2: Effects of additives and preparation variables. *Selective oxidation of CO with modified Pd/ZnO catalysts in the presence of H 2: Effects of additives and preparation variables* **2008**.

207. Johnson, R. S.; DeLaRiva, A.; Ashbacher, V.; Halevi, B.; Villanueva, C. J.; Smith, G. K.; Lin, S.; Datye, A. K.; Guo, H., the CO oxidation mechanism and reactivity on PdZn alloys. *Physical Chemistry Chemical Physics* **2013,** 15, (20), 7768-7776.

208. J.liu, Advanced Electron Microscopy of Metal Support Interactions in Supported Metal Catalysts.

209. Sá, S.; Silva, H.; Brandão, L.; Sousa, J. M., Catalysts for methanol steam reforming—A review. *Catalysts for methanol steam reforming—A review* **2010**.

210. Gu, X.-K.; Li, W.-X., First-principles study on the origin of the different selectivities for methanol steam reforming on Cu (111) and Pd (111). The *Journal of Physical Chemistry C* **2010,** 114, (49), 21539-21547.

211. Xu, J.; Wu, H.; Liu, J. J., ZnO Nanowire Supported Metal Single Atoms for CO oxidation. *Microscopy and Microanalysis* **2016,** 22, (S3), 872-873.

212. Łomot, D.; Karpiński, Z., Hydrogen oxidation over alumina-supported palladium–nickel catalysts. *Research on Chemical Intermediates* **2015,** 41, (12), 9171-9179.

213. Qiao, B.; Liang, J.-X.; Wang, A.; Xu, C.-Q.; Li, J.; Zhang, T.; Liu, J. J., Ultrastable single-atom gold catalysts with strong covalent metal-support interaction (CMSI). *Nano Research* **2015,** 8, (9), 2913-2924.

214. Boronin, A.; Slavinskaya, E.; Danilova, I.; Gulyaev, R.; Amosov, Y. I.; Kuznetsov, P.; Polukhina, I.; Koscheev, S.; Zaikovskii, V.; Noskov, A., Investigation of palladium interaction with cerium oxide and its state in catalysts for low-temperature CO oxidation. *Catalysis today* **2009,** 144, (3), 201-211.

215. Kummer, J., Use of noble metals in automobile exhaust catalysts. The *Journal of Physical Chemistry* **1986,** 90, (20), 4747-4752.

216. Armor, J. N., the multiple roles for catalysis in the production of H 2. *Applied Catalysis A: General* **1999,** 176, (2), 159-176.

217. Liu, K.; Wang, A.; Zhang, T., Recent advances in preferential oxidation of CO reaction over platinum group metal catalysts. *ACS Catalysis* **2012,** 2, (6), 1165-1178.

218. Glaspell, G.; Fuoco, L.; El, S., Microwave synthesis of supported Au and Pd nanoparticle catalysts for CO oxidation. *Microwave synthesis of supported Au and Pd nanoparticle catalysts for CO oxidation* **2005**.

219. Comotti, M.; Li, W. C.; Spliethoff, B., Support effect in high activity gold catalysts for CO oxidation. *Support effect in high activity gold catalysts for CO oxidation* **2006**.

220. Li, S.; Liu, G.; Lian, H.; Jia, M.; Zhao, G.; Jiang, D., Low-temperature CO oxidation over supported Pt catalysts prepared by colloid-deposition method. *Low-temperature CO oxidation over supported Pt catalysts prepared by colloid-deposition method* **2008**.

221. Liu, X.; Liu, M. H.; Luo, Y. C.; Mou, C. Y.; Lin, S. D., Strong metal–support interactions between gold nanoparticles and ZnO nanorods in CO oxidation. *Strong metal–support interactions between gold nanoparticles and ZnO nanorods in CO oxidation* **2012**.

222. Lin, S.; Ye, X.; Johnson, R. S.; Guo, H., First-Principles Investigations of Metal (Cu, Ag, Au, Pt, Rh, Pd, Fe, Co, and Ir) Doped Hexagonal Boron Nitride Nanosheets: Stability and Catalysis of CO Oxidation. The *Journal of Physical Chemistry C* **2013,** 117, (33), 17319-17326.

223. Li, F.; Li, Y.; Zeng, X. C.; Chen, Z., Exploration of High-Performance Single-Atom Catalysts on Support M1/FeOxfor CO Oxidation via Computational Study. *ACS Catalysis* **2015,** 5, (2), 544-552.

224. Remediakis, I. N.; Lopez, N.; Nørskov, J. K., CO oxidation on rutile-supported Au nanoparticles. *Angewandte Chemie* **2005,** 117, (12), 1858-1860.

225. Bruix, A.; Lykhach, Y.; Matolinova, I.; Neitzel, A.; Skala, T.; Tsud, N.; Vorokhta, M.; Stetsovych, V.; Sevcikova, K.; Myslivecek, J.; Fiala, R.; Vaclavu, M.; Prince, K. C.; Bruyere, S.; Potin, V.; Illas, F.; Matolin, V.; Libuda, J.; Neyman, K. M., Maximum noble-metal efficiency in catalytic materials: atomically dispersed surface platinum. *Angew Chem Int Ed Engl* **2014,** 53, (39), 10525-30.

226. Duarte, R. B.; Safonova, O. V.; Krumeich, F.; van Bokhoven, J. A., Atomically dispersed rhodium on a support: the influence of a metal precursor and a support. *Phys Chem Chem Phys* **2014,** 16, (48), 26553-60.

227. Abbet, S.; Heiz, U.; Häkkinen, H.; Landman, U., CO oxidation on a single Pd atom supported on magnesia. *Physical review letters* **2001,** 86, (26), 5950.

228. Ghosh, T. K.; Nair, N. N., Rh1/γ-Al2O3 Single-Atom Catalysis of O2 Activation and CO Oxidation: Mechanism, Effects of Hydration, Oxidation State, and Cluster Size. *ChemCatChem* **2013,** 5, (7), 1811-1821.

229. Moses-DeBusk, M.; Yoon, M.; Allard, L. F.; Mullins, D. R.; Wu, Z.; Yang, X.; Veith, G.; Stocks, G. M.; Narula, C. K., CO oxidation on supported single Pt atoms: Experimental and ab initio density functional studies of CO interaction with Pt atom on θ-Al2O3 (010) surface. *Journal of the American Chemical Society* **2013,** 135, (34), 12634-12645.

230. Yang, T.; Fukuda, R.; Hosokawa, S.; Tanaka, T.; Sakaki, S.; Ehara, M., A theoretical Investigation on CO Oxidation by Single-Atom Catalysts M1/γ-Al2O3 (M= Pd, Fe, Co, and Ni). *ChemCatChem* **2017**.

231. Jen, S.; Anderson, A. B., CO oxidation mechanisms over ZnO: Molecular orbital theory. *Surface science* **1989,** 223, (1-2), 119-130.

232. Lin, J.; Qiao, B.; Liu, J.; Huang, Y.; Wang, A.; Li, L.; Zhang, W.; Allard, L. F.; Wang, X.; Zhang, T., Design of a Highly Active Ir/Fe (OH) x Catalyst: Versatile Application of Pt-Group Metals for the Preferential Oxidation of Carbon Monoxide. *Angewandte Chemie International Edition* **2012,** 51, (12), 2920-2924.

233. Gajdoš, M.; Eichler, A.; Hafner, J., CO adsorption on close-packed transition and noble metal surfaces: trends from ab initio calculations. *Journal of Physics: Condensed Matter* **2004,** 16, (8), 1141.

234. Liu, W.; Zhu, Y.; Lian, J.; Jiang, Q., Adsorption of CO on Surfaces of 4d and 5d Elements in Group VIII. The *Journal of Physical Chemistry C* **2007,** 111, (2), 1005-1009.

235. Strayer, M. E.; Senftle, T. P.; Winterstein, J. P.; Vargas-Barbosa, N. M.; Sharma, R.; Rioux, R. M.; Janik, M. J.; Mallouk, T. E., Charge Transfer Stabilization of Late Transition Metal Oxide Nanoparticles on a Layered Niobate Support. *J Am Chem Soc* **2015,** 137, (51), 16216-24.

236. Parkinson, G. S.; Novotny, Z.; Argentero, G.; Schmid, M.; Pavelec, J.; Kosak, R.; Blaha, P.; Diebold, U., Carbon monoxide-induced adatom sintering in a Pd–Fe3O4 model catalyst. *Nature materials* **2013,** 12, (8), 724-728.

237. Bliem, R.; van der Hoeven, J. E.; Hulva, J.; Pavelec, J.; Gamba, O.; de Jongh, P. E.; Schmid, M.; Blaha, P.; Diebold, U.; Parkinson, G. S., Dual role of CO in the stability of subnano Pt clusters at the Fe3O4 (001) surface. *Proceedings of the National Academy of Sciences* **2016,** 113, (32), 8921-8926.

238. Chang, T.-Y.; Ikuhara, Y.; Shibata, N., Effects of TiO2 Support on the Initial Stage of Pt Nanoparticle Growth. *Applied Physics Express* **2013,** 6, (2), 025503.

239. Wheeler, C.; Jhalani, A.; Klein, E.; Tummala, S.; Schmidt, L., the water–gas-shift reaction at short contact times. Journal of catalysis 2004, 223, (1), 191-199.

240. Fu, Q.; Saltsburg, H.; Flytzani-Stephanopoulos, M., Active nonmetallic Au and Pt species on ceria-based water-gas shift catalysts. Science 2003, 301, (5635), 935-938.

241. Koh, S. J.; Ehrlich, G., Self-assembly of one-dimensional surface structures: long-range interactions in the growth of Ir and Pd on W (110). *Physical review letters* **2001,** 87, (10), 106103.

242. Mocking, T. F.; Bampoulis, P.; Oncel, N.; Poelsema, B.; Zandvliet, H. J., Electronically stabilized nanowire growth. *Nature communications* **2013,** 4.

APPENDIX A

LIST OF PUBLICATIONS DURING THE STUDY

TOWARDS THE DOCTORAL DEGREE

List of publications by Jia Xu, during her Ph.D. studies at Arizona State University:

Jia Xu and Jingyue Liu. "Facet-Selective Epitaxial Growth of δ-Bi_2O_3 on ZnO Nanowires." Chemistry of Materials 28, (2016): 8141-8148.

Yonghai Yue, Datong Yuchi, Pengfei Guan, Jia Xu, Lin Guo, and Jingyue Liu. "Atomic scale observation of oxygen delivery during silver-oxygen nanoparticle catalysed oxidation of carbon nanotubes." Nature Communications 7, (2016).

Jiake Wei, Nan Jiang, Jia Xu, Xuedong Bai, and Jingyue Liu. "Strong coupling between ZnO excitons and localized surface plasmons of silver nanoparticles studied by STEM-EELS." Nano letters 15, (2015): 5926-5931.

Guanhua Zhang, Yian Song, Hang Zhang, Jia Xu, Huigao Duan, and Jingyue Liu. "Radially Aligned Porous Carbon Nanotube Arrays on Carbon Fibers: A Hierarchical 3D Carbon Nanostructure for High - Performance Capacitive Energy Storage." Advanced Functional Materials 26, (2016): 3012-3020.

Proceedings:

Jia Xu and Jingyue Liu. Synthesis and Characterization of Bismuth Functionalized ZnO Nanostructures[J]. Microscopy and Microanalysis, 2012, 18(S2): 1334-1335.

Jia Xu, Diana Convey, Datong Yuchi and Jingyue Liu, et al. High Spatial Resolution CL Imaging of ZnO, Bi/ZnO and Sb/ZnO Nanostructures[J]. Microsc. Microanal, 2013, 19: 2.

Jia Xu and Jingyue Liu. Influence of Bismuth Additive on the Growth of ZnO Nanostructures[J]. Microscopy and Microanalysis, 2013, 19(S2): 1976-1977.

Jia Xu and Jingyue Liu. Atomic resolution study of the bonding between ZnO nanowires[J]. Microscopy and Microanalysis, 2014, 20(S3): 194-195.

Jia Xu and Jingyue Liu. Interfacial atomic structure of BiO x functionalized ZnO nanowires[J]. Microscopy and Microanalysis, 2014, 20(S3): 1964-1965.

Jia Xu and Jingyue Liu. Aberration-corrected STEM of Cross-sectional View of Core-shell Nanowires Prepared by Ultramicrotomy[J]. Microscopy and Microanalysis, 2015, 21(S3): 1739-1740.

Jia Xu, Honglu Wu and Jingyue Liu. ZnO Nanowire Supported Metal Single Atoms for CO oxidation[J]. Microscopy and Microanalysis, 2016, 22(S3): 872-873.

Awards:

the Diatome U.S. second place annual meeting of Microscopy and Microanalysis (2015)

First prize of student poster award at Microscopy and Microanalysis annual meeting(2014)

Second prize of student poster award at Arizona Imaging and Microanalysis Society(2014)